Surface Quality of Aluminium Extrusion Products

Xiao Ma

This research was carried out under project number MC 5.05218 in the framework of the Research Program of the Materials innovation institute (M2i) in the Netherlands (www.M2i.nl).

De promotiecomissie is als volgt opgesteld:

prof.dr.ir. F.Eising	Universiteit Twente	voorzitter en secretaris
prof.dr.ir. D.J. Schipper	Universiteit Twente	promotor
prof.dr.ir. A.J. Huis in't Veld	Universiteit Twente	
prof.dr.ir. F.J.A.M. van Houten	Universiteit Twente	
dr.ir. A.H. van den Boogaard	Universiteit Twente	
prof. A. Matthews	University of Sheffield	

Ma, Xiao
Surface quality of aluminium extrusion products
PhD Thesis, University of Twente, Enschede, the Netherlands,
February 2011

Keywords: aluminium alloy, extrusion, surface quality model, friction model.

Cover design by Xiao Ma
Printed by Ipskamp Drukkers

ISBN: 978-90-77172-72-8

SURFACE QUALITY OF ALUMINIUM EXTRUSION PRODUCTS

PROEFSCHRIFT

Ter verkrijging van
de graad van doctor aan de Universiteit van Twente,
op gezag van de rector magnificus,
prof.dr. H. Brinksma,
volgens besluit van het College voor Promoties
in het openbaar te verdedigen
op vrijdag 11 februari 2011 om 15.00 uur

door

Xiao Ma
geboren 23 Oktober 1985
te Hunan, China

Dit proefschrift is goedgekeurd door:
de promotor: prof.dr.ir. D.J. Schipper
de assistent promotor: dr.ir. M.B. de Rooij

Samenvatting

Aluminium extrusie is een omvormproces dat wordt gebruikt om profielen te produceren en omvat bijna de helft van de totale aluminium productie. Door een verwarmd blok aluminium door een matrijs met een opening in de vorm van het te verkrijgen profiel te persen kan een grote verscheidenheid aan profielen op een efficiënte wijze worden geproduceerd. In dit proefschrift wordt aandacht besteed aan een belangrijk aspect van extrusie: de oppervlaktekwaliteit van de geëxtrudeerde producten. Hoge temperatuur scheurvorming en verschijnselen als gevolg van beginnende smelt worden buiten beschouwing gelaten omdat deze buiten de operationele procescondities vallen. Oppervlaktedefecten die binnen het proceskader optreden, zoals het vormen van *pickups* (ook wel 'pers-vlooien' genoemd) zijn het onderwerp van dit onderzoek.

De doelstellingen van dit onderzoek zijn:

- Het begrijpen van de mechanismen die verantwoordelijk zijn voor het ontstaan van oppervlaktedefecten binnen de operationele procescondities;
- Het ontwikkelen van een fysisch model dat de vorming van oppervlaktedefecten beschrijft;
- Het ontwikkelen van een oppervlaktekwaliteitsindicator die als postprocessor gekoppeld kan worden aan een Eindige Elementen Pakket. Met deze indicator kan het extrusieproces worden geoptimaliseerd met betrekking tot de oppervlaktekwaliteit.

Het eerste punt vormt in feite het fundament van dit onderzoek. Wat zijn relevante oppervlaktedefecten? Hoe worden deze gevormd? In dit proefschrift is vastgesteld dat ernstige oppervlaktedefecten die optreden binnen de operationele procesparameters hun oorsprong hebben als oppervlakte-*pickup*. Om te begrijpen hoe deze worden gevormd is de micro-structuur bepaald en is er een analyse van de samenstelling van *pickups* uitgevoerd. Hieruit bleek dat de vorming van *pickups* gerelateerd is aan materiaaloverdracht tussen de *bearing* (het deel van de matrijs dat de vorm van het profiel vastlegt) en het oppervlak van het extrudaat. Dit is het gevolg van de hoge adhesie tussen beide loopvlakken. Tenslotte worden de mechanismen die verantwoordelijk zijn voor het ontstaan van oppervlakte-*pickups* gedetailleerd beschreven.

Vervolgens is er een fysisch model ontwikkeld dat gebaseerd is op de

mechanismen die verantwoordelijk zijn voor de vorming van *pickups*. Om de verschijnselen die optreden in het contact tussen de *bearing* en het oppervlak van het extrudaat te modelleren zijn eerst de tribologische aspecten van de interface gemodelleerd. Een belastingsafhankelijk model voor het contact- en wrijvingsgedrag is ontwikkeld om het samengroeien van contacten bij hoge drukken te modelleren. Dit model is gebaseerd op ruwheidstoppen, dit in tegenstelling tot de klassieke contactmodellen. Het contact- en wrijvingsmodel is toegepast op de *bearing* van een aluminium extrusie matrijs. Met het model zijn berekeningen aan de afmetingen van de *stick*- en *slip*-regimes op het oppervlak van de *bearing* uitgevoerd. Deze berekeningen laten zien dat de grootte van deze regimes afhangt van het wrijvingsniveau in het contact tussen aluminium en *bearing*. Het contact- en wrijvingsmodel is geverifieerd met behulp van experimenten met deelbare matrijs. Vergelijking van de lengtes van de stick- en slip zones op de bearing van deze matrijs met resultaten van berekeningen laten zien dat het model toegepast kan worden op aluminium extrusie.

Het tweede deel van het fysische model betreft het modelleren van overdracht van materiaal tussen de bearing en het oppervlak van het extrudaat. Er is gemodelleerd hoe deze pickups, na een kritische vorm en grootte bereikt te hebben, uiteindelijk loskomen van de bearing en *pickup* defecten veroorzaken. Hiertoe is het bestaande klodder-groei model uitgebreid en aangepast teneinde het gedrag van aluminiumlegeringen te beschrijven. Dit model is vervolgens gekoppeld aan eindige elementen berekeningen.

Op basis van het ontwikkelde fysische model is een indicator voor de oppervlaktekwaliteit ontwikkeld. Deze indicator beschrijft de mate van oppervlaktebeschadigingen van extrusieproducten op basis van het aantal "losgelaten klodders". Gebaseerd op de berekeningen met dit model zijn diagrammen voor de oppervlaktekwaliteit opgesteld. De indicator voor de oppervlaktekwaliteit is gevalideerd met extrusie experimenten met een deelbare matrijs, waarin het aantal oppervlaktedefecten op het productoppervlak werd geteld. De berekende resultaten komen overeen met de experimenten.

Tenslotte wordt een praktijkstudie gepresenteerd. Deze praktijkstudie is bedoeld om een voorbeeld te geven hoe de indicator de oppervlaktekwaliteit in de extrusie praktijk kan verbeteren. Gedetailleerde procedures voor de implementatie van de oppervlaktekwaliteit indicator en de integratie in het totale ontwerpproces worden voorgesteld. Ook worden enkele aanbevelingen met betrekking tot de industriële praktijk gedaan.

Summary

Aluminium extrusion is a forming process used to produce profiles, and accounts for almost a half of aluminium production. By forcing a heated billet through a die opening that resembles the required profile shape, a large variety of profiles can be made efficiently. In this thesis, an important aspect of extrusion is addressed: surface quality of the extruded products. Surface hot cracking and incipient melting are not part of this research though, as they occur outside the appropriate process window. Surface defects occurring inside the process window, namely, the formation of surface pickups, have been studied.

The objectives of this research are threefold:

- Understand the formation mechanisms of surface defects occurring inside the process window;
- Develop a physical model that describes surface defect formation;
- Coupled with FEM, develop a surface quality predictor by which the process can be tailored with respect to good surface quality.

The first issue in fact forms the fundamentals of this study. What are the relevant surface defects? How are they formed? It has been established in this thesis that severe surface defects occurring inside the process window are of surface pickup origin. To understand how they are formed, a microstructural study and compositional analysis of the pickups have been performed. From these studies it was understood that formation of pickups is closely related to material transfer between the bearing and the extrudate surfaces, as a result of large adhesion between the counter-surfaces. A formation mechanism of surface pickups has been proposed.

A physical model can now be developed. To model a phenomenon occurring at the bearing–extrudate interface, the tribological aspects of this interface have been modelled. A load dependent contact and friction model has been developed to account for contact coalescence at high pressure level situations, as opposed to the classical summit-based contact model. The contact and friction model has been applied to the bearing area of aluminium extrusion. Calculations show that the sticking / slipping lengths on the bearing surface are a function of the friction level inside the bearing channel. The contact and friction model has been verified by

performing split die extrusion experiments, where measurements of the sticking and slipping lengths on the split bearing show that the model is applicable to aluminium extrusion.

The second part of the physical model concerns modelling the transfer of material between the bearing–extrudate surfaces and how they eventually detach to form pickup defects. The existing lump growth model is extended and modified to describe the behaviour of aluminium alloys. Further, this physical model is coupled to FEM calculations.

Based on the developed physical model, a surface quality predictor has been developed that indicates the degree of surface damage of extrusion products as the number of “detached lumps”. Based on this surface quality diagrams have been constructed. The surface quality predictor has been validated by split die extrusion experiments, in which surface defects on product surfaces were counted. The calculation results show good agreement with experiments.

A case study is presented in this thesis to give an example of how such a surface quality predictor improves an extrusion process. Detailed procedures for implementing the surface quality predictor and integrating it into the complete designing process have been proposed. Some recommendations regarding industrial practice are given.

Acknowledgements

It is time to end this chapter of my life by finishing the PhD thesis. Four years ago I started the journey with aspirations and expectations, wondering what it would be like four years after. Now I can see it. It is a moment filled with joy of my achievements, and more importantly, full with gratitude.

First of all, M2i needs to be thanked for providing us researchers such a platform for seamless integration between industry and academia. The fast and transparent knowledge transfer, or "valorisation", has trained us to be researchers with an entrepreneurial mind; the amount of continuous education provided by M2i, over the course of four years, has also been very beneficial for the development of our characters; particularly, the efforts towards better care for us employees, create excellent conditions and momentum for us to reach maximum performance.

Thanks to such a platform I am lucky enough to have worked with a lot of people in the M2i network. I would like to thank Andrew den Bakker from Nedal, Kjell Nilsen from Boal, Robert Werkhoven from TNO and Alexis Miroux from TUDelft for our great collaboration. I must also thank Professor Laurens Katgerman and Bert Heijselaers, to name a few, to have inspired me with their expertise and knowledge whenever things went to a deadlock.

The majority of my time has been spent within the campus of the University of Twente, to be specific, the group of Surface Technology and Tribology. Professor Dik Schipper leads the group, and he has been a tremendous mentor for me. His encouragement, guidance and support always seemed to be spot-on for me, in every aspect of my four year's time. I would like to thank Matthijn de Rooij for being my daily supervisor, who really assisted me on a "daily" basis. Therefore, I thank you, Dik and Matthijn, for guiding me in the way that led me where I am today. I must also express my gratitude to Belinda, our secretary, for arranging everything and making sure that I felt home in a foreign country. Eric, Walter, Willie, Laura and Dedy, I thank you for your technical assistance and endless wisdom.

And of course, my lovely colleagues in the group, with whom the journey is completed: Adeel, Agnieszka, Dinesh, Ellen, Gerrit, Ioan, Jiupeng, Mahdiar, Marc,

Martijn, Natalia, Noor, Radu and Rob. Each of you guys possesses a certain character and together we form a very pleasant, easy and inspiring international environment. We have had a lot of great moments and memories together, and they will always be remembered. So guys, it is a privilege to have worked with you all.

To my girlfriend, Shangxia Song, who has always been there to give me enough understanding, encouragement and support, to take the pressure off my shoulder when it piled up, I thank you for your love and trust.

Finally, my family in China. My mom and dad, my other relatives and friends. They deserve huge appreciation for shaping me who I am today. They are the solid backup for me, asserting me that there is always a warm shelter on the other part of the world. The last paragraph (in Chinese) is dedicated to them:

我亲爱的家人和朋友们:

感谢你们一直以来的理解，支持和帮助。你们是我独处异乡的坚强后盾，也是我一直前进的动力。这本书是我四年研究的成果， 我希望把它献给你们， 来表达我一直不曾表达，但是一直满怀心中的无尽感激。 新的生活篇章即将开始， 我相信我能一直得到你们的祝福。 我会继续加油的！

马骁

Xiao Ma
Enschede, the Netherlands
2011

List of publications

Journal papers

Ma, X. and Matthews, A., Evaluation of abradable seal coating mechanical properties, Wear 267, 1501 – 1510.

Ma, X., Rooij, M.B. de and Schipper, D. J., 2009, A load dependent contact and friction model for fully plastic conditions, Wear 269, 790 – 796.

Ma, X., Rooij, M.B. de and Schipper, D. J., 2008, Modelling of contact and friction in aluminium extrusion, Tribology International 43, 1138 – 1144.

Ma, X., Rooij, M.B. de and Schipper, D.J., 2011, Friction conditions in the bearing area of aluminium extrusion, in preparation.

Ma, X., Rooij, M.B. de and Schipper, D.J., 2011, On the formation of surface defects on aluminium extrusion products, in preparation.

Ma, X., Rooij, M.B. de and Schipper, D.J., 2011, Modelling the formation of surface defects on aluminium extrusion products, in preparation.

Conference proceedings

Ma, X., Rooij, M.B. de and Schipper, D.J., 2008, Modelling of contact and friction in aluminium extrusion, Proceedings of International Conference on Advanced Tribology, Singapore. .

Ma, X., Rooij, M.B. de and Schipper, D.J., 2009, On the formation of a sticking layer on the bearing during thin – section aluminium extrusion, Proceedings of Comsol conference, Milan.

Rooij, M.B. de, Ma, X., Bakker, A.J. den and Werkhoven, R.J., 2011, Surface quality prediction in aluminium extrusion, abstract submitted to ICEB 2011.

Bakker, A.J. den , Ma, X., Rooij, M.B.de, and Werkhoven, R.J., 2012, Surface Pick-up Formation: New Limits In The Limit Diagram, abstract submitted to ET 2012.

Nomenclature

Roman symbols

A	Contact area	[m^2]
A_{cr}	Autocorrelation function	[m^2]
A_r	Real contact area	[m^2]
A_z	Constant in the constitutive equation	[s^{-1}]
a	Contact radius	[m]
a_{mj}	Major contact radius of an elliptical contact	[m]
a_{mn}	Minor contact radius of an elliptical contact	[m]
c	Constant (fully defined by suffixes)	[–]
C	Specific heat capacity	[J/(kgK)]
D	Diameter of components	[m]
D_c	Degree of contact radius	[−]
D_i	Degree of indentation	[−]
D_{ini}	Degree of initiation	[−]
D_p	Degree of penetration	[–]
d	Distance of any kind	[m]
h	Mean surface separation	[m]
h_{pr}	Height number of an elliptical paraboloid	[m]
h_{tcc}	Thermal contact conductance	[W/(Km^2)]
E^*	Reduced elastic modulus	[Pa]
F	Load (Force)	[N]
f	Frequency	[Hz]
f_{hk}	Interfacial shear factor	[–]
G	Geometrical factor of a lump	[m]
H	Hardness	[Pa]
K	Thermal conductivity	[W/(Km)]
L	Lubrication number	[–]
L_H	Latent heat of fusion	[J/Kg]
l	Length of various kinds	[m]
M	Moment of various kinds	[N·m]
m	Constant in Sellars–Tegart flow stress	[–]
m_0	Moment of surface PSD	[m^2]
m_2	Moment of surface PSD	[–]

m_4	Moment of surface PSD	[m^{-2}]
m_a	Magnification factor in the physical model	[m/N]
N	Number of calculation cycles	[–]
n	Number of summits / asperities / contact patches	[–]
n_{str}	Strain hardening sensitivity	[–]
n_{strrt}	Strain rate sensitivity	[–]
P	Nominal contact pressure at a particular location / time during the extrusion cycle	[Pa]
P	Power spectrum density	[W/Hz]
p	Normal pressure	[Pa]
p_x	Sampling interval in the x direction	[m]
p_y	Sampling interval in the y direction	[m]
Q	Thermal activation energy	[J/mol]
R	Universal gas constant	[J/(molK)]
R_a	Centre Line Average surface roughness value	[m]
R_q	Root Mean Square surface roughness value	[m]
r	Ratio of various kinds	[–]
r_H	Hardness ratio	[–]
s	Surface slope	[–]
s	Summit height	[m]
s_m	Constant in Sellars–Tegart flow stress	[Pa]
T	Temperature	[K]
T_m	Melting point	[K]
t	Thickness of the extrusion profile	[m]
V	Volume	[m^3]
v	Velocity	[m/s]
v^+	Sum velocity used in lubrication	[m/s]
w	Width of the extrusion profile	[m]
x	Coordinate in the x direction; measuring distance	[m]
Z	Zener–Hollomon parameter	[–]
z	Local surface height	[m]

Greek symbols

α	Degree of contact	[–]
α_{db}	Bearing angle	[^{o}]
β	Tip radius of an asperity	[m]

δ	Height of a lump	[m]
Δt	Time interval	[s]
$\Delta\gamma$	Interfacial work of adhesion	[N/m]
γ	Surface free energy	[N/m]
ε	Strain	[–]
$\dot{\varepsilon}$	Strain rate	[s^{-1}]
ζ	Elasto–plastic recovery angle	[rad]
η	Dynamic viscosity	[Pa•s]
θ	Attack angle of an asperity	[rad]
κ	Tip curvature of an asperity	[m-1]
λ	Ellipticity ratio	[−]
μ	Coefficient of friction	[–]
ν	Poisson's ratio	[–]
σ	Standard deviation	[m]
σ	Stress	[Pa]
σ_V	Von–Mises stress	[Pa]
τ	Shear stress	[Pa]
$\Phi(z)$	Surface height probability density function	[–]
$\Phi(s)$	Summit height probability density function	[–]
φ	Orientation angle of an elliptical paraboloid	[rad]
χ	Three dimension shape factor	[–]
ξ	Dimensionless surface separation	[–]
Ψ	Plasticity index	[–]
ψ	Bandwidth parameter	[–]
ω	Contact interference (flattened distance in elastic contact and indentation depth in plastic contact)	[m]
$\overline{w}$	Dimensionless contact interference	[–]

Suffixes

abr	Abrasive
adh	Adhesive
al	Aluminium
asp	Aspect ratio
bil	Billet
br	Breakthrough in extrusion

cp	Contact patches
cr	Critical (values)
db	Die bearing
eff	Effective
el	Purely elastic
end	End of stroke
ent	Bearing entrance
ep	Elasto – plastic
epp	Elliptical paraboloid
eqv	Equivalent
ext	Extrudate / Exit / Extrusion
fe	Steel
fr	Friction
f	Flow (stress)
fl	Flash (temperature)
i	i-th contact object; i-th asperity
ini	Initiation
int	Properties of the interface
lump	Lump
M	Moment
mj	Major (contact radius)
mn	Minor (contact radius)
N	Normal direction
n	Nominal
pl	Fully plastic
rep	Representative
s	Summit
sl	Sliding
slp	Slipping (zone)
st	Static
stk	Sticking (zone)
T	Tangential direction
trans	Transition of different deformation modes
x	In x direction
xx	Normal to the x direction
y	In y direction
yy	Normal to the y direction

*	Combined parameter, composed of multiple parameters

Abbreviations

AA	Aluminium Alloys
ABS	Acrylonitrile Butadiene Styrene
BL	Boundary Lubrication
CLA	Centre Line Average (roughness)
DF	Dry Friction
DMZ	Dead Metal Zone
EDM	Electrical Discharge Machining
EDX	Energy Dispersive X-ray spectroscopy
EHL	Elasto–Hydrodynamic Lubrication
FEA	Finite Element Analysis
FEM	Finite Element Method
FIB	Focused Ion Beam
LSCM	Laser Scanning Confocal Microscopy
ML	Mixed Lubrication
PCG	Periphery Coarse Grain
PDF	Probability Density Function
PSD	Power Spectrum Density

Table of contents

Chapter 1
Introduction

1.1 Extrusion process

The extrusion process was invented by Joseph Bramah in 1797 when he extruded a lead pipe; since then extrusion has firmly become a major industrial application. The extrusion process converts a billet of material into a continuous length of generally uniform cross section by forcing it to flow through a die with an opening shaped to produce the desired form of product. Generally this is a hot working operation, the material being heated to some certain temperature until it possesses a suitable flow stress. It is cost-effective, very efficient and highly developed with minimum material waste, and in this respect it certainly has no rival among industrially produced long products with complex cross sections. Examples of everyday use of extrusion are shown in Fig.1.1:

(a) (b)

Fig.1.1 Examples of extrusion: (a) the escalator of London's "tube" system in which the handles are produced by extrusion; (b) a fleck of toothpaste is being extruded out of the tube.

The essential principles of the extrusion process are presented in Fig. 1.2, together with the distinction between two methods of operation, known as direct and indirect extrusion. The distinction depends on the layout of the tooling [1]. In direct

extrusion, the material to be extruded is pushed by a ram towards the die located at one end of the container, therefore moving relative to the container, as seen in Fig. 1.2(a). In indirect extrusion, the die is placed on the end of the bored ram, with the container holding the material pushing against the hollow ram, as seen in Fig. 1.2(b).

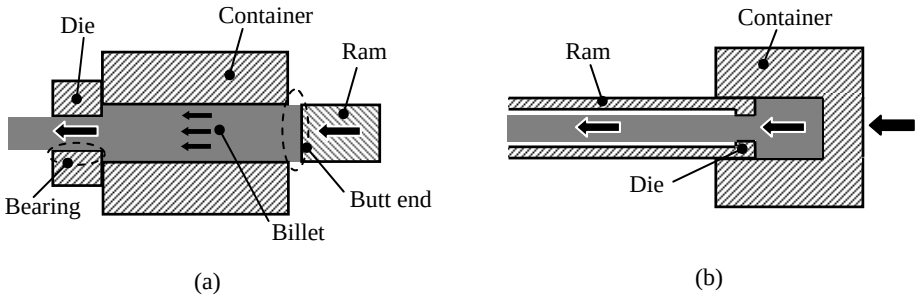

Fig. 1.2 Direct and indirect extrusion: (a) Arrangement of direct extrusion; (b) Arrangement of indirect extrusion.

The main difference between these two operations is that there is no friction between the billet and the container in indirect extrusion, whilst large friction, usually approaching shear strength of the material, exists in between the billet and the container in direct extrusion. As a result, the main advantage of using indirect extrusion is that the load required from the ram is 25–50% lower compared to direct extrusion, therefore permitting higher extrusion speeds. However, the lack of friction inside the container means that the contaminants on the billet surface are not automatically retained in the "butt end" (illustrated in Fig. 1.2 (a)) which can be discarded at the end of the process, as found in direct extrusion. Therefore, the product surface usually needs machining. This fundamental downside limits the extensive application of indirect extrusion [1].

The materials that can be extruded range from thermoplastic polymers to various metals. This thesis deals exclusively with the extrusion of aluminium alloys.

1.2 Aluminium extrusion

1.2.1 Overview of the process

Aluminium is one of the most utilised and applied metals nowadays, only second to

steel, because of its high strength to weight ratio and superior corrosion resistance. It was made commercially available in 1886 [2]. About half of the aluminium is used in the extrusion industry [3], due to its superb extrudability. Aluminium extrusions are used in a large number of applications, including commercial and domestic buildings for window and door frame systems, prefabricated houses/building structures, roofing and exterior cladding, curtain walling, shop fronts, etc., as illustrated in Fig. 1.3:

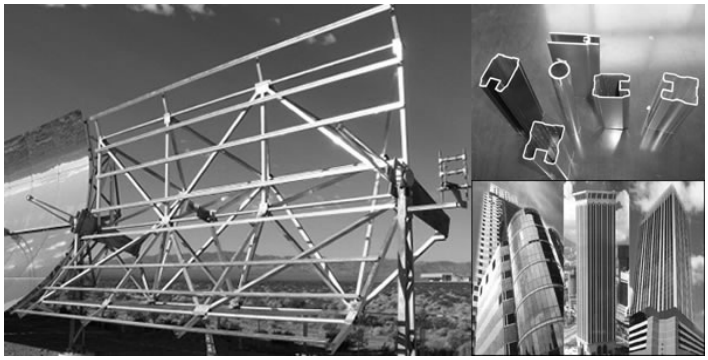

Fig. 1.3 Various aluminium extrusion products.

Various elements can be added to pure aluminium to make aluminium alloys. They are usually divided into two categories according to whether they are strengthened by work hardening (1XXX, 3XXX, 4XXX and 5XXX series) or precipitation hardening (2XXX, 6XXX and 7XXX series). Among them, the 6XXX series aluminium alloys (aluminium–magnesium–silicon alloy) are considered the "flagship" in the extrusion industry due to their excellent formability, superb surface finish and corrosion resistance [1].

In order to achieve a good surface quality of products that do not need post–extrusion machining, aluminium extrusion usually adopts the direct extrusion arrangement, without the addition of any lubricants between the tooling and the billet or extrudate. This arrangement enables maximum friction at the billet–container interface, thus allowing shearing of the billet surface and leaving the oxide layer and surface contaminants in the "butt end (illustrated in Fig. 1.2 (a))" that will be cut off from the extrudate as a finishing treatment. The billet temperature required for the extrusion process is usually 400 - 500 ºC, depending on the alloy composition and profile to be extruded. Due to intensive plastic deformation, the exit temperature can generally rise up to close to the material melting point. After the process, the exiting extrudates are stretched for strain

hardening and moderate straightening. The anodising or powder coating is usually the last treatment extrusions will undergo, before being delivered to customers.

1.2.2 Extrusion defects

Extrusion defects can generally be categorised according to their origins: operational related defects, metallurgical defects and defects caused by operating the process outside the process window [1]:

- Operational defects:

Operational related defects include the well-known “back–end” defect where the sheared billet surface flows towards the centre of the billet at the back end of the extrudate, extending beyond the “butt–end” which will be discarded at the end of the process. Since the original billet skin usually contains oxide layers, surface contaminants and voids, this region is associated with impaired mechanical properties. This often results in scrapping the back–end materials. Possible solutions include use of a ram with a diameter somewhat smaller than the container to deviate the billet surface, and heating the billets in an inert environment. The contaminated billet skin is also the cause of transverse weld and longitudinal weld problems as it forms a region with deteriorated mechanical properties where materials merge, for example the billet–billet interface as in transverse weld defect, and the re-welding of materials extruded from hollow dies, as in longitudinal weld problems. Another type of defects in this category is where blistering occurs during the extrusion process because the entrapped air or volatile lubricants form bulges on the product surface.

- Metallurgical defects:

Problems occurring due to metallurgical defects usually involve poor ingot quality or improper homogenisation prior to extrusion. The heterogeneous billet microstructure and undesirable presence of second phase particles such as coarse Mg_2Si particles substantially decrease extrudability and cause various problems such as eutectic melting and tearing, surface streaks, hot spots due to accidental localised contact with the run out table, severe abrasive wear due to coarse second phase particles, etc.

- Defects occurring by operating the process outside the process window:

In order for the product to satisfy stringent geometric, cosmetic and property specifications, interaction between process variables needs consideration. To be more specific, the various parameters that can be adjusted for one particular extrusion need to lie in some certain process window. This process window can be visualised by constructing a "limit diagram" indicating the appropriate use of extrudate temperature, exit speed as well as extrusion ratio. One can locate the process window by finding the area bounded by curves representing different loci [1]: 1) Pressure restriction (curve A); 2) Surface damage (curve B). 3) Required microstructure of the extrudate therefore mechanical properties are desirable (curve C). Such a diagram is schematically shown below [4]:

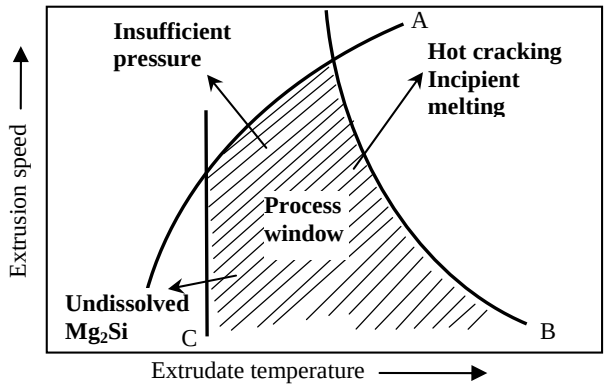

Fig. 1.4 Limit diagram (schematic) for aluminium extrusion.

The shaded area in the limit diagram indicates the appropriate working area for a specific extrusion process, depending on the alloy type and extrusion setup. Operating the extrusion process outside the process window, i.e., extrudate temperature and extrusion speed for a certain extrusion ratio, causes insufficient pressure input or, on the other hand, surface problems such as hot cracking and tearing.

1.2.3 Defects occurring within the process window

As mentioned above, operating the extrusion process outside the process window leads to various product defects. However, a number of defects can still arise when the extrusion is operated within the process window. Die lines and surface pickups are, among them, the most severe and relevant to the AA 6XXX series alloys. They can virtually appear throughout the process window.

Die lines are longitudinal depressions or protrusions formed on the product surface. A good measure of the severity of the die line defect is the roughness of the extruded surface. Die lines can be categorised into macro die lines and micro die lines. Macro die lines are formed inside the bearing area (as shown in Fig. 1.2 (a)) and are closely related to the roughness of the die bearing surface. Micro die lines are much less deeper and are attributed to linear alignment of cavitations interspersed with the fractured iron phase precipitates [1]. Impressions of die lines are shown below:

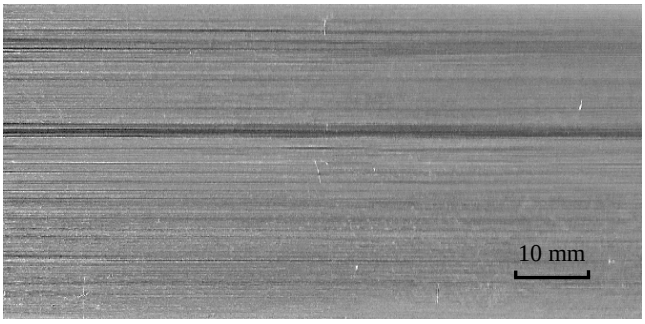

Fig. 1.5 Appearance of die lines on AA 6063 surface.

Pickups are observed as intermittent score lines and often terminate with a fleck of aluminium debris that rises above the extrudate surface. Since the deposits can be as long as several hundreds of microns, they will not readily be eliminated in the anodising process and can cause numerous aesthetical and functional problems [5]. So far there is yet no sound physical model by which formation of pickups can be described; some [6] suggested that local melting is responsible for pickup formation, others [7] claim that the defect is formed as a result of the peritectic reaction of $AlMg_2Si$ and β - AlFeSi at 576ºC, while others [1][2] concluded that formation of pickups is not related to metallurgical features as they can form both above and below the eutectic point; rather, it is a mechanical process that is associated with the transfer of material between the extrudate and the die bearing surface, and it can be enhanced by inclusions in the cast and inadequate homogenisation treatment. A typical impression of the pickup is shown below [7]:

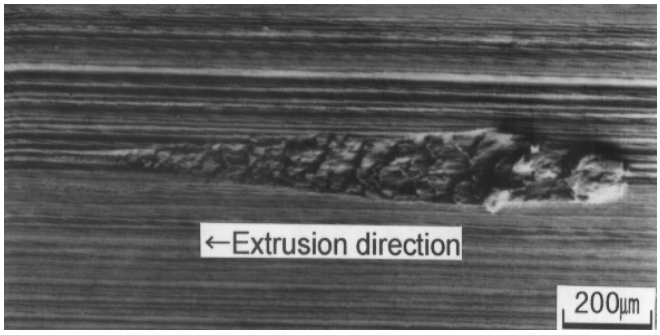

Fig. 1.6 Appearance of a pickup defect on AA 6063 surface.

In the literature it is mentioned that surface quality should be judged by: 1) surface roughness and reflection of the surface; 2) ability for anodic oxidation. Research has shown that the increase of roughness value is associated with surface pickup, deteriorating the overall surface quality [4]. Hereafter surface defects and surface pickups are interchangeably used in the context that severe surface defects occurring in the process window are of surface pickup origin.

1.3 Objectives of this research

This research aims at understanding the formation mechanisms of surface defects of aluminium extrusions occurring when the process window (the shaded area in Fig. 1.4) is conformed to, therefore issues such as hot cracking and surface tearing are not within the scope of this study. The main focus is surface pickups, as they are the primary decorative problem. The objectives are threefold:

- Investigate and understand factors contributing to pickup formation.
- Development of an experimentally validated physical model by which the damage mechanism can be described.
- In combination with numerical simulation of the extrusion process, the development of a surface quality predictor, with which the extrusion process can be tailored with respect to surface quality.

1.4 Overview of this thesis

This thesis focuses on modelling the formation of defects on the surface of aluminium extrusion products. AA 6063 has been chosen to be the subject of this

study since it is one of the most extruded alloys due to its excellent extrudability. The thesis is composed of four main sections: in Chapter 2, 3 and 4 a load dependent contact and friction model, coupled with the constitutive behaviour of the studied alloy, is presented; in Chapter 5, 6 a physical model is developed to quantitatively describe formation of surface defectss. In Chapter 7 this physical model is combined with FEM results to represent the “surface quality predictor”. Further, they illustrate how the process can be controlled and optimised to diminish its onset. In Chapter 8 the developed physical model is subject to validation. Finally in Chapter 9 conclusions and discussions are presented.

To be more specific, chapter 2 deals with an introduction of the tribological system in the aluminium extrusion process and how various process parameters can be related to controlling surface defects, based on a survey of the literature. Chapter 3 is devoted to developing a new contact and friction model that considers change of contact geometry with load — a load dependent contact and friction model. The contact model is also adopted to account for the constitutive behaviour of the studied alloy AA 6063. Chapter 4 describes the laboratory scale split die extrusion experiments and the use of sticking / slipping lengths to verify the friction model.

The formation mechanism for surface defects is studied in detail in chapter 5. The study is based on microstructural and morphological analysis of the pickups. In Chapter 6, a physical model is developed to account for such a formation process. Chapter 7 demonstrates pickup measurements on samples taken from the split die extrusion experiments. Using temperature and extrusion speed measured during the extrusion process, results from the developed physical model can be compared with the actual results obtained from the extrusion experiments.

In Chapter 8 the physical model is coupled with FEM simulation of several extrusion processes. Guidelines can thus be given as to how pickups can be eliminated or diminished by opting for the right combination of process parameters. Finally, in chapter 9 conclusions for this research are drawn; discussions are made and recommendations are proposed for extruders and future researchers.

Chapter 2
Tribology and aluminium extrusion

2.1 Tribology: Contact and friction

In this section, the general principles regarding contact and friction between two rough surfaces are introduced. First, the concept of contact and contact models are presented, and then friction in dry and lubricated conditions is introduced.

2.1.1 Contact between rough surfaces

2.1.1.1 Surface roughness and microgeometry

Engineering surfaces are far more complicated than merely a simple plane; in fact, all known surfaces, apart from the cleaved faces of mica [8], are rough. This roughness means that the surface is composed of peaks and valleys, and it illustrates that the real contact area between two surfaces is merely a fraction of the apparent or nominal contact area, as schematically illustrated in Fig. 2.1:

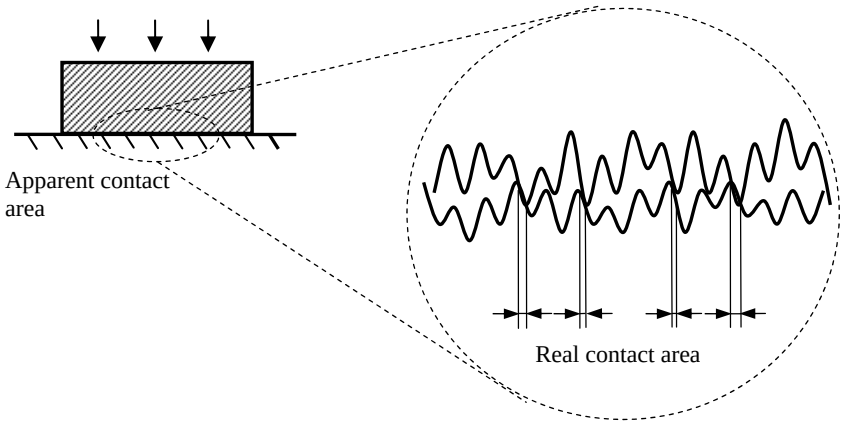

Fig. 2.1 Apparent and real contact area.

The surface height distribution of an engineering surface is usually random unless some regular features have been deliberately introduced. The randomness can be described by some surface height probability density function $\Phi(z)$, and two sets of parameters are introduced that are associated with this surface height probability density function (PDF):

- Height parameters

The roughness of a surface can usually be characterised by some statistical data. For a given set of surface height data $z(x)$, the arithmetic mean R_a and the root mean square R_q are represented in Eq. (2.1) and Eq. (2.2), in which z_0 is the reference value of the dataset, as shown in Fig. 2.2:

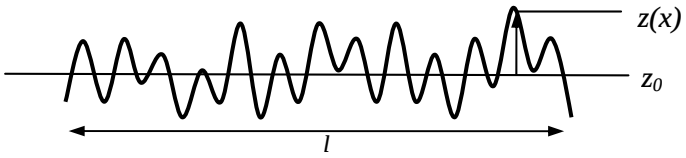

Fig. 2.2 Random characteristics of an engineering surface (height profile).

Considering measurements taken in x and y directions which correspond to a measured area rather than a length, the arithmetic mean and root mean square (RMS) values can be written in the 3 – D form:

$$R_a = \frac{1}{l_x l_y} \int_{y=0}^{l_y} \int_{x=0}^{l_x} |z(x,y) - z_0| dxdy \tag{2.1}$$

$$R_q = \sqrt{\frac{1}{l_x l_y} \int_{y=0}^{l_y} \int_{x=0}^{l_x} |z(x,y) - z_0|^2 dxdy} \tag{2.2}$$

Since R_a represents the average roughness over the sampling area, one of the main disadvantages of using this parameter is that it can give identical values for surfaces with completely different characteristics. Since the RMS parameter is weighted by the square of the heights, it is much more sensitive to deviations from the reference line.

- Spatial parameters

However, a surface cannot be fully defined merely by its height parameters, as two surfaces that essentially have the same height parameters can be rather different, simply by aligning “ridges” of the same height more densely on one surface than the other. Therefore, a set of parameters is introduced to overcome this ambiguity by incorporating the spatial alignment of the surface: the autocorrelation function $A_{cr}(d)$ which indicates the similarity of surface features measured d distance away from the original measuring point, and the power spectrum density (PSD) of the surface height, which is the Fourier transform of the autocorrelation function and transforms the spatial surface height distribution to a random signal with a mixture of frequencies. For a measuring area of $l_x \cdot l_y$, the following expressions hold [9]:

$$A_{cr}(d_x, d_y) = \frac{1}{l_x l_y} \int_{y=0}^{l_y} \int_{x=0}^{l_x} z(x,y) z(x+d_x, y+d_y)\, dxdy \tag{2.3}$$

$$P(f_x, f_y) = \frac{1}{4p^2} \iint_{\pm\infty} A_{cr}(d_x, d_y) \exp\left[-i(d_x f_x + d_y f_y)\right] dd_x dd_y \tag{2.4}$$

For isotropic surfaces, a set of moments of the surface PSD can be derived:

$$m_0 = \iint_{\pm\infty} P(f_x, f_y) df_x df_y = s_z^2 \tag{2.5}$$

$$m_2 = \iint_{\pm\infty} P(f_x, f_y) f_x^2 df_x df_y = s_s^2 \tag{2.6}$$

$$m_4 = \iint_{\pm\infty} P(f_x, f_y) f_x^4 df_x df_y = s_k^2 \tag{2.7}$$

In which suffixes σ_z, σ_s, σ_κ stand for the standard deviations of the surface height (R_q when $z_0 = \bar{z}$), the surface slope and the surface curvature, respectively. In Chapter 3 it is shown that these three moments can affect the friction calculation.

To obtain a continuous surface height PDF is not always feasible, and a practical way of obtaining all the parameters above is by measuring the surface height digitally. The result of such measurement is a surface height matrix including surface height data at each measurement location. It can be done using several

means, e.g. surface profilometry or interference microscopy. The set of surface height data is usually pre-processed before putting into use [10], and this involves filling up the missing points by interpolation from its neighbouring points, and removing the "spikes" by allowing a maximum local slope to occur in the surface. Settings like the sampling frequency (resolution of the roughness measurement) and limitations of the measuring apparatus can affect the outcome quite significantly. Digital measurement enables the slope and curvature of a surface to be obtained in a discrete manner [11] [12]:

$$s_x = \left|\frac{z(x,y) - z(x+p_x,y)}{p_x}\right|; s_y = \left|\frac{z(x,y) - z(x_x,y+p_y)}{p_y}\right|; \quad s(x,y) = \frac{s_x + s_y}{2} \tag{2.8}$$

$$k_x = \left|\frac{z(x-p_x,y) - 2z(x,y) + z(x+p_x,y)}{{p_x}^2}\right|;$$

$$k_y = \left|\frac{z(x,y-p_y) - 2z(x,y) + z(x,y+p_y)}{{p_y}^2}\right|;$$

$$k(x,y) = \frac{k_x + k_y}{2} \tag{2.9}$$

The calculated values can then be related to obtaining the moments of surface PSD.

An important aspect of the surface height is the summits. They are points with a local surface height higher than their neighbouring points. Summits are very important since in most cases contacts are assumed to only occur on the summits, thus contributing crucially to the tribological behaviour. The nine – point definition of a summit is often used because this minimises the probability of identifying "false summits", as illustrated in Fig. 2.3:

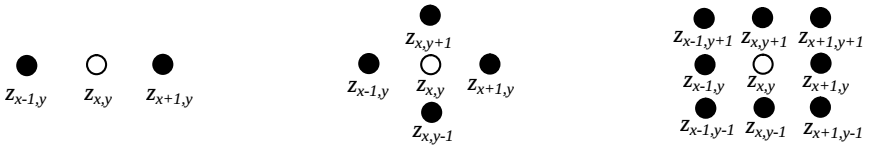

Fig. 2.3 Summit definitions.

Following the approach by Greenwood and Williamson [13], all the summits are considered to be spherically tipped, and the tip radius of the summits can be related to the local curvature calculated according to Eq. (2.10):

$$b = k^{-1} = \frac{2}{k_x + k_y} \tag{2.10}$$

2.1.1.2 Overview of contact models

Now that the contacting surfaces are characterised as introduced in section 2.1.1.1, a contact model needs to be applied to the surfaces in order to model tribological behaviour of the contacting pair. However, contact conditions are extremely versatile; to find a model suitable for any of these conditions is almost out of the question. There are quite a number of existing contact models, each being suitable for a certain range of operating conditions, depending on the assumptions made in their contexts. An overview of contact model types is summarised in Table 2-1:

Table 2-1 Overview of contact model types.

	Features	Model characteristics	Literatures (not conclusive)
Contact models	Contact pattern	Summits	Greenwood [13], Chang [14]
		Contact patches	Nayak [15]
	Deformation mode	Purely elastic	Greenwood [13]
		Fully plastic	Pullen and Williamson [16]
		Elasto - plastic	Zhao [17]
	Contact condition	Static contact	Above
		Sliding contact	Masen [18]
	Geometry of contact	Spherical	Greenwood [13]
		Others	De Pellegrin [19], Ma [20]

To model contact and friction in aluminium extrusion, a sliding contact with elliptical paraboloidal-shaped asperity contact model has been developed and applied, based on contact patches rather than summits. In the next section only fully plastic contact models are presented. However, it will be shown in Chapter 3 that the summit-based model is not appropriate in aluminium extrusion, therefore

in the next section any fully plastic contact models based on summits are not included. The summit-based contact models are elaborated in Appendix A.

2.1.1.3 Fully plastic contact models

When the normal load is large or surface asperities are sharp, plastic deformation of the soft surface is dominant and elastic recovery can be neglected. In this case a fully plastic contact model will suffice. This occurs if the plasticity index Ψ is greater than 2, according to [11]:

$$\Psi = \frac{E^*}{H}\sqrt{\frac{\sigma^*}{\beta^*}} \tag{2.11}$$

The H value represents the hardness of the softer surface in the contacting pair, and the overhead bar refers to an average value. As a two-rough-surface contact can be reduced to the contact between a perfectly smooth surface and a surface with equivalent surface roughness, the combined parameters in Eq. 2.11 can be expressed as [10]:

$$\frac{1}{b^*} = \frac{1}{b_1} + \frac{1}{b_2}; \qquad s^* = \sqrt{{s_1}^2 + {s_2}^2}; \quad \frac{1}{E^*} = \frac{1-{u_1}^2}{E_1} + \frac{1-{u_2}^2}{E_2} \tag{2.12}$$

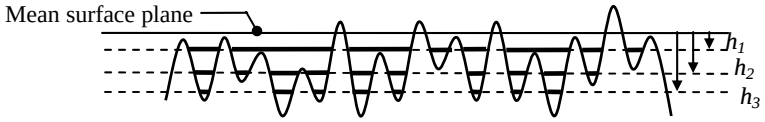

Fig. 2.4 Contact area in fully plastic contact (bold lines indicating real contact area at different separation levels).

A surface separation h is defined as the distance between the smooth surface of the mean plane of the rough surface as shown in Fig. 2.4. In fully plastic contact conditions the deformation of the harder surface is negligible, therefore the degree of contact (ratio between true contact area and nominal contact area) at a certain surface separation h, is exactly equivalent to the complementary cumulative distribution function of the surface PDF of the rough surface in the contacting pair (truncation of the rough surface):

$$a(h) = \int_{h}^{+\infty} f(z)dz \tag{2.13}$$

The degree of contact for a random surface that has a Gaussian PDF is illustrated in Fig. 2.5(a). Plastic deformation ensures that the pressure in the contact area equals the hardness of the softer material, yielding the following expressions:

$$a = \frac{p_n}{H} \tag{2.14}$$

Combining Eq. 2.13 and Eq. 2.14 the surface separation and contact can be solved, given an input nominal contact pressure. However, Eq. 2.14 is only valid if the bulk material is free to deform. In an extrusion process such deformation is restrained by the bearing surfaces and the high pressure in the extrusion direction that is present in the extrudate. It was experimentally observed by Pullen and Williamson [21], that if the plastically deformed material is constrained and bulk deformation is not allowed, the linear increase of degree of contact with the nominal contact pressure is not valid when $p_n > 0.3H$, as plastically deformed material requires additional energy to displace to the "open" space between the two surfaces due to volume conservation. The degree of contact is:

$$a = \frac{p_n}{H + p_n} \tag{2.15}$$

A comparison is made between with or without considering volume conservation in Fig. 2.5 (b):

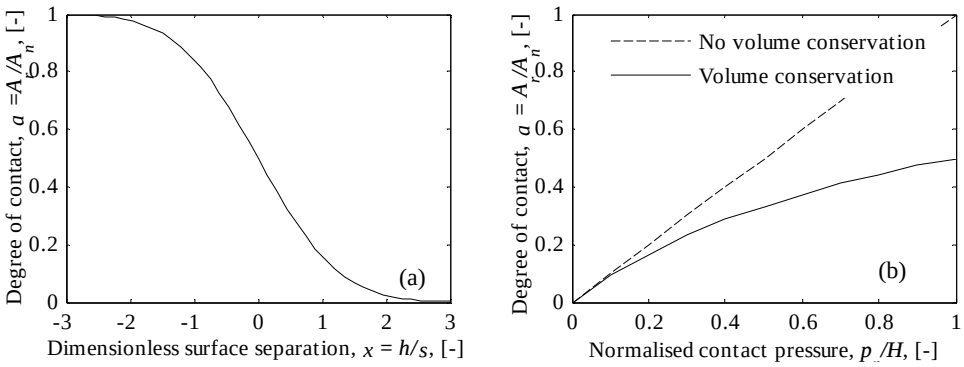

Fig. 2.5 Fully plastic contact models: (a) Degree of contact as a function of the surface separation for surfaces with a Gaussian height distribution; (b) Degree of contact as a function of nominal contact pressure (normalised by hardness) including volume conservation.

The above-mentioned fully plastic contact models have some obvious shortcomings for our study:

- They are only applicable for perfectly plastic material. Therefore, no hardening or softening of the contacting material is taken into account.
- They do not give geometrical information of the contact area, which is essential in modelling friction.

2.1.2 Friction

An essential constitute of tribology is friction. When two bodies are in contact and move relative to each other, friction arises that manifests itself as a force opposing the relative motion. The magnitude of this opposing force can be measured by the coefficient of friction, defined as the ratio between the tangential and normal forces, or between the shear stress and normal stress present in a contacting pair:

$$m = \frac{F_T}{F_N} = \frac{t}{p} \tag{2.16}$$

The coefficient of friction is affected by the physical and chemical attributes of the contacting surfaces, and is crucially related to the addition of lubricants, which are either naturally present or artificially applied to decrease friction and prevent wear. Depending on the operating conditions, a tribological system can operate in one of

the following regimes: Elasto–Hydrodynamic Lubrication (EHL), Mixed Lubrication (ML), Boundary Lubrication (BL) and Dry Friction (DF). In this section they will be discussed.

2.1.2.1 Lubricated friction

A vast majority of engineering tribological systems are lubricated to some extent. Lubricants can range from purposefully introduced substances such as synthetic oil or grease, to physically or chemically absorbed layers formed on a surface [22]. In the case of two lubricated surfaces sliding against each other under a normal load, three different lubrication regimes can be distinguished[1] [23], as shown in Fig. 2.6:

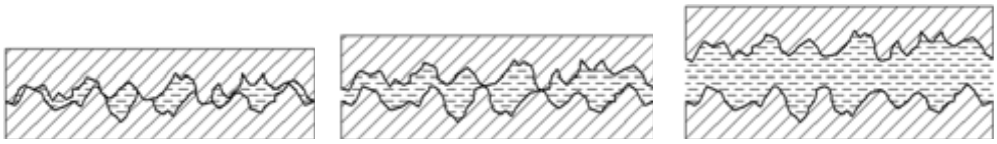

Boundary lubrication Mixed lubrication Elasto–hydrodynamic lubricaiton

Fig. 2.6 Lubrication regimes.

- Boundary Lubrication (BL): The normal load is carried completely by contacting asperities on two surfaces. These surfaces are protected from dry friction by thin boundary layers attached to the surfaces. Friction in this regime is controlled by shearing of the boundary layers built on the surfaces of the solid bodies. The value of the coefficient of friction in this regime is of the order 0.1.

- Mixed Lubrication (ML): The normal load is carried partially by contacting asperities, and partially by the lubricant film. In this regime friction is controlled by the interacting asperities as well as by the fluid between the surfaces. Typical value of the coefficient of friction ranges from 0.01 to 0.1.

- Elasto–Hydrodynamic Lubrication (EHL): The load is entirely carried by the lubricant film. Contact of surfaces does not occur. The hydrodynamic pressure of the film may elastically deform the solid surfaces. In this regime the coefficient of friction is merely governed by the rheological properties of the lubricant and is typically of the order 0.01.

[1] A fourth regime, plasto – hydrodynamic lubrication (PHL) is when one of the bodies deforms plastically while a full fluid film is maintained. This situation can occur in some metal forming processes, e.g. rolling, hydrostatic extrusion.

The coefficient of friction can be plotted against operating conditions, i.e. velocity, pressure etc. in the generalised Stribeck diagram, in which the three regimes can be distinguished, as shown in Fig. 2.7.

The lubrication number L – number is defined by Schipper [24]:

$$L = \frac{hv^{+}}{p_n R_a} \tag{2.17}$$

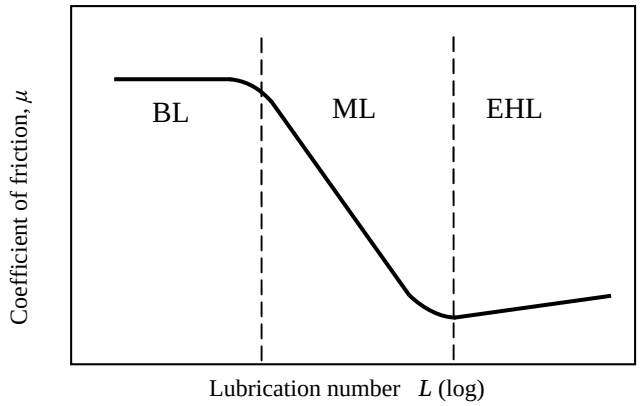

Fig. 2.7 Generalised Stribeck diagram.

η represents the dynamic viscosity of the lubricant; v^{+} is the sum velocity of the two surfaces; p_n is the nominal contact pressure and R_a is the centre line average (CLA) of the surfaces. With increasing lubrication number the three lubrication regimes can be distinguished with different tribological characteristics, as introduced above.

2.1.2.2 Dry friction

Yet when no lubricant layer of any sort is present between the contacting surfaces, the tribological system is operating under dry friction conditions. Strictly speaking, dry friction condition can only be achieved in an evacuated environment since surface contaminants such as an oxide layer or absorption of water vapour immediately form on a surface under exposure to an atmosphere with a total pressure as low as 10^{-2} Pa, which radically alter friction and wear behaviour [25]. However, this oxide layer is usually very thin (from nm to μm) and does not

contribute to the load–bearing characteristics and thus contact between two surfaces. Therefore one usually refers the dry friction condition to a tribological system in which no lubricant substance is intentionally introduced, i.e. an unlubricated contact. Tverlid [26] and Bjork [27]concluded from their laboratory extrusion experiments that the atmospheric condition in the bearing area of extrusion dies is partial oxidation of the aluminium extrudate surface, therefore, the conventional definition of dry friction also applies to this thesis. In the current study, the effect of oxidation has not been quantitatively studied, but the effect will be discussed in Chapter 9. In this section the characteristics of dry friction for a single asperity are discussed at length.

Dry friction condition results in a high degree of friction and wear, due to extensive abrasive and adhesive actions between the contacting surfaces without protection from lubricants. The coefficient of friction can be generally split into an abrasive component and an adhesive component [28], which can be illustrated in Fig. 2.8:

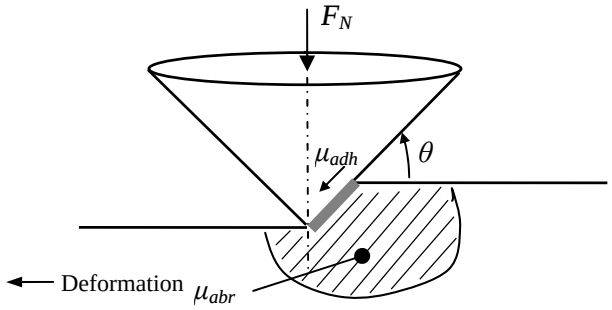

Fig. 2.8 Abrasive and adhesive components of friction.

- Abrasive component

The abrasive component of friction arises from the deformation of the softer material. The abrasive component is negligible when the deformation is purely elastic [29]. Relatively straightforward expressions for the abrasive component of the coefficient of friction can be established for the abrasive component only considering deformation of the softer surface with a simple geometry. Under the fully plastic deformation conditions, for a conical slider [30]:

$$m_{abr,pl} = \frac{2}{p}\tan q \tag{2.18}$$

In which the attack angle θ for a cone is illustrated in Fig. 2.8. Similarly, for a

spherical slider, the abrasive coefficient of friction can be written as [31]:

$$m_{abr,pl} = \frac{2}{p}\frac{q - \sin q \cos q}{\sin^2 q} \tag{2.19}$$

When elastic recovery for elasto–plastic deformation is considered, the recovered part of material alters friction. For a conical asperity [32]:

$$m_{abr,ep} = \frac{2}{p}\tan q\left[\frac{p\cos z\,(1-\sin z)}{p + 2z + \sin(2z)}\right] \tag{2.20}$$

In which the elasto–plastic recovery angle ζ has been fitted by Masen [33] using data from [34]:

$$z = 0.7\left(\frac{E}{H}\tan q\right)^{-0.6} \tag{2.21}$$

In the case of a spherical slider operating under elasto–plastic condition the abrasive friction coefficient can be written [35]:

$$m_{abr,ep} = \frac{2\left[c^2 \arcsin(a\cos z / c) - a\cos z\sqrt{c^2 - a^2\cos^2 z}\right]}{a^2[p + 2z + \sin(2z)]} \tag{2.22}$$

In which the contact radius a and geometry parameter χ can be related to the attack angle θ:

$$a = b\sin q \tag{2.23}$$

$$c = \sqrt{b^2 - a^2\sin^2 z} \tag{2.24}$$

The abrasive component of coefficient friction for conically and spherically shaped asperities is only dependent on the attack angle θ and can be shown below:

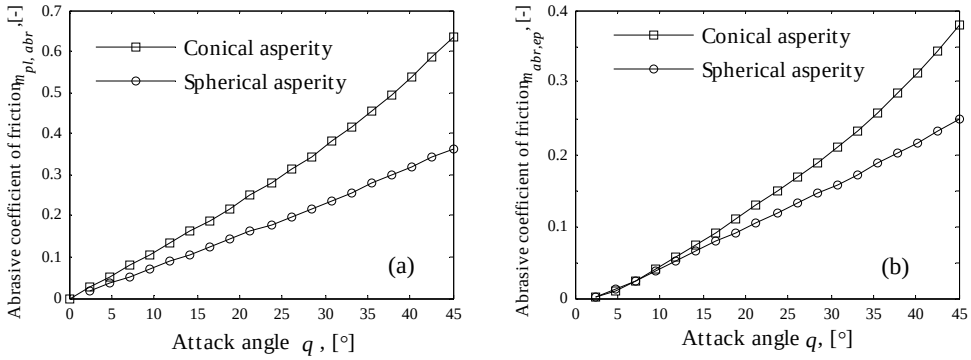

Fig. 2.9 Abrasive component of the coefficient of friction: (a) Fully plastic; (b) Elasto–plastic (*E/H* = 16 for ABS).

It can be seen that the abrasive coefficient of friction increases with increasing attack angle values, suggesting its direct relation to the severity of deformation of the softer surface. Elasto–plastic condition reduces the coefficient of friction at the same attack angle value due to elastic recovery at the rear part of the asperity.

- Adhesive component

The adhesive component of the coefficient of friction is related to the adhesion force between the two bodies, resulting from interfacial interactions such as the electron transfer at metal–metal interfaces, Van der Waals force at metal–polymer interfaces and chemical bonding at metal–ceramic interfaces [36]. The adhesive coefficient of friction can be expressed by:

$$m_{adh} = \frac{t_{\text{int}}}{H} \tag{2.25}$$

The upper limit for the shear strength of the interface is that of the bulk material since the bulk would start to shear if the interface is any stronger. Therefore, the theoretically possible μ_{adh} value is approximately 0.2, which is far lower than the extremely high and fluctuating observed values between metal–metal contact in an evacuated environment. This can be explained by two phenomena occurring when adhesive friction is very large, e.g. in high vacuum environment [36]: firstly, junction growth resulting from presence of shear stress which increases the contact area and thus allowing the normal pressure to be lower than the hardness, as shown in Fig. 2.10 (a) and (b); secondly, production of adhesive transfer particles that render high friction, normally observed as a transfer film of the softer material, as

shown in Fig. 2.10 (c) and (d):

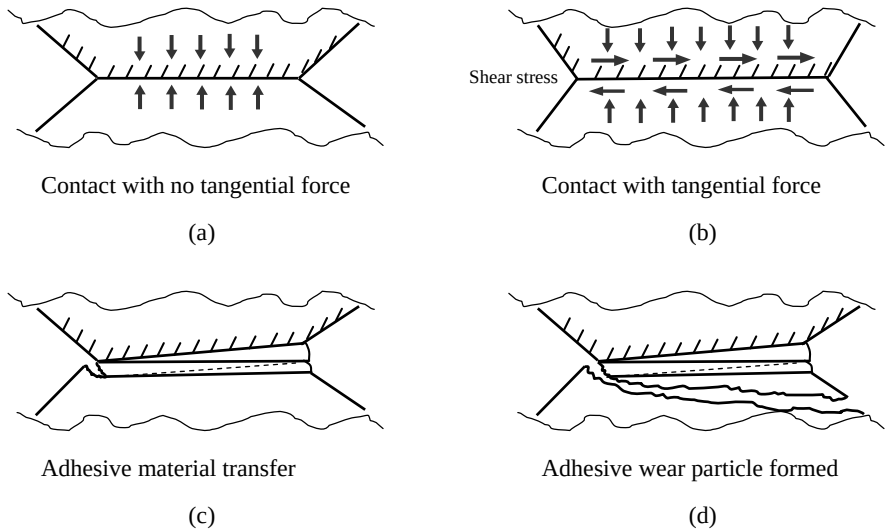

Fig. 2.10 Reasons for extremely high and fluctuating coefficient of friction observed during metal – metal contact in an evacuated environment: (a) and (b) Junction growth; (c) and (d) Formation of adhesive transfer particles.

It is thus very difficult to describe friction when adhesion is large between two contacting bodies.

2.1.2.3 Modelling dry friction — the Challen and Oxley model

The above-mentioned friction models have limitations in that: 1) contribution of "pile up" of the deformed material is not taken into account; 2) the two components of friction cannot be readily combined. This is solved by Challen and Oxley [37] by constructing permissible slip–line field in the deformation zone beneath the asperity. The model assumes a triangularly shaped rigid asperity in sliding contact with a flat and soft surface which deforms perfectly plastic, as shown in Fig. 2.11:

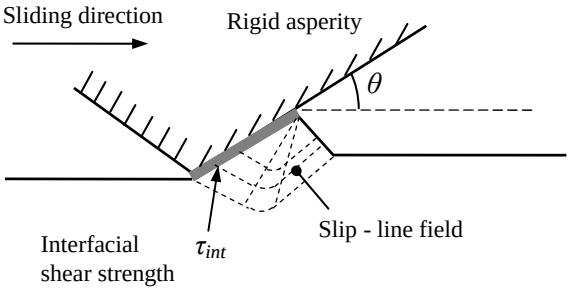

Fig. 2.11 Asperity sliding and associated slip–line field in Challen and Oxley's friction model.

In the model the effect of abrasion and adhesion are combined by introducing two important parameters: the attack angle θ as described previously and the shear strength of the interface τ_{int} which is related to adhesion between two bodies. The interfacial shear strength can be made dimensionless by dividing it by the shear strength of the bulk material, k, to obtain the interfacial shear factor f_{hk}. The f_{hk} thus has a theoretical upper limit of unity. Unfortunately the exact value of f_{hk} depends on the contacting pair and local condition such as temperature and sliding speed. For dry contact this value approaches unity and in boundary lubrication it is 0.4–0.7 [10]. Based on slip–line analysis, a wear mode diagram was constructed, distinguishing three different friction regimes: the ploughing regime, the wedge–formation regime and the cutting regime, determined by f_{hk} and θ:

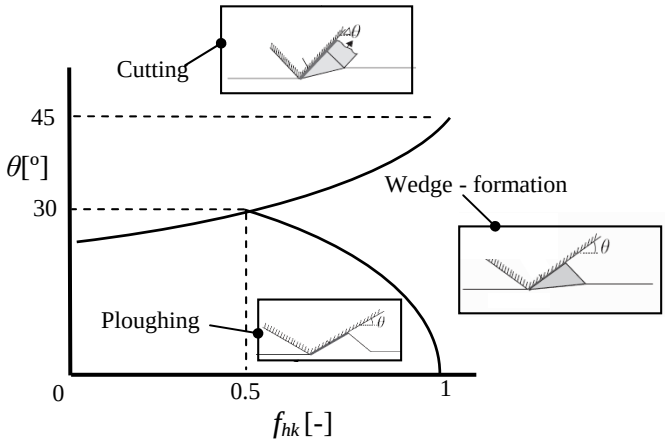

Fig. 2.12 Three different friction regimes illustrated schematically (grey area indicating removed material), reproduced from [38].

It can be seen in Fig. 2.12 that the three friction regimes are determined by θ and f_{hk} together. In the case of lubricated contacts (small f_{hk} values) and smooth surfaces (low attack angles) the asperity is operating in the "ploughing" regime, in which the deformed material is displaced to the ridges on both sides of the asperity, forming a wave–like deformation pattern. In this regime, no material is removed; when the system is not well lubricated (f_{hk} > 0.5) or the surfaces are rough, the displaced material can form a wedge in front of the sliding asperity, and wear can be produced by transfer of the material to the asperity; When the surfaces are very rough and well lubricated the asperity acts like a knife–edge that cuts through the material, producing wear by chipping. The transition lines as shown in Fig. 2.12 can be approximated by [10]:

$$q_{plg \to wf} = \frac{1}{2}\arccos f_{hk} \tag{2.26}$$

$$q_{plg,wf \to cut} = \frac{1}{4}(p - \arccos f_{hk}) \tag{2.27}$$

The coefficient of friction can be calculated according to the analytical model developed by Challen and Oxley with following results [37]:

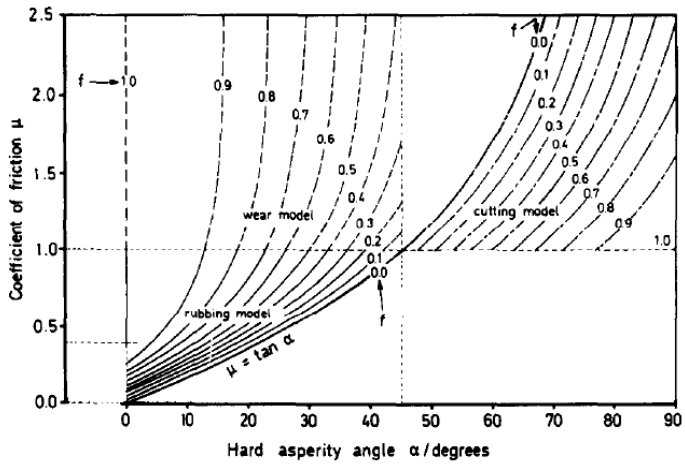

Fig. 2.13 Coefficient of friction as calculated by Challen and Oxley's analytical model [37]. It should be noted that the "wear model" refers to the wedge – formation regime; the "rubbing model" refers to the ploughing regime.

It can be seen that in both the wedge–formation and ploughing regimes, the

coefficient of friction increases with the interfacial shear factor f_{hk}, whereas in cutting regime it decreases with the shear factor. In all the friction modes the coefficient of friction increases with the attack angle. This analytical slip–line model was experimentally validated by Challen, McLean and Oxley [39], and was extended by Hokkirigawa and Kato [40] to abrasion by a spherical slider, indicating that this model can also be applied to friction caused by sliders with an attack angle dependent on the penetration depth (contact interference).

2.2 Thermo–mechanics of aluminium extrusion

The aluminium extrusion process is a thermo–mechanical bulk deformation process. The success of this process depends on the obtainment of both appropriate mechanical and metallurgical features of the billet material. They are also both closely related to the tribological aspects in the process. Since this topic is heavily dependent on the alloy system, in this section the thermo–mechanics of the aluminium extrusion of the 6XXX series alloys are presented.

2.2.1 Metallurgical evolution during the extrusion cycle

The success of an aluminium extrusion process commences well before the extruding of the billets. The billet undergoes an extensive thermal cycle during whole span of the extrusion process, in which the metallurgical and microstructural evolution is crucial in getting everything right. A typical thermal cycle of aluminium extrusion processes of heat treatable alloys is shown in Fig. 2.14:

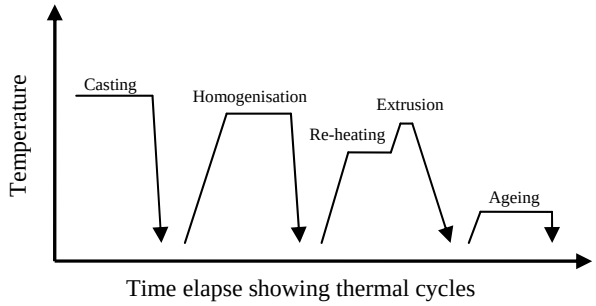

Fig. 2.14 Thermal cycle of a typical extrusion (T6 tempering) [41].

After casting, the first heat treatment applied is homogenisation. This involves heating the “logs” (as they are called in this stage) to a certain temperature usually

below the eutectic point and soaking for some time [1]. During this treatment, the metallurgical changes are: 1) the dendritic cast structure is homogenised therefore the equilibrium in composition is reached; 2) second phase particles are either dissolved or transformed to a desired shape and distribution in the matrix. For the 6XXX series aluminium alloys, they are heated to 565 ºC ~ 595 ºC for several hours in order to transform the plate–shaped β AlFeSi into the rounded α AlFeSi, as well as dissolve the low melting point Mg_2Si and Si particles [42][43]. Latest findings suggest that an additional homogenisation treatment can be performed at preferably 450 ºC to prevent periphery coarse grain (PCG) of the extrudate [44].

Just prior to extrusion the homogenised logs are preheated again to lower its strength therefore decrease the required force from the ram and increase productivity. In order to make sure the achieved microstructure from homogenisation is retained during extrusion, preheating has to be done in such a way that the temperature range from 316 ºC to 417 ºC is traversed rapidly to prevent rapid precipitation of Mg_2Si [1], which causes incipient melting during extrusion, low hardness of the extrudate and deteriorated surface finish. During extrusion, an appropriate extrusion temperature enables complete dissolution of the Mg_2Si and Si particles, eliminating the necessity of a separate solution treatment. Another important feature during the extrusion process is dynamic recovery and/or recrystallisation. This occurs when the stored strain within the grains exceeds some critical value [45]. Dynamic recrystallisation is generally unwanted since it decreases the strength of the extrudate, but a uniform small recrystallised grain size is conducive to fatigue and corrosion resistance [1].

After extrusion the extrudates are subject to different tempering schemes to increase strength. For the 6XXX series alloys the T6 tempering is commonly used, in which a solution treatment (can be combined with the extrusion itself) is performed followed by artificial ageing processes to increase strength by forming extremely small uniformly dispersed second phase particles within the original matrix [46]. Static recrystallisation is this stage is generally undesirable as it results in a reduction of the achieved strength.

2.2.2 Mechanical evolution during the extrusion cycle

2.2.2.1 Constitutive equation of aluminium alloys

In the interests of forming processes the relation between flow stress and various state variables, such as temperature, strain rate and strain, is of great essence. An accurate description of flow stress should take into account both solid mechanics

and microscopic variations, e.g. dislocation dynamics. It is well-known that in the cold to warm temperature range, i.e. when the deformation temperature is below 300 ºC, aluminium alloys show a significant dependency of temperature and strain due to work hardening effect [47][48]. The flow stress can be expressed as follows:

$$s_f(T,e) = s_0\left(1-\frac{T}{T_0}\right)\left(\frac{e}{e_0}\right)^{n_{str}} \tag{2.28}$$

In which the suffix 0 refers to a reference state. When the deformation temperature is above 300 ºC, work hardening effect is only observable at the initial state of deformation, and within steady state it is negligible; strain rate hardening becomes prominent due to high strain rate sensitivity of aluminium [49]. It is most frequently described by the modified Sellers–Tegart law [50]:

$$s_f(T,\dot{e}) = s_m \operatorname{arcsinh}\left[\left(\frac{Z}{A_z}\right)^{\frac{1}{m}}\right] \tag{2.29}$$

In which Z is the Zener–Hollomon parameter, or alternatively called the temperature–compensated strain rate and is written as:

$$Z = \dot{e}\exp\left(\frac{Q}{RT}\right) \tag{2.30}$$

The equation shown above can fit well with the experimental data [51] but it is purely empirical and does not concern the microstructural evolution during the deformation such as dynamic recovery and recrystallisation (strain softening). To incorporate these effects parameters s_m and m can be made dependent on temperature and/or strain [52] [53]:

$$s_m = \frac{1}{c_1 + c_2 \ln e} \tag{2.31}$$

$$m = \frac{1}{n_{strrt}} = \frac{1}{c_3 + c_4 e} \tag{2.32}$$

Where $c_1 \sim c_4$ are experimentally determined constants for a certain alloy. For simplicity the effect of structural evolution during extrusion is not included in this study. The flow stress of AA 6063 used in this study apparently lends itself to the high temperature strain rate hardening regime and is calculated by Eq. 2.29 with the following constants as shown in Table 2-2. A comparison of calculation and experimental data is shown in Fig. 2.15:

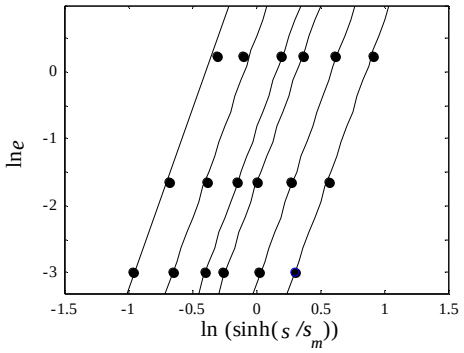

Fig. 2.15 Fit between experimental data and Sellars – Tegart constitutive equation: — Sellars – Tegart calculation; • Evangelista (1991) [51].

Table 2-2 Constitutive parameters for AA 6063 alloy used in this study (parameters based on regressed data from [1]).

Param.	Value	Unit
s_m	25e6	[Pa]
m	5.4	[–]
A_Z	6e9	[s^{-1}]
Q	1.4e5	[J/mol]
R	8.314	[J/(molK)]

Data for other aluminium alloys are given in Appendix G and a discussion on alloy dependency of pickup formation is given in Chapter 9.

2.2.2.2 Stress, strain rate and temperature during extrusion

It is clear from the above-mentioned analysis that the nominal contact pressure p_n is an essential input in any contact and friction model as it determines to what extent two surfaces make contact. In aluminium extrusion, the nominal contact pressure can be obtained by finite element analysis (FEA) of the extrusion process [10], or less precisely by using empirical relations based on the experimental measurement. In this section the empirical equations concerning thermo-mechanics of the extrusion process are presented first; then a method is presented to obtain the actual p_n distribution along the bearing.

First the bulk analysis is presented to obtain the nominal contact pressure inside the bearing channel. The thermo-mechanical aspects during an extrusion are illustrated

in Fig. 2.16:

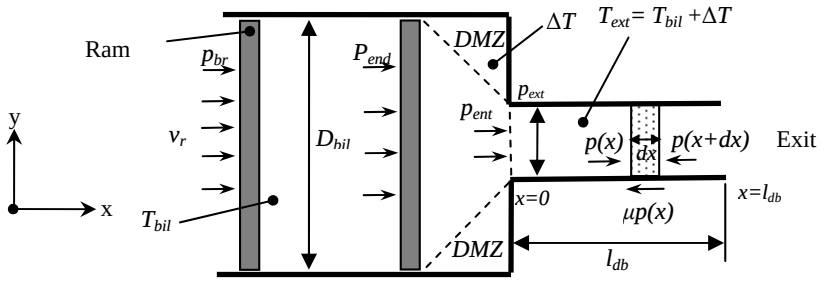

Fig. 2.16 Thermo – mechanical analysis based on experimental data (arrows with an open end indicate direction; arrows with a closed end delimit dimensions).

The most readily measured value is the extrusion force, which yields the pressure value (normal stress on a cross section plane) on the ram by simply dividing the force reading by the cross section area of the billet or the container. During extrusion, plastic deformation of the billet onsets at the "breakthrough point"; at this point ram speed starts to decrease rapidly until the desired steady state speed is reached. Once it is reached, the extrusion force decreases roughly linearly due to reduction of friction in the container. At the end of the stroke the ram is roughly at the location of the DMZ (Dead Metal Zone). The key pressures, P_{br} and P_{end} can be obtained by referring to the extrusion force–ram displacement curve. Since it is the contact stress level inside the bearing (as illustrated in Fig. 1.2 (a)) that is relevant to the current study, the analysis is based on measurements of the stroke end pressure p_{end}.

The bearing entrance pressure p_{ent} can be obtained by the following expression by relating to the measured value of the stroke end pressure [1]:

$$p_{ent} = p_{end} - (1.86 \ln r_{ext} + 0.171) s_f (T_{def}, \dot{\varepsilon}_{eff}) \tag{2.33}$$

In which r_{ext} is the extrusion ratio and $\dot{\varepsilon}_{eff}$ is the effective strain rate during the deformation that can be given by an upper bound analysis:

$$\dot{\varepsilon}_{eff} = \frac{6 v_{ext} D_{bil}^{\ 2}}{r_{ext} \left(D_{bil}^{\ 3} - D_{ext}^{\ 3} \right)} (0.171 + 1.86 \ln r_{ext}) \tan(0.67 + 0.12 \ln r_{ext}) \tag{2.34}$$

The above equations were theoretically obtained by constructing a velocity field in the deformation zone and the constants were fitted using extensive experimental data [1]. The theoretical analysis was merely based on an axisymmetric profile, but it has been shown that it can be applied to rectangular profile extrusion by using the equivalent profile diameter whilst keeping the extrusion ratio constant:

$$D_{ext,eqv} = 2\sqrt{wt/p} \tag{2.35}$$

The deformation pressure and strain rate are plotted as a function of the Zener – Hollomon parameter, shown in Fig. 2.17 (a):

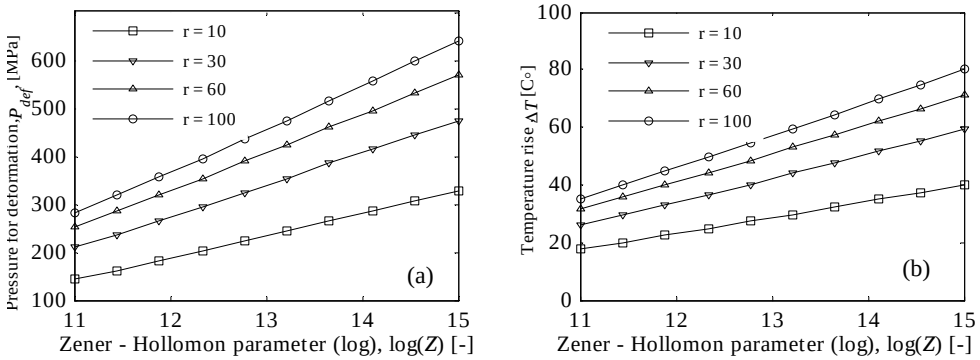

Fig. 2.17 Pressure and temperature rise as calculated by empirical models.

The temperature in the deformation zone T_{def} is the billet temperature plus the temperature rise due to shearing of the billet surface in the container as well as intensive plastic deformation in the deformation zone. The temperature rise predicted by Stuwe [1] has been shown to agree with experimental temperature measurements:

$$\Delta T = \frac{s_{fl}\left(T_{bil} + \Delta T, \dot{\varepsilon}_{eff}\right)\ln r}{\sqrt{3}\,r_{al} C_{al}} \left(1 + 0.25\sqrt{\frac{v_{ext} l_{bil} r_{al} C_{al}}{r K_{al}}}\right) \tag{2.36}$$

This is illustrated in Fig. 2.17 (b) also as a function of the Zener–Hollomon parameter. Therefore, by solving Eq. 2.36 and combing the constitutive equation Eq. 2.29, the temperature in the deformation zone T_{def} can be calculated. However,

Eq. 2.36 assumes adiabatic deformation condition so that no heat is lost to the tooling surrounding; alternatively, T_{def} can be obtained more precisely by actual temperature measurements near the die face by thermometers. Once the temperature in the deformation zone is established, the pressure at the bearing entrance can be calculated through Eq. 2.33.

Without resorting to FEA, the above-mentioned procedure cannot yield the nominal pressure distribution in the bearing channel. A straightforward slab–analysis approach has been implemented by considering the force equilibrium of a thin cross section with a thickness of *dx*. Lof [54] and Tverlid [26] performed FEA of aluminium extrusion and concluded that within the bearing channel the material still undergoes both plastic and elastic deformation. The purpose of conducting this analysis was to obtain the nominal contact pressure distribution as an input in the developed model. It should be emphasised that the straightforward slab analysis only works well for simple profile geometry, for example, a solid rectangular profile.

The normal stress in the extrusion direction σ_{xx} and that in the perpendicular direction σ_{yy} can be equated, yielding the following equilibrium condition (assuming *dx* is sufficiently small):

$$\overline{s_{xx}(x)}A_{\sec} = \left[\overline{s_{xx}(x)} + \frac{d\,\overline{s_{xx}(x)}}{dx}dx\right]A_{\sec} + m\overline{s_{xx}(x)}l_{\sec}dx \tag{2.37}$$

In which *x* is the distance from the bearing entrance, as illustrated in Fig. 2.16. A_{sec} and l_{sec} are the area and perimeter of the cross section of the profile, respectively. Assuming the normal stress does not vary considerably through the cross sectional area according to Tverlid's analysis [26], the average normal stresses can be replaced by the nominal contact pressure. This yields the following integration (see Fig. 2.16):

$$p_n(x) = p_{ent}\exp\left[\frac{l_{\sec}}{A_{\sec}}\int_x^0 m(x)dx\right] \tag{2.38}$$

Where the perimeter/area ratio for certain profiles is:

$$\frac{l_{\text{sec}}}{A_{\text{sec}}} = \begin{cases} \dfrac{4}{D_{ext}} & \text{Circular profile} \\ \dfrac{2(w+t)}{wt} & \text{Rectangular profile} \end{cases} \tag{2.39}$$

It is clear from Eq. 2.38 that the nominal contact pressure inside the bearing channel decreases exponentially with the distance from the bearing entrance if the coefficient of friction does not vary significantly along the bearing length. It can be also concluded that a small profile diameter for circular profile, or a thin thickness for rectangular profile, and complicated-shaped profile increase the pressure gradient in the bearing channel.

2.3 Tribological conditions in aluminium extrusion

Tribology makes its way where contact between surfaces takes place. Applied to aluminium extrusion, two different contacts arise:

- Contact between billet and container wall
- Contact between existing extrudate and die bearing

It is commonly established that at the contact between billet and the container wall, pressure is so high that the contact covers nearly the complete interface and that sliding is impossible — full sticking contact is achieved, according to Schikorra [55]. The surface of aluminium adhering to the container wall is stagnant and recrystallises; the two surfaces are interlocked with the adhering metal penetrating the irregularities of both surfaces, or called “total seizure” in contact mechanics [56]. This is no bad thing as contaminants on the original billet surface are left in the stagnant layer deposited on the container liner. Nevertheless, based on this study of deformation patterns, Schikorra concluded that a certain degree of sliding between the extrudate and the bearing surface is permitted in the bearing channel, as the contact pressure and friction both decrease. This however, creates problems that some sliding products can be collected on the product surface, i.e. Parson et al. [57] concluded that by reducing the effective bearing length to zero, the problem of pickups can be fully eliminated. It is thus obvious that in terms of pickup formation, tribological studies should be focused on the bearing channel. In this section, it will be discussed at length.

2.3.1 Friction phenomena inside the bearing channel

As for all unlubricated contacts, friction between the extrudate and the die bearing surface is high. A very important aspect is the transport of oxygen from the environment to the interface. The formed oxides act as a lubricant in the dry friction condition. It is reported that for absolute dry sliding between steel and aluminium in vacuum, the coefficient of friction approaches 3 causing complete seizure whereas in oxidative condition it decreases to 0.5 or less [36]. A study of the literature suggests that observation of a coefficient of friction as high as 3 during aluminium extrusion is very rare, suggesting that some lubricative effects are introduced by oxidation of the interface. It should be established on this foundation, that both the bearing and the extrudate surfaces are oxidised during extrusion especially considering the high temperature encountered, thus differentiating this study from one orientated at metal – metal seizure in inert environment. The difference made by introduction of oxygen can be best demonstrated by Tverlid [26] in his split die extrusion experiments. However, it is assumed in the current study that all the extrusion processes operate in roughly the same atmospheric condition unless altered intentionally by the extruders; therefore the effect of oxidation is not included in this research.

By far the most commonly used scheme of implementing friction in FEA of aluminium extrusion process is to describe the friction by the Coulomb model with a prescribed coefficient of friction, for example Chanda et al. [58] and Parvizian et al. [59]. Use of a constant coefficient of friction facilitates fast calculation and easy implementation, but is contradictory to other research findings [60][61] that show that the coefficient of friction is a function of local contact conditions, e.g., temperature and sliding speed. Moreover, the prescribed value is often based on empirical knowledge and guesswork, due to lack of techniques capable of actually measuring friction accurately within the bearing channel. Direct measurement is difficult due to geometrical difficulties, so basically friction in the bearing channel is obtained indirectly by deriving it from the extrusion force measurements. However, since the total amount of friction in the bearing channel is much less than that at the container–billet interface and contributes less than is significant to the extrusion force, this measurement technique yields unconvincing results.

An indirect measuring method performed by Thedja [62], Abtahi [63] and Tverlid [26] is to measure the sticking /slipping lengths on the bearing by using split dies. The tooling consists of two die inserts that can be split after the extrusion and a die holder that locks them together during the extrusion, as schematically illustrated in Fig. 2.18:

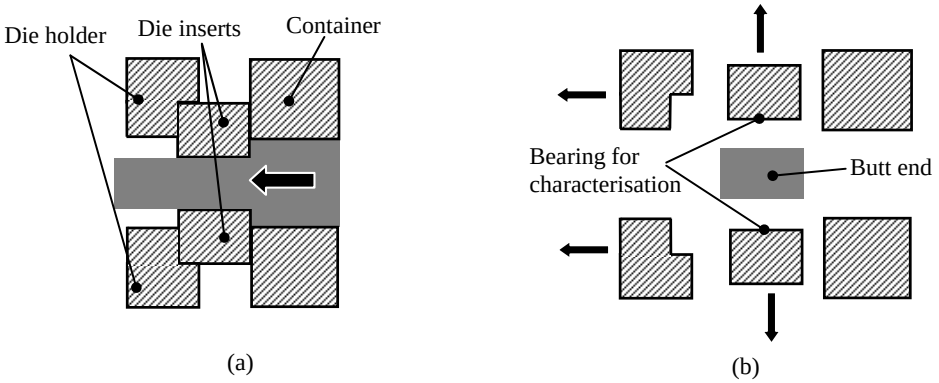

Fig. 2.18 Operation of split die: (a) During extrusion the die inserts are assembled; (b) After extrusion the die holder and container retrieve, the die inserts are split up vertically.

The split die reveals morphological information of the as-extruded bearing without having to use hydroxide sodium or other caustic to dissolve the “butt end” after extrusion agents that must be performed otherwise.

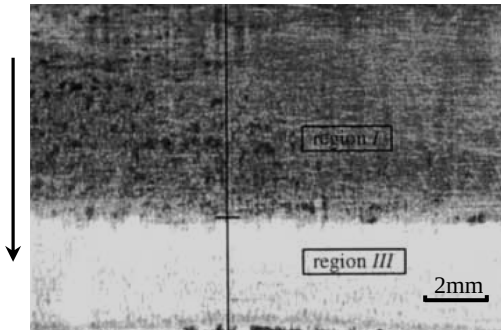

Fig. 2.19 Sticking / slipping zones on a bearing in Abtahi’s split die experiment [63]. Arrow indicates the extrusion direction.

It was observed that a clear separation on the bearing surface appeared after extrusion, as shown in Fig. 2.19. It can be seen that the exit shiny part of the bearing is covered by an adhesive layer made up from the extrudate material; this is called the “slipping zone” in which the surface of the extrudate can slide; whereas there is no adhesive layer on the entrance dark part of the bearing, and it is called the “sticking region” in which the surface of the extrudate adheres to the bearing surface which can be seen as an extension of the billet–container contact. This may seem contradictory as the slipping zone is actually covered by aluminium deposits. It can be explained by the fact that when the extrusion is ceased just prior to die

split-up, strong adhesion between the aluminium sticking layer in the sticking zone forms a strong bond with the extrudate material, and as the die inserts are split the junctions are torn off where it is weakest, the Al–Fe interface, leaving only very limited aluminium primarily residing in the valleys. In the slipping zone, the surface is allowed to slide therefore only the asperities on the bearing are covered by aluminium. When die inserts are split up, the junction will break at the partially oxidised Al–Al interface, leaving an adhesive layer [26]. The sticking layer can, however, be observed on the container liner because the process is not stopped until the ram reaches the end of the container, therefore no re-bonding between the sticking layer and the extrudate can occur. The lengths of two regions are closely determined by the friction in the bearing channel. Sticking is considered to occur when the nominal friction stress exceeds the shear strength of the extrudate so that the surface will stick to the bearing [26]. The nominal contact pressure at the slip point can hence be written as:

$$p_{stk \to slp} = \frac{k}{m} \tag{2.40}$$

As the nominal contact pressure decreases from the bearing entrance towards the exit, the nominal friction stress also decreases until it reaches the slip point where it is not greater than the bulk shear strength, as shown in Fig. 2.20:

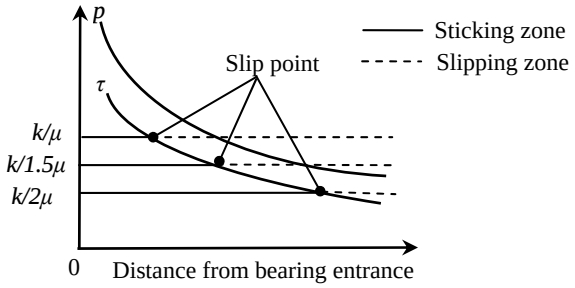

Fig. 2.20 Sticking / slipping length and friction.

It can be seen that as the coefficient of friction increases, the length of the sticking zone is increased, which decreases the slipping length instead. Therefore, by measuring the lengths of two zones one can obtain the friction inside the bearing channel. Results from previous split die extrusion experiments show good coherency and they have all yielded the same conclusions [26][63]:

- Sticking and slipping lengths are mutually supplementary; an intermediate zone has only a very limited length or sometimes is absent.
- The ratio between the sticking/slipping lengths increases with the nominal contact pressure inside the bearing channel, which can result from a large bearing choke angle, a long bearing length or a large reduction ratio.
- The ratio between the sticking/slipping lengths decreases with a high exit temperature and fast exit speed.
- When using a different die bearing length, the change of exact values of sticking/slipping lengths is unclear.

An empirical expression of the slipping length proposed by Abtahi is written as:

$$l_{slp} = \left[(c_1 v_{ext} + c_2) \exp\left(\frac{a_{db}}{c_3 v_{ext} + c_4}\right) + c_5 v + c_6 \right] t \tag{2.41}$$

The above expression was fitted by results from their split die experiments and shows the trends mentioned above. It is clear that the slipping length decreases when friction inside the bearing channel is raised.

The mechanism for sticking in the sticking region is studied by Ma [64]. Three possible mechanisms result in the sticking zone, and they can be distinguished by the velocity and strain rate profile near the interface: a) sticking involves localisation of shear strain in the vicinity of the bearing surface, similar to the secondary deformation zone usually observed in machining [65]; b) without the formation of such a localised shear layer, but a continuous velocity profile varies from zero at the interface to a maximum velocity at the extrudate centre axis, resulting in a much smaller and more constant strain rate over the cross section of the extrudate; c) this mechanism differs from the second one by allowing a small velocity difference at location in the vicinity of the extrudate–die bearing interface, which acts as an effective interface. The velocity profiles of these three possible mechanisms are shown below:

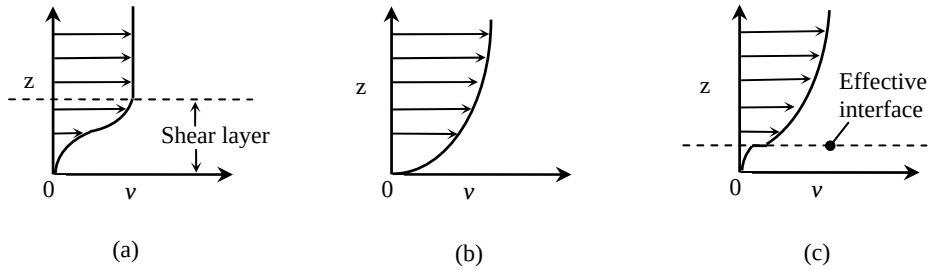

Fig. 2.21 Illustration of the velocity profile of extrudate in the vicinity of the extrudate–die interface ("z" represents the distance to the interface).

By calculating the associate temperature and strain rate fields by FEA analysis, it has been shown that shear localisation such as shown in Fig. 2.21 (a) is not possible to occur in the extrusion of aluminium due to the relative large strain rate sensitivity of aluminium alloys compared to other metals like steel [64]. The effect of thermal softening is overwhelmed by the tremendous strain rate hardening effect, thus shear localisation cannot develop within this particularly hardened layer. Fig. 2.21 (b) and (c) differ in the failure modes of the interface. A continuous velocity profile indicates that no actual interface is present, thus velocity difference between the centre and the perimeter of the extrudate is accommodated by internal shearing of the aluminium extrudate across a much larger cross sectional area than in Fig. 2.21 (a). In the case of Fig. 2.21 (c) a small velocity discontinuity is allowed at the aluminium–aluminium effective interface by surface detachment due to void coalescence at the subsurface level — large friction cannot be accommodated by retaining surface integrity; detachment of the actual extrudate surface produces a layer of sticking aluminium in which probably only a very small strain rate exists. Distinguishing between mechanisms Fig. 2.21(b) and (c) seems nontrivial, but the two mechanisms share one common characteristic: the shear strain at the interface is not confined in a localised layer. In this case of total seizure, material transfer is probably along both directions (from the sticking layer to the extrudate and vice versa) and is not confined within the contact spots but at a larger scale at the subsurface level, and the thickness of the sticking layer remains roughly constant during the extrusion process.

In the slipping zone conventional sliding friction applies and the strain rate across the cross section is much smaller than in the sticking zone [26]. Material transfer is confined within the contact spots and is primarily unidirectional — from the extrudate to the bearing since the aluminium deposited on the bearing is hardened by lower temperature. The coefficient of friction during aluminium extrusion in the slipping zone was found to be a function of the sliding speed (exit speed), as

experimentally fitted by Tverlid [26]:

$$m = -1.47v + 1.06v^2 + 8.45 * 10^{-3} a_{db} + 0.65 \quad (2.42)$$

The expression predicts a decrease of the coefficient of friction with the sliding speed, followed by a slight increase at around 0.8 m/s. This expression was obtained when assuming friction is equal to shear strength in the sticking zone, but it nevertheless suggests that friction is dependent on the contact conditions, e.g. temperature and sliding speed. An explanation from Tverlid is that as temperature and sliding speed get higher, local melting of asperities is due to flash temperature that lowers the shear strength of the interface. However, as will be demonstrated in Chapter 3, in aluminium extrusion the flash temperature is negligible to the bulk temperature. A possible explanation is that under the combined effect of normal and tangential loading, the interfacial adhesive bonding rather than the aluminium itself behaves as a viscous fluid to allow sliding. The input shear stress (apparent friction) required to form this viscous bonding thus decreases at higher temperature and sliding speed.

2.3.2 Pickup formation

There is yet no sound physical model capable of predicting the formation of pickups, due to lack of a clear understanding of the onset of this daunting problem. Research has been orientated to empirically studying the effect of several factors on pickup formation so that guidelines can be provided to extruders on how the process can be tailored to overcome this problem. Pickup formation could be related to metallurgical aspects during the extrusion. A common knowledge regarding this [6][7][66] involves the peritectic reaction of Mg_2Si and β–AlFeSi particles that produces liquid at grain boundaries at 576 ºC. Therefore, remedies include increasing iron content which is conducive to β → α AlFeSi transformation during homogenisation and decreasing Mg content to reduce the amount of unsolved Mg_2Si particles during extrusion, of course at the expense of jeopardising mechanical properties of the end products.

On top of this metallurgical mechanism, researchers have suggested that a metallurgical process involving transfer of material at the bearing interface is responsible for formation of pickups [1][2]. Only material transfer in the slipping zone is relevant since in the sticking zone total seizure takes place. A direct proof of this material transfer is the adhesive deposits observed in the slipping zone on the die bearing, containing the extrudate material and on some occasions, excessive

oxygen [62]. The extrudate material adheres to the bearing surface due to large adhesion between the contacting surfaces under extrusion operating conditions to form the deposits, which will occasionally detach under certain conditions. It is this process that has been considered to contribute to the formation of pickups on the product surface. In reality, the mechanical and metallurgical mechanisms probably operate conjunctively to contribute to pickup formation, e.g., intergranular melting weakens the strength of the surface material and encourages material transfer to the bearing. However, in the current study the effect of metallurgical events, such as study of chemical composition of the alloy, is not included.

Since pickup formation is closely related to the tribo–mechanical behaviour of the interface, it is essential to study how process parameters can be optimised in this regard. Sheppard [1] suggested by collecting experimental results that a "safe window" for pickup formation can be constructed, based on the Zener–Hollomon parameter. The locus dividing the experimental results exhibiting an acceptable surface and those showing excessive pickups for AA 6063 can be determined by the inequality, shown below:

$$\ln Z \le 1.236 \times 10^{6} T^{-1.7} \tag{2.43}$$

In which the coefficient was fitted according to a large amount of experimental data for AA 6063 of arbitrary profile shape and therefore might be different for other aluminium alloys. Relating Eq. 2.43 and assuming that the average strain rate can be expressed as $\dot{\varepsilon} = v/c$, a process window for generating the acceptable amount of pickups can be defined by the following inequality:

$$cv \le \exp\left(1.236 \times 10^{6} T^{-1.7} - \frac{1.4 \times 10^{5}}{8.314T}\right) \tag{2.44}$$

The effect can be shown in Fig. 2.22 (a):

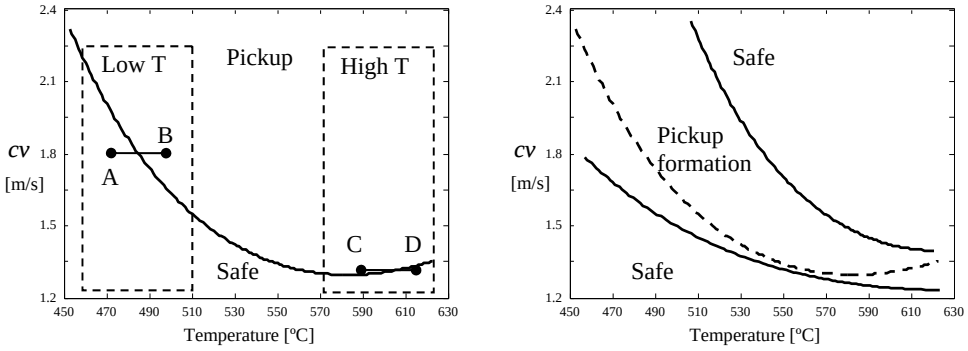

Fig. 2.22 Prediction of excessive pickup by the Zener–Hollomon parameter.

It can be seen in the general operating range of extrusion, the threshold exit speed for pickup formation decreases significantly with temperature, whereas at high temperature this is replaced by an increase of the speed. The result is somewhat surprising because it suggests that pickup formation seems to be reduced when the extrusion temperature is high enough. Another notable study in which several factors including billet temperature and exit speed were studied extensively to examine their effects on pickup formation [57], has revealed a clearer relationship in between the parameters as shown in Fig. 2.23:

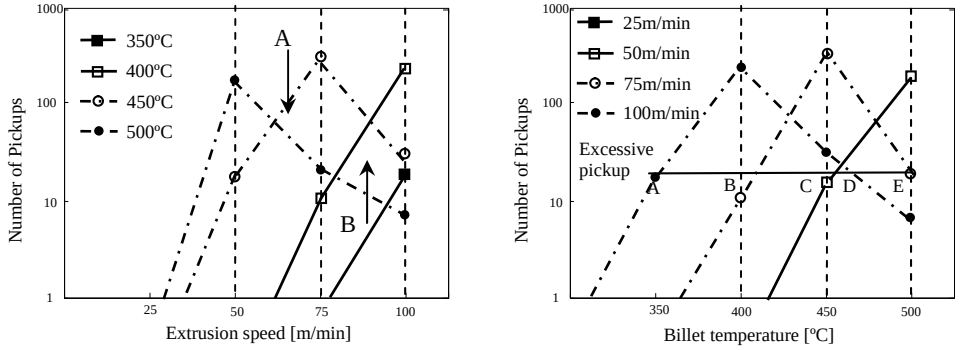

Fig. 2.23 Pickup formation as a function of billet temperature and exit speed [57]: (a) Directly taken from the publication; (b) Reconstructed by the author.

Interpretation of the findings from Sheppard and Parson suggests some coherency in results. In the low temperature range as marked in Fig. 2.22 (a), when

temperature is increased, for example from point A to point B, pickup formation becomes worse as the safe zone is exceeded; however in the high temperature range, for example from point C to point D, an increase of temperature can enter the safe zone again, thus is beneficial for reducing pickups. The same information can be extracted from Fig. 2.23 (a) that for extrusions in high temperature range (450ºC and 500ºC billet temperature), a decrease of pickup formation is observed indicated by arrow A, and in the lower temperature range formation of pickups is encouraged with an increase in temperature. In Fig. 2.23 (b) results from (a) are reproduced to show the effect of temperature. Assuming "excessive pickup surface" is one on which there are more than 200 pickups, then a horizontal line can be drawn to intercept the curves at points A ~ E, giving the threshold exit speed values for excessive pickups. It can be seen at the lower temperature range from A ~ C, the threshold speed increases with temperature; whereas at high temperature from D to E, the opposite is true. This observation can clearly be confirmed in the curve shown in Fig. 2.22 (a).

It can be concluded from the above analysis that pickup formation is encouraged as temperature increases to some critical value, after which further increase in temperature will actually hinder pickup formation. Another observation in Parson's findings is that the shape of the plots in Fig. 2.23 (a) and (b) are identical, suggesting that temperature and speed should have similar effects on pickup formation. Therefore the same conclusion can be drawn that increase in speed is favoured by pickup formation until some critical value is reached. However, Sheppard suggests once the pickup formation zone is entered by increasing speed, further increase will only worsen it, indicated by a single line instead of an actual window. This can be modified as shown in Fig. 2.22 (b) which can best describe the experimental results — a zone exists, bounded by temperature and exit speed, in combination probably with other process parameters, in which the problem of excessive pickups is prone to occur.

It was also concluded from the study, that apart from the process parameters such as temperature and speed, geometry of the die bearing, i.e., the bearing length and bearing angle, was also observed to significantly influence pickup formation, which can be summarised as:

- A fully choked bearing (α_{db} = +1.4°) eliminated pickup formation, but scoring of the extrudate surface was much more severe.
- A fully relieved bearing (α_{db} = -1.4°) which was effectively a zero – bearing die fully eliminated pickup formation.

- Bearings containing a choke and relief parts produced pickups, and the number of pickups increased as the magnitude of the choke (relief) angle increased to 0.7°.

Therefore, the pickup formation is influenced by a number of factors ranging from process parameters to tooling geometry. A physical model incorporating all these effects is what this thesis aims at.

2.4 Summary

In this chapter an overview has been given on the fundamentals of tribology and aluminium extrusion and how tribological aspects of the aluminium extrusion can be altered by changing process parameters.

Section 2.1 presents the contact and friction models available for modelling friction; particular attention has been given to modelling the dry and adhesive friction found in aluminium extrusion.

In order to correctly model the behaviour of aluminium under tribo-mechanical conditions, thermo–mechanics of the extrusion process are discussed in Section 2.2 at length. It serves as a theoretical basis for obtaining boundary values for subsequent modelling.

In Section 2.3 the friction and contact conditions specific for aluminium extrusion are discussed. By surveying the literature, the exact tribological aspects in the extrusion process are understood. The presence of two distinct zones, the sticking and slipping zones found on the die bearing surface, has been given great focus. It is then followed by analysis on how all these parameters including temperature, speed and tooling geometry can work together to obtain a defect – free surface. Finally, it is established that a model incorporating all these factors is imperative for the study of this matter.

Chapter 3
Modelling contact and friction in aluminium extrusion processes

3.1 Contact coalescence between rough surfaces

The use of contact models based on summit analysis is only fundamentally correct based on an important assumption as adopted by Greenwood and Williamson [13], Chang [14] and a lot of other researchers: that a contact is formed when a summit meets the opposing surface, and that this contact then grows independently of all other micro contacts. Therefore, as the number of contacting summits increases as two surfaces approach, so does the number of contacts. This, however, contradicts the obvious fact: contacts do not simply grow, they also coalesce to form contact patches.

A straightforward approach demonstrates the difference with or without considering this coalescence process. Consider a Gaussian rough surface in contact with a flat plastically deformed surface. The genuine contact area (with contact coalesced) at a given dimensionless surface separation $\xi=h/\sigma$ is according to section 2.1.1.3 and is simply determined by truncation of the microgeometry of the rough surface (suffix *cl* refers to coalescence):

$$A_{cl} = A_n \int_h^\infty f(z)dz = \frac{1}{2}\operatorname{erfc}\left(\frac{x}{\sqrt{2}}\right)A_n \tag{3.1}$$

The contact area with the assumption that summits only grow but do not merge (summit-based model) can be obtained by simply summing up the contact area borne by each of the contacting summits:

$$A_{non-cl} = 2p\,h\,\bar{b}A_n \int_h^\infty (s - x\,s\,)f(s)ds \tag{3.2}$$

Where $\bar{b}$ is the mean summit tip radius of a surface and *Φ(s)* is the summit height density function. The summit height density function is different from that of the surface height and takes a rather complicated form [9]. For simplicity it can be assumed that it is also Gaussian, and the product $h\bar{b}s$ is taken as 0.05, from which the degree of contact calculated by both methods can be shown below:

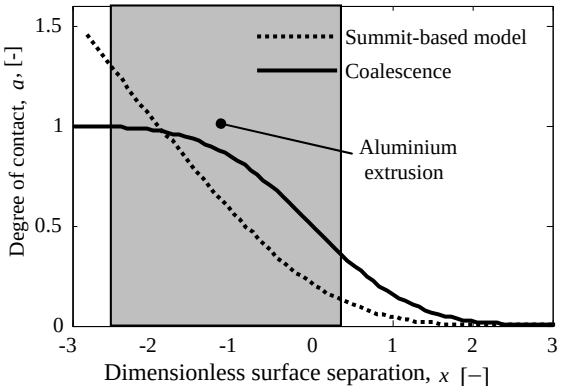

Fig. 3.1 Degree of contact with and without considering contact coaelescence.

It can be clearly seen that the two curves have different characteristics. At small - medium load levels, the summit-based model predicts a lower contact area than the true value (calculated according to surface truncation Eq. 3.1) since at this load level contact is not only shared by the summits, but also by other parts of the surface. However, as the load keeps increasing, the true contact area gradually levels off to the apparent contact area, as coalescence of the contacts rather than individual growth of summits becomes the dominant approaching process, whilst prediction from the summit-based model illustrates a steady increase to even beyond unity, as this model assumes that the contact area of each summit can grow independently of its neighbouring area, even “interfering” with the growth of other summits. In terms of the load range encountered in the aluminium extrusion process (marked as grey area in Fig. 3.1), this is clearly a major deviation from reality which is crucial in the analysis of this thesis.

The introduction of a contact model based on contact patches instead of summits tackles this problem, as proposed by Nayak [15]. A contact patch is a cluster of surface height points (measured or numerically generated) that are in contact with the opposing surface. Specifically, the number of closed contours on a rough surface at a given surface separation was studied by Nayak. However, within a

contact patch "holes" may be present, and the number of closed contours is only related to the difference between number of holes and number of contact patches. Nayak estimated the upper and lower bound of the number of holes, but an exact number could not be obtained. Greenwood [67] provided a solution assuming that when the dimensionless separation is non-negative, the number of minima below ξ within contact patches (holes) is equal to the number of summits above $-\xi$ which can be calculated using Nayak's statistical model. In their work, a bandwidth parameter ψ was defined by the three moments of the surface PSD as introduced in Chapter 2. This parameter is considered a controlling parameter in determining the number of contact patches:

$$y = \frac{m_0 m_4}{{m_2}^2} = \left(\frac{s_z s_k}{{s_s}^2} \right)^2 \tag{3.3}$$

If a surface can be decomposed to a set of random signals with a mixture of frequencies, this surface can be characterised analogously to random signals. A broad spectrum, as indicated by a large bandwidth parameter, is a surface that has waves with a large range of wavelengths; a narrow spectrum has waves of approximately equal wavelength. The number of contact patches can then be obtained using the following expression:

$$\frac{r_{cp}(x) - r_s(-x)}{r_s(x)} = c \frac{y x \exp\left(-0.5x^2\right)}{F(x,y)} \tag{3.4}$$

Where ρ indicates the density of surface features and $F(\xi,\psi)$ is the cumulative density function for summits, as detailed in Appendix B. This relation suggests that the ratio between number of contact patches and summits in contact is merely a function of the dimensionless surface separation and the bandwidth parameter. Reproduction of Greenwood and Nayak's theory can be shown in Fig. 3.2, demonstrating the ratio between numbers of contact patches and contacting summits of surfaces with a range of ψ values:

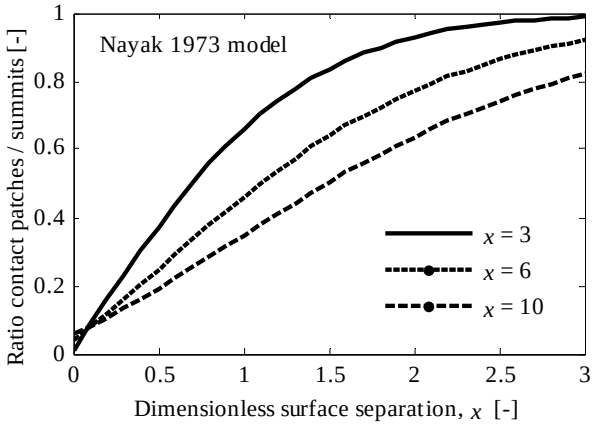

Fig. 3.2 Ratio between the number of contact patches and contacting summits (Nayak's statistical model as modified by Greenwood).

The statistical model of Nayak clearly illustrates that any plastic contact model applied to the extrusion process must take into account, or allow for, the coalescence of contact, as the number of contact patches deviates from that of the contacting summits substantially as normal load is increased. This is extremely important at contact situations in aluminium extrusion as the normal load is quite large over a majority of the contact area. However, Nayak's statistical model does have some limitations: 1) It is only correct when the load is not too large (for example when separation is negative); 2) It does not give any geometrical information of the contact patches, e.g. their shape, which is crucial in modelling friction. Therefore, a deterministic approach of characterising contact patches on engineering surfaces is presented on this basis [68], in the next section.

3.2 A deterministic approach for contact coalescence

To facilitate systematic studies, a series of nominally flat surfaces with a Gaussian surface height distribution has been generated numerically following procedures described by [69]. Their properties are listed in Table 3-1:

Table 3-1Numerically generated surfaces used in this study (ACL = Auto – Correlation Length).

Surface	Rq [μm]	Anisotropy	ψ	ACL_x/ACL_y	Varied parameter
1	1	Isotropic	6.0	1	Reference surface
2	2	Isotropic	6.0	1	Roughness
3	0.5	Isotropic	6.0	1	Roughness
4	1	Transversal[1]	7.0	0.1	Anisotropy
5	1	Longitudinal	7.0	10	Anisotropy
6	1	Isotropic	3.0	1	Bandwidth parameter
7	1	Isotropic	10.0	1	Bandwidth parameter

3.2.1 Identification of contact patches

For either experimentally measured or numerically generated surfaces, the surface height matrix indicates the height of the surface at a certain location in the sampled area. As mentioned above, the contact between two rough surfaces can be reduced to contact between a rough surface and a flat one. By truncating the rough surface at a given surface separation, the contacting part of the surface can be located.

To capture the nature of contact patches, they first have to be identified and located in a surface height matrix. The number of closely packed surface points instead of contacting summits is taken into account. Truncation of the rough surface at the separation level gives a binary matrix where points within or outside contact patches are distinguished. Each contact patch is identified by a cluster of points higher than the input surface separation (called an "object") connected together at least with an edge. This is called the "4–connectivity" in image processing theory, as schematically illustrated in Fig. 3.3:

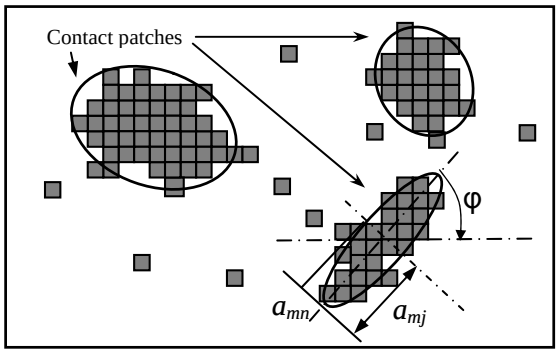

Fig. 3.3 Identification of contact patches.

[1] Transveral anisotropy means surface microgeometry is aligned parallel to the sliding direction. Longitudinal anisotropy means perpendicular to the sliding direction.

Therefore, the coalescence of contact is taken into account by treating them as a single contact patch. Again, the ratio between contact patches and contacting summits can be plotted as a function of the dimensionless surface separation according to this deterministic approach, as shown in Fig. 3.4:

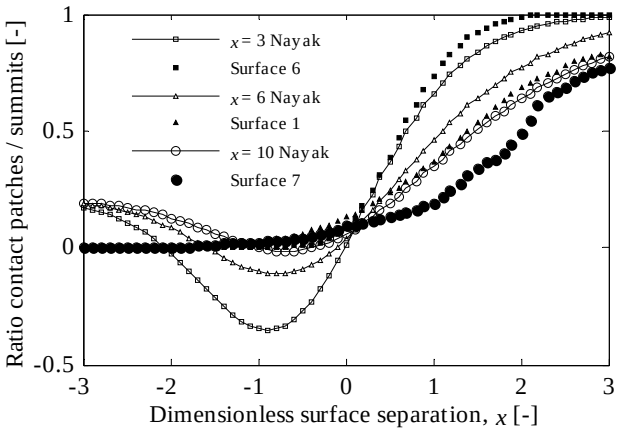

Fig. 3.4 Number of contact patches and summits as determined by Nayak's statistical model and the deterministic approach.

Notice that the Nayak model predicts untrue values when the separation is negative and the deterministic approach suggests a steady decrease of the ratio. As can be seen, both the statistical model and the deterministic approach demonstrate that the number of contact patches is substantially less than that of the contacting summits when the surface separation decreases, i.e. with large load. Therefore, it is essential to model friction and contact based on the true contact spots rather than individual summits in aluminium extrusion. The results from both methods show good agreement when the bandwidth parameter is small; when it is large, the surface roughness spectrum covers a big wavelength range and the agreement is less obvious. This can be explained by the fact that the sampling frequency limits the measurement in the sense that the high frequency surface details that are present in the surfaces with large ψ are not measured. Both models indicate that the number of contact patches is a function of the bandwidth parameter and it generally decreases with it.

3.2.2 Characterisation of contact patches

After the contact patches had been identified, they were modelled as representative elliptical paraboloids. This choice was made to better incorporate surface

anisotropy and obtain a more precise description of the surface topography than other geometry such as conic and spherical shaped asperity [33]. Using the deterministic approach one can obtain several geometrical parameters for this contact patch: the major radius length a_{mj}, the minor radius length $a_{mn,}$ the orientation angle φ (φ = 0 as aligned parallel to sliding direction) and the total volume of this contact patch V_{cp}. The base ellipse is characterised by mapping its centroid to the centroid of the cluster of contacting points, its major and minor radius lengths and the orientation angle of this ellipse being such that the ellipse has the same second central moments as the region, as illustrated in Fig. 3.5:

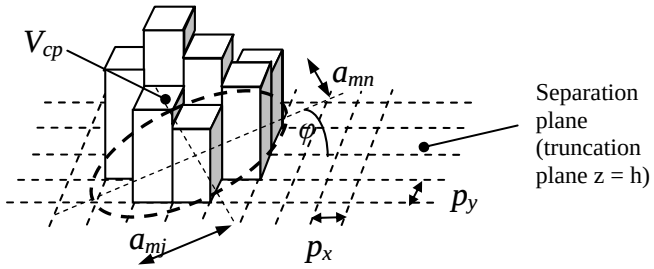

Fig. 3.5 From measurements to modelling.

The total volume of this contact patch is determined by summing up the pixel height within this contact patch (suffix *cp* refers to contact patch hereafter):

$$V_{cp} = p_x p_y \sum_{i=1}^{n} (z - h) \tag{3.5}$$

Now the geometry of the representative elliptical paraboloid can be fully defined:

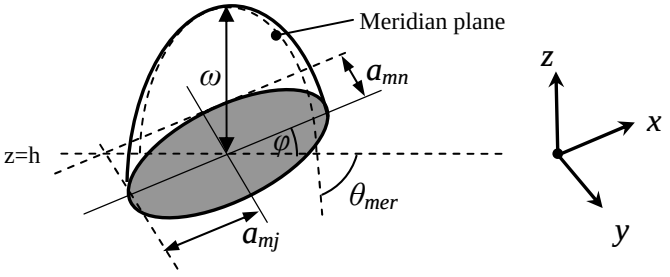

Fig. 3.6 A representative elliptical paraboloid.

The surface of the representative elliptical paraboloid can be described mathematically by:

$$z = h_{pr}\left[1 - \frac{x^2}{\left(l_{ph}h_{pr}\right)^2} - \frac{y^2}{\left(l_{ph}\,l\,h_{pr}\right)^2}\right] \tag{3.6}$$

The height number h_{pr} is a reference number that can be chosen arbitrarily, merely to define the shape of the elliptical paraboloid. The ellipticity ratio λ is the ratio between the major and minor radius lengths; the periphery factor λ_{ph} determines how "wide" a paraboloid expands at the reference height. The ellipticity ratio is an invariant for an elliptical paraboloid with a fixed geometry. The contact area at a given interference ω is also an ellipse with a major contact radius a_{mj} and a_{mn} which can be obtained using the following expressions:

$$a_{mj} = l_{ph}\sqrt{wh_{pr}} \tag{3.7}$$

$$a_{mn} = l\,l_{ph}\sqrt{wh_{pr}} \tag{3.8}$$

In fully plastic sliding condition, the load is only carried by the front part of the contact patch [18], thus the contact area can be written as:

$$A_{pl,sl} = \frac{pa_{mj}a_{mn}}{2} = \frac{p\,l\,l_{ph}{}^2 h_{pr} w}{2} \tag{3.9}$$

It is shown that if the geometry of a contact patch is fully defined, the contact area of this elliptical paraboloidal contact patch increases linearly with the indentation ω. This indentation of the representative contact patch is determined such that the volume and contact area of the representative paraboloid are the same as the contact patch [33], since the representative elliptical paraboloid should be one that has the same contact area and volume in order for the load and energy balance to be maintained. This yields:

$$w = \frac{2V_{epp}}{A_{epp}} = \frac{2V_{cp}}{A_{cp}} = \frac{2p_x p_y \sum_{i=1}^{n}(z-h)}{pa_{mj}a_{mn}} \tag{3.10}$$

Where suffix *epp* indicates the elliptical paraboloid. The degree of penetration D_p is expressed as the ratio between contact radius a and the indentation depth ω, and can be related to the attack angle on the meridian plane θ_{mer}:

$$D_p = \frac{w}{a_{epp}} = \frac{\tan(q_{mer})}{2} \tag{3.11}$$

In which the contact radius a can be obtained from geometry

$$a_{epp} = \frac{a_{mj} a_{mn}}{\sqrt{a_{mn}^2 \cos^2 j + a_{mj}^2 \sin^2 j}} \tag{3.12}$$

However, in order to apply the Challen & Oxley friction model which was developed for two-dimensional wedges, a three dimension shape factor χ is introduced to relate the degree of penetration with the effective attack angle θ_{eff} [40]:

$$\frac{w}{a_{epp}} = \frac{c \tan(q_{eff})}{2}; \quad q_{eff} = \arctan\left(\frac{2w\sqrt{a_{mn}^2 \cos^2 j + a_{mj}^2 \sin^2 j}}{c a_{mj} a_{mn}}\right) \tag{3.13}$$

The shape factor is obviously a function of the ellipticity ratio λ and takes the value of 0.8 for a circular contact area with $\lambda = 1$ [40] and unity for two-dimensional geometry $\lambda \rightarrow 0$. It can be assumed that unless the ellipticity ratio is very close to zero (extreme anisotropy of the surface roughness), the shape factor should be close to 0.8. This value has been used in this study. For a contact patch with a fixed shape, the effective attack angle can hence be plotted as a function of the indentation depth and the orientation angle:

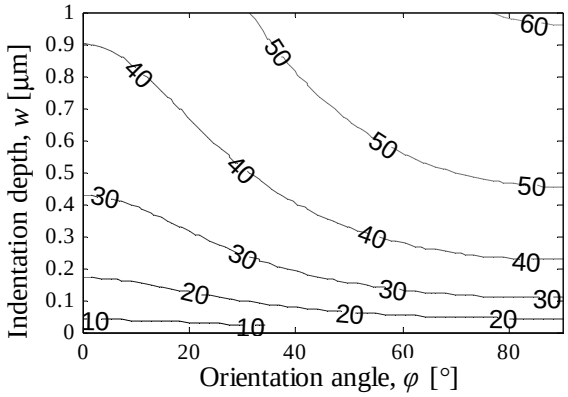

Fig. 3.7 Effective attack angle as a function of the indentation depth and the orientation angle. Calculations using shape geometrical parameters: h_{pr} = 2 μm; λ_{ph} = 2; λ = 0.5.

It is shown in Fig. 3.7 that the effective attack angle increases as the indentation depth increases. It also increases as the minor axis of the ellipse is aligned parallel to the sliding direction, and this effect is more pronounced when the ellipticity ratio is decreased. Therefore, the average attack angle of a surface ground perpendicularly to the sliding direction is larger than a surface ground parallel to the sliding direction.

3.2.3 Results and discussion

Since the number of the contact patches depends on the surface separation and thus the nominal contact pressure, the geometry of the contact patches is also load-dependent, resulting in load-dependent friction. The average effective attack angle of a rough surface can be obtained by a weighted average value as:

$$\bar{q}_{eff} = \frac{\sum_{i=1}^{n} q_{i,cp,} A_{i,cp}}{a A_n} \tag{3.14}$$

This weighted average attack angle takes the contribution from each contact patch, and is thus more meaningful than the arithmetic average value, since it is closely related to the friction contribution from each individual contact patch. A comparison of the numerically generated surfaces is shown in Fig. 3.8:

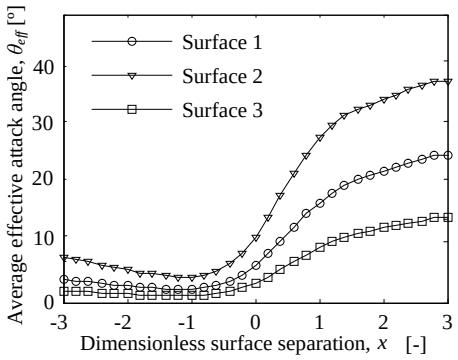

(a)

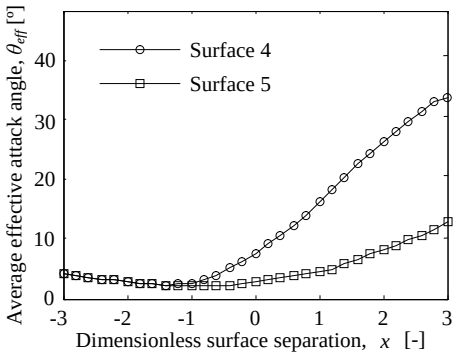

(b)

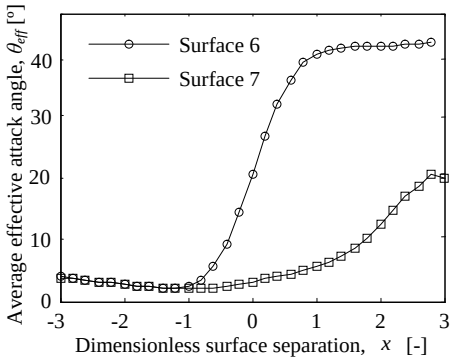

(c)

Surf.	Rq [μm]	ψ	ACL_x/ACL_y
1	1	6.0	1
2	2	6.0	1
3	0.5	6.0	1
4	1	7.0	0.1
5	1	7.0	10
6	1	3.0	1
7	1	10.0	1

(d)

Fig. 3.8 The average effective attack angle of numerically generated surfaces: (a) effect of surface roughness; (b) effect of surface anisotropy; (c) effect of the bandwidth parameter ψ; (d) revisit of the parameters of numerically generated surfaces.

It can be clearly seen from Fig. 3.8 that the average attack angle is influenced by surface topography and surface separation (thus nominal contact pressure). It can be seen that as the separation decreases, the attack angle is reduced due to formation of blunt contact patches because of contact coalescence. At very small surface separation, the contact area of contact patches is limited by the measurement area, thus the marginal increase of attack angle at very low attack angle is considered to be a numerical effect.

As can also be seen the attack angle increases as the surface roughness is increased, or as the surface anisotropy is aligned transversally, or as the bandwidth parameter is reduced, all of which lead to sharper contact patches. It should be noted that at

small separation, the effect of surface topography is greatly diminished, as the coalescence process starts to produce contact patches of similar blunt shape.

3.3 Fully plastic contact model

In this section a fully plastic contact model including effect of contact coalescence and material's constitutive behaviour is presented, based on the contact patch approach mentioned above.

3.3.1 Model assumptions

There are several assumptions made in the contact model developed for aluminium extrusion:

- Indentation of the soft aluminium by the rough bearing: it has been established that as the billet passes through the deformation zone and sticking region, a nascent aluminium surface is formed. This surface is smooth due to the shearing nature [1][26][63]. As the extrudate enters the slipping region, sliding contact starts to deteriorate this smooth interface and surface defects are formed. Therefore, contact condition is one in which a hard rough surface (bearing) indents a soft and smooth surface (aluminium). Therefore, the roughness of the bearing is of relevance.

- Fully plastic deformation: due to the high pressure involved and large hardness difference between the bearing and the extrudate, the contact model assumes fully plastic deformation at all contact spots. This means that the deformation of the bearing asperities is negligible and the contact area only covers the front half of the contact asperity in sliding direction. The fully plastic condition can be evaluated by calculating the associated plasticity index Ψ of the surface, according to Eq. 2.11 [11]. It has been found that the plasticity index for aluminium–bearing contact is much higher than 2, due to small hardness / elasticity ratio of aluminium. Therefore assuming fully plastic condition suffices.

- Flash temperature neglected: It has been assumed that the flash temperature due to heat dissipation of local deformation within contact spots is negligible compared to the temperature of the bulk material, due to the high bulk

temperature encountered in aluminium extrusion and the large thermal conductivity of aluminium. Following Bos's model [70], the flash temperature due to plastic deformation of the aluminium within the contact spot can be estimated. It has been found that the flash temperature is smaller than 1°C for practical conditions in aluminium extrusion. The very small flash temperature can be attributed to: 1) Low hardness of the aluminium (thus low friction force); 2) Large thermal diffusivity of aluminium. This validates the assumption that the temperature in the contact spots is equal to the bulk aluminium temperature.

The above assumptions are therefore considered to be accurate for the modelling in the current study. The contact and friction models are developed according to this framework.

3.3.2 The fully plastic contact model

Under the above-mentioned deterministic approach of describing contact, a new contact model based on contact patches developed for fully plastic contact in aluminium extrusion is presented. In this model, the constitutive behaviour of aluminium alloys as a function of temperature and strain rate is taken into account.

According to Johnson [71], a representative strain can be defined for the plastic deformation beneath a static spherical indenter:

$$e_{rep} = 0.2\, a/b \tag{3.15}$$

When the contact patch is not too sharp, Eq. 3.15 can be extended to indentation by an elliptical paraboloid. Therefore, the contact radius can be expressed by Eq. 3.12 and an effective tip radius can be obtained according to [33]:

$$b_{x,epp} = \frac{A_{epp}{}^2}{4pV_{epp}\,l};\; b_{y,epp} = \frac{l\,A_{epp}{}^2}{4pV_{epp}} \tag{3.16}$$

$$b_{eff} = \sqrt{b_x b_y} = \frac{a_{mj} a_{mn}}{2w} \tag{3.17}$$

The representative strain for an elliptical paraboloid in static contact can be

expressed by substitution of Eq. 3.12 and Eq. 3.17 into Eq. 3.15:

$$e_{rep,st} = \frac{0.4w}{\sqrt{a_{mn}{}^2 \cos^2 j + a_{mj}{}^2 \sin^2 j}} \tag{3.18}$$

For plastic contact in sliding condition, the contact area only covers the frontal half of the contacting ellipse, therefore the representative strain is also a half of that in static contact:

$$e_{rep,sl} = \frac{0.2w}{\sqrt{a_{mn}{}^2 \cos^2 j + a_{mj}{}^2 \sin^2 j}} \tag{3.19}$$

The contact time of this contact spot, Δt, can be written as:

$$\Delta t = \frac{a_{epp}}{v} = \frac{a_{mj} a_{mn}}{v\sqrt{a_{mn}{}^2 \cos^2 j + a_{mj}{}^2 \sin^2 j}} \tag{3.20}$$

The local (hereafter referring to the material indented by a contact patch) representative strain rate can then be expressed as:

$$\dot{e}_{rep,sl} = \frac{e_{rep,sl}}{\Delta t} = \frac{0.2wv}{a_{mj} a_{mn}} \tag{3.21}$$

It is clear that although the representative strain depends on the orientation angle φ, the strain rate is independent of this direction; therefore the strain rate is independent of surface anisotropy. The local flow stress and the local contact pressure can then be related to the local representative strain rate and the contact temperature (bulk temperature) using the constitutive relation of the aluminium alloy according to Eq. 2.29:

$$H_{cp}\left(T, \dot{e}_{rep,sl}\right) = 2.8 s_f\left(T, \dot{e}_{rep,sl}\right) \tag{3.22}$$

At a given surface separation, the average contact pressure can be obtained using the above-mentioned procedure. For the contact conditions in the bearing channel, the bearing constrains the material bulk deformation, and thus the volume conservation effect described by Pullen and Williamson [21] should also be considered, as discussed in Section 2.1.1.3. However, it can be seen that the flow stress beneath any contact patch on a rough surface is not constant as the extent of strain rate hardening of the material depends on the geometry of the indenting contact patch. In order to incorporate the effect of volume conservation, an average contact pressure is defined as a volume-weighted parameter as follows:

$$\overline{H}(T,v,x)=\sum_{i=1}^{n}\frac{H_{i,cp}V_{i,cp}}{\sum_{i=1}^{n}V_{i,cp}} \tag{3.23}$$

Replacing the H term in Eq. 2.15 with the average contact pressure, the actual degree of contact at a given surface separation can be obtained by:

$$a_1(T,v,x)=\frac{p_n}{\overline{H}(T,v,x)+p_n} \tag{3.24}$$

In the meantime the degree of contact can be obtained by truncation of the rough surface according to the complementary cumulative distribution function, as expressed in Eq. 3.1. The dimensionless surface separation ξ can be obtained by solving the following nonlinear equation:

$$\frac{p_n}{\overline{H}(T,v,x)+p_n}=\int_{xs}^{+\infty}f(z)dz \tag{3.25}$$

For a Gaussian surface with a surface height PDF described by Eq. 3.26, the complementary cumulative distribution function can be written as in Eq. 3.27:

$$f(z)=\frac{1}{s}\frac{1}{\sqrt{2p}}\exp\left(-\frac{z^2}{2s^2}\right) \tag{3.26}$$

$$a_2(x) = \frac{1}{4}\operatorname{erfc}\left(x/\sqrt{2}\right) \tag{3.27}$$

The effective contact pressure over the surface is larger than the average contact pressure due to volume conservation, and can be written as:

$$H_{eff}(T,v,x) = \overline{H}(T,v,x) + p_n \tag{3.28}$$

The effective contact pressure takes account of the resistance of displacing the deformed volume and should be used in friction calculation. An iterative solving procedure is implemented to obtain convergence of the nonlinear equations, as shown in Fig. 3.9.

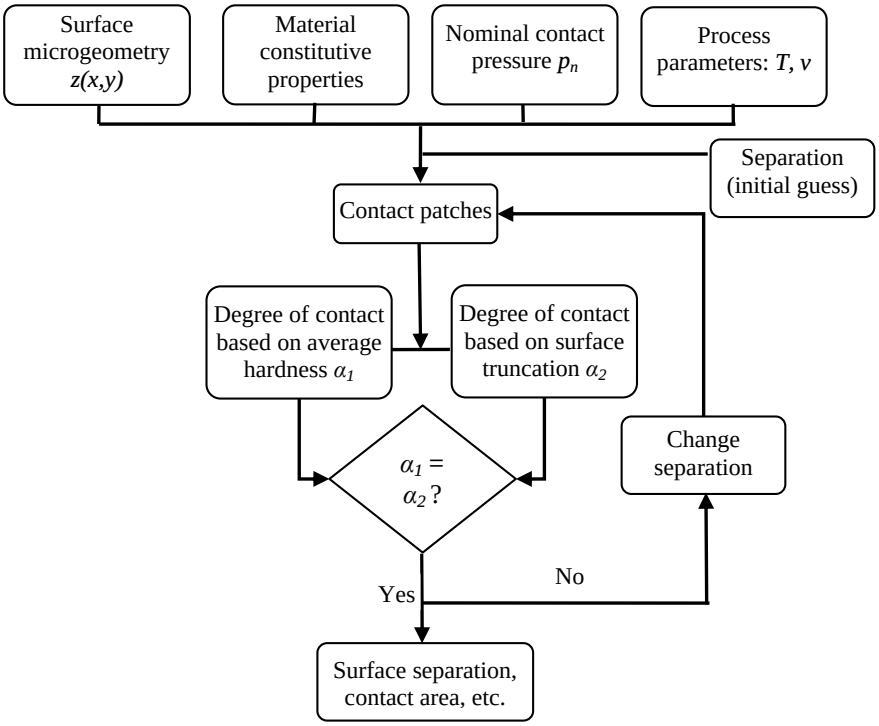

Fig. 3.9 Flow diagram of the iterative procedure for the contact & friction model.

As discussed, the newly developed contact model incorporates the effect of contact coalescence at high nominal contact pressure, the constitutive behaviour of

aluminium alloys. The surface microgeometry can be accurately modelled by elliptical paraboloids instead of spheres.

3.3.3 Results and discussion

3.3.3.1 Effect of process parameters

Process parameters, e.g. contact temperature and sliding speed, determine the flow stress of the deformed material, and thus influence contact situations in aluminium extrusion processes. The effects of temperature and sliding speed are shown in Fig. 3.10:

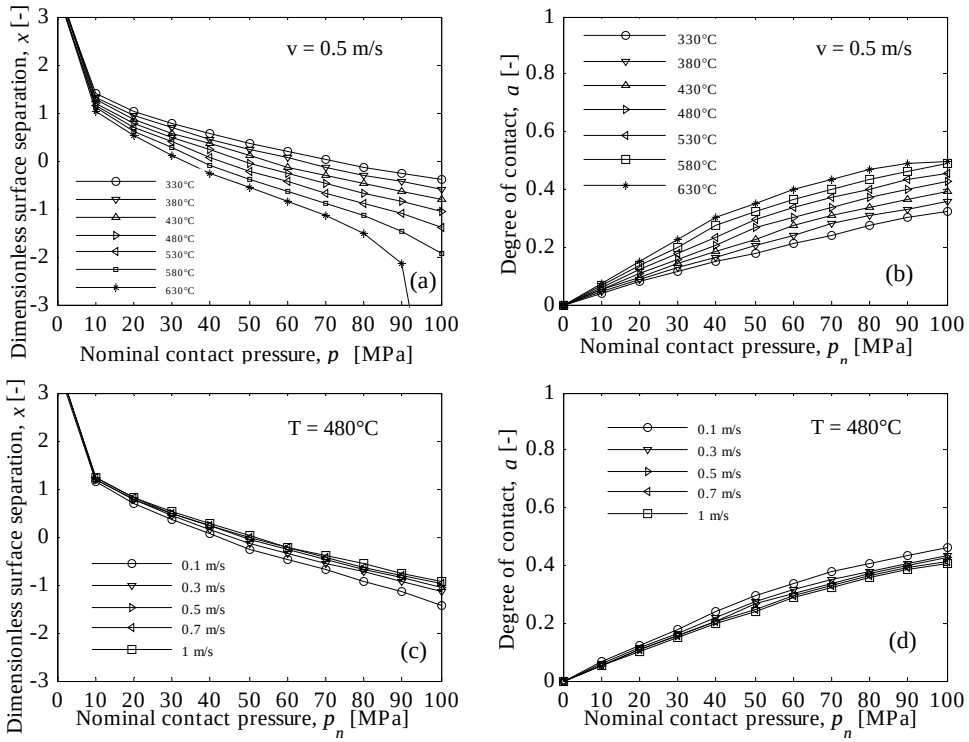

Fig. 3.10 Effect of temperature and sliding speed on the contact situations: (a) & (c) dimensionless separation; (b) & (d) degree of contact.

The temperature and sliding speed ranges are typical of aluminium extrusion processes. It can be seen that the contact area increases when temperature is increased or sliding speed is reduced due to softening of the material. It should be

noted that the effect of temperature is much more significant than that of the sliding speed, indicating that during the extrusion of aluminium alloys, variation of temperature has substantial effects on the contact situation.

3.3.3.2 Effect of surface topography

Surface topography dictates the strain rate of the deformed material in contact. The effect of surface roughness and the bandwidth parameter is shown in Fig. 3.11:

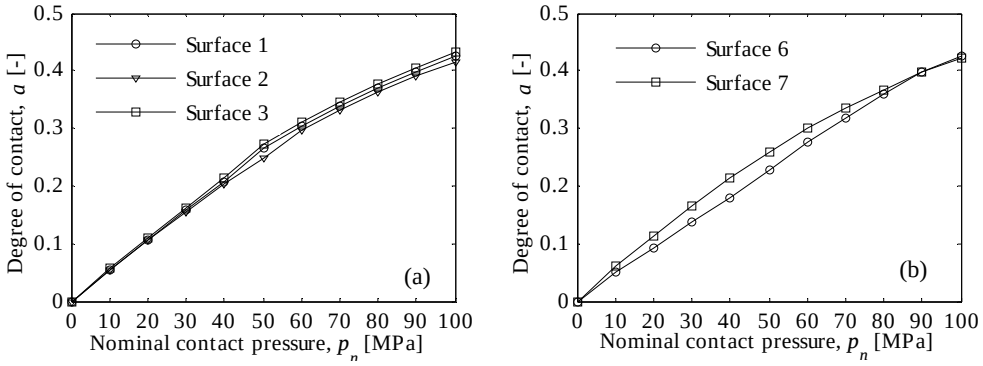

Fig. 3.11 Effect of surface topography on the degree of contact: (a) effect of surface roughness; (b) effect of the bandwidth parameter.

Since the strain rate hardening effect does not significantly alter the contact situations, the effect of surface topography is only marginal.

3.4 Friction model

3.4.1 Applying the Challen and Oxley model

The coefficient of friction of a pair of contacting surfaces is obtained by dividing the total friction force by the total normal load, as given below:

$$F_{fr} = \sum_{i=1}^{n} m_{i,cp} H_{eff} A_{i,cp} \tag{3.29}$$

$$F_N = p_n A_n = H_{eff} A_r = H_{eff} \sum_{i=1}^{n} A_{i,cp} \tag{3.30}$$

$$m = \frac{F_{fr}}{F_N} = \frac{\sum_{i=1}^{n} m_{i,cp} A_{i,cp}}{\sum_{i=1}^{n} A_{i,cp}} \tag{3.31}$$

The total normal and friction forces are the summation of the contribution of each contact patch. The coefficient of friction of each contact patch is obtained by using the friction model of Challen & Oxley [37], relating the effective attack angle as calculated by Eq. 3.13 and the interfacial shear factor f_{hk}, which is influenced by the shear strength of the interface and the bulk material. However, since the shear strength of the interface τ_{int} reflects adhesion between the contacting pair, it depends on a number of factors, including state of lubrication, local contact condition and chemistry, etc. For dry contact it can reach unity, which is the upper limit [72]. The contact condition in our study is typically dry contact with partial oxidation, hence an adhesive joint is formed at the interface. An expression for such situations is proposed for the shear strength of an adhesive interface:

$$t_{\text{int}} = c_1 L_H r \ln(\frac{T_m}{T}) \exp(-c_2 v) \tag{3.32}$$

Where L_H (3.98×10^5 J/Kg) is the latent heat of fusion of aluminium alloys, ρ (2.7×10^3 kg/m^3) is the density of aluminium alloys and T_m (933 K) is the melting point and T_{int} is the interfacial temperature.

This expression takes into account the shear strength of the adhesive joint when two metallic surfaces are allowed to slide at the interface [73][74]. The additional velocity term is included according to Tverlid [27] to incorporate the effect of "velocity weakening": as the sliding speed is increased, the time in which this adhesive bonding can occur is reduced, therefore decreasing the shear strength of the adhesive joint. In the case of surface sticking ($v = 0$) the exponential factor will take the value of unity. This suggests that there is no velocity weakening as there is sufficient time for the adhesive joint to form completely. The fitting parameters c_1 and c_2 are likely to vary when the local contact conditions change, e.g. chemistry of the contacting pair, temperature, etc. A complete set of data can be retracted from Tverlid and Abtahi's extrusion experiments in which the interfacial conditions are

similar to the current study; therefore following the approach discussed in Section 3.5, the fitting parameters can be obtained for our contact situations (AA 6063 – case hardened steel). The interfacial shear factor thus takes the form:

$$f_{hk} = \frac{t_{\text{int}}}{k} = \frac{0.13 L_H \, r \, \ln(\frac{T_m}{T}) \exp(-0.496 v)}{s_f(T, \dot{\varepsilon}) / \sqrt{3}} \tag{3.33}$$

In this way, f_{hk} can be determined as a function of temperature, sliding speed and strain rate. Referring the data for constitutive equations of other aluminium alloys in Appendix G, it is possible to deduce f_{hk} value for other alloys, as further discussed in Chapter 9. A satisfactory fit with experimental data from the literature can be shown in Fig. 3.12 :

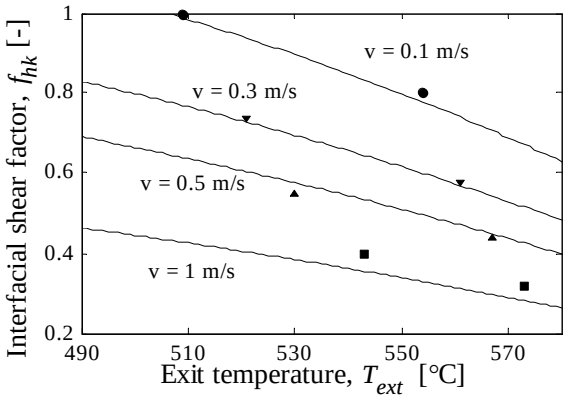

Fig. 3.12 Fitted interfacial shear factor curve and the original Tverlid & Abtahi data: ● Experiments with exit speed 0.1m/s ; ▼ Experiments with exit speed 0.3m/s; ▲ Experiments with exit speed 0.5 m/s; ■ Experiments with exit speed 1 m/s.

Moreover, the upper limit of unity should be imposed when the calculated f_{hk} according to Eq. 3.33 is larger than unity, or when the contacting pair is made of the same material -- the shear strength of the interface must be the same as that of the bulk material. This occurs when some aluminium is transferred and deposited on the bearing surface, i.e. when the contact patch operates in the wedge – formation regime. Therefore, implementation of the interfacial shear factor f_{hk} takes the following form:

$$f_{hk} = \begin{cases} 1 & \dfrac{t_{\text{int}}}{k} > 1 \quad \text{Or operating in wedge–formation} \\ \text{Eq. 3.33} & \dfrac{t_{\text{int}}}{k} \le 1 \end{cases} \tag{3.34}$$

It should be mentioned that when f_{hk} approaches unity, the Challen & Oxley's model gives complex solutions; also oxidation prevents f_{hk} from achieving unity. An interfacial shear factor of 0.95 is thus used for friction calculation that ensures that the coefficients of friction of most contact patches are real numbers.

3.4.2 Results and discussions

Results in this section are taken from calculations for the numerically generated surfaces as described in Table 3-1. In this section, in order to focus on the friction model, the fully plastic model described in Section 3.3 is not applied for means of clarity. This means that the dimensionless surface separation ξ is varied as inputs instead of being calculated for an applied p_n by the fully plastic contact model presented in Section 3.3. In Section 3.5 the contact model is included to show the effect of temperature and sliding speed.

3.4.2.1 Effect of surface topography

The numerically generated surfaces have been used to study the influence of surface topography on the coefficient of friction. First, the effect of surface roughness is studied using surfaces 1, 2 and 3, as shown in Fig. 3.13:

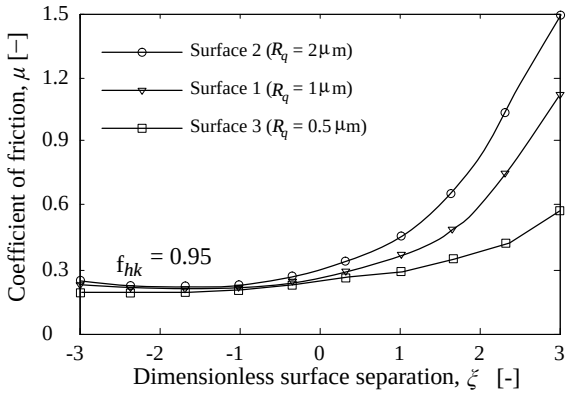

Fig. 3.13 Influence of surface roughness on the coefficient of friction.

It can be seen that as expected, a high roughness value increases the coefficient of friction since sharper contact patches operate in the wedge–formation regime as can be seen from Fig. 3.8 (a). The difference of coefficient of friction caused by roughness is reduced at low surface separation, since the coalesced, blunt contact patches at high nominal contact pressure basically plough through the soft aluminium, and all three curves converge to a low surface separation. The change of shape of the contact patches results in a load-dependent friction, which has been also found by a few other researchers [75] [76] [77]. The same trend can be found by comparing surfaces 4 and 5 for the influence of surface anisotropy and surfaces 6 and 7 for the effect of the bandwidth parameter, as shown in Fig. 3.14:

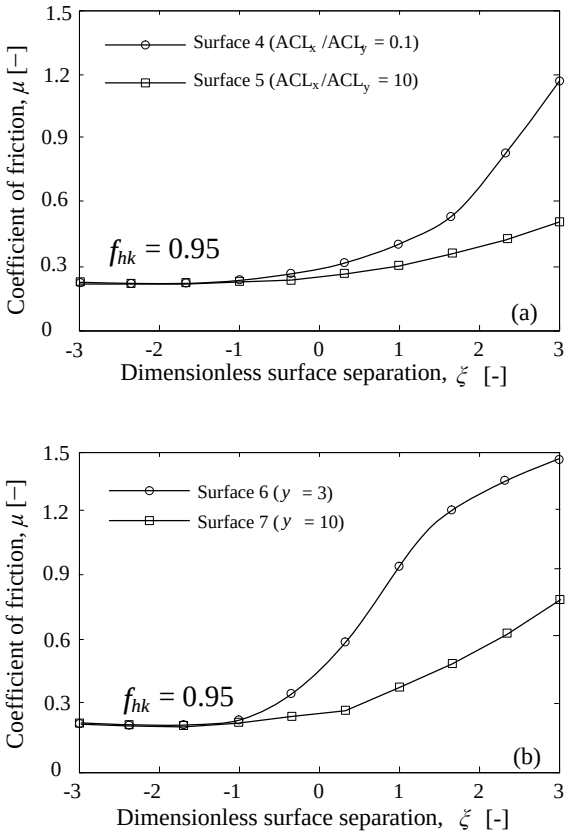

Fig. 3.14 Influence of: (a) surface anisotropy; (b) the bandwidth parameter.

The friction curves correspond with the average effective attack angle curves in

Fig. 3.8. The calculated coefficient of friction is more surface topography dependent at low pressure level, as contact patches follow the geometry of single summits. It can thus be deduced from the above results that the coefficient of friction has a significant dependence on the nominal contact pressure. At low pressure, the coefficient of friction is closely related to surface topography; at high pressure coefficient of friction tends to converge for surfaces with different topography since small details of the surface have already coalesced to form blunter contact patches with similar shapes. In Fig. 3.1 it can be seen that inside the bearing channel of aluminium extrusion, the pressure range renders a dimensionless surface separation in between 0 and -2.5, therefore the implications of this is that in situations with a high nominal contact pressure, e.g. in aluminium extrusion processes, altering surface topography by, for example, polishing has little influence on the friction level.

3.4.2.2 Effect of interfacial shear factor

Apart from the surface topography that changes the attack angle in friction calculation, the interfacial shear factor also affects the coefficient of friction. The effect of interfacial shear factor can be shown in Fig. 3.15:

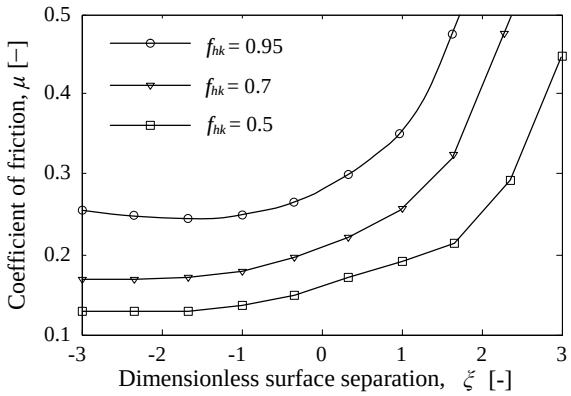

Fig. 3.15 Influence of the interfacial shear factor.

It can be seen that as the strength of the interface decreases, resulting in a decreased f_{hk}, the coefficient of friction is notably reduced, due to: 1) more contact patches operate in ploughing regime where friction is low; 2) weaker adhesive component of the friction. The effect of f_{hk} persists at all pressure levels, and it is more significant at large nominal contact pressure since the adhesive component is more dominant when the contact patches are blunter. It can hence be concluded

that the interfacial shear factor f_{hk} is crucial to the coefficient of friction in situations involving large pressure. Therefore, factors influencing the shear strength of the interface, e.g. temperature, sliding speed, interfacial chemistry, will have a notable effect on the coefficient of friction in aluminium extrusion processes.

3.5 Applying the contact and friction model to aluminium extrusion

3.5.1 The framework

It has been established that there are two zones on the bearing with distinctive tribological characteristics: the sticking zone and the slipping zone. It has been shown that surface defects only form in the slipping zone. Therefore, one of the primary objectives of contact and friction modelling in aluminium extrusion is to calculate the slipping (or equivalently the sticking) length. A framework for contact and friction modelling in aluminium extrusion is set up to cater for different tribological aspects of two different zones on the bearing: The slip point is the separation between the two distinctive tribological zones. Friction in these two zones can be described as following:

- Constant friction stress in sticking zone: as sub-surface plastic deformation occurs, full contact will be achieved in this region and thus the contact patch-based model is not relevant. In this region the friction stress takes the value of the shear strength of the bulk aluminium material. Since it is regardless of the nominal contact pressure, the developed friction model cannot be applied to this region.

- Load dependent friction stress in slipping zone: the coefficient of friction can be calculated by the friction model and friction stress decreases with the nominal contact pressure towards the exit of the bearing.

Given the bearing entrance pressure P_{ent}, the pressure calculation Eq. 2.38 then has to be updated to:

$$p_n(x) = \begin{cases} p_{ent} - \dfrac{l_{\sec}}{A_{\sec}} kx & x < l_{stk} \\ p_{stk \to slp} \exp\left[\dfrac{l_{\sec}}{A_{\sec}} \int_{l_{db}}^{l_{stk}} m(p_n(x)) dx \right] & x \geq l_{stk} \end{cases} \tag{3.35}$$

The coefficient of friction $\mu(p_n(x))$ can be calculated by the developed contact and friction model and is load dependent as discussed above. The friction stress inside the whole bearing channel can be schematically illustrated in Fig. 3.16 (a) and a comparison with Tverlid's FEA results is provided in Fig. 3.16(b):

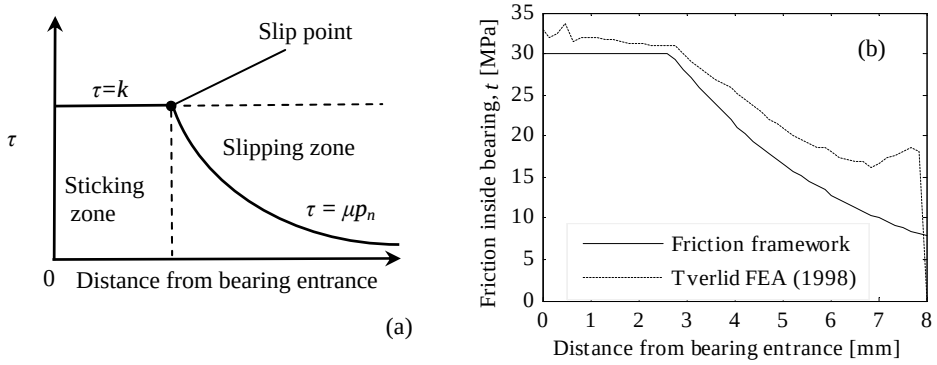

Fig. 3.16 Friction condition inside the bearing channel: (a) a schematic illustration of the proposed friction framework; (b) A comparison with Tverlid's FEA results (μ = 0.3 as input in Eq. 3.35).

During the calculation the same temperature and exit speed conditions from [26] were used. Since surface topography is of little influence, surface 1 of our numerically generated surface has been used. It can be seen that the proposed friction framework fits well with the FEA results except the exit region of the bearing where discrepancy is caused by the effect of the perpendicular flow as modelled in the FEA at this region that creates an additional component to the nominal contact pressure [26]. This effect deviates the pressure distribution along the cross section of the profile from being even, which is an assumption in our model.

The flow chart of sticking / slipping length calculation is summarised in Fig. 3.17:

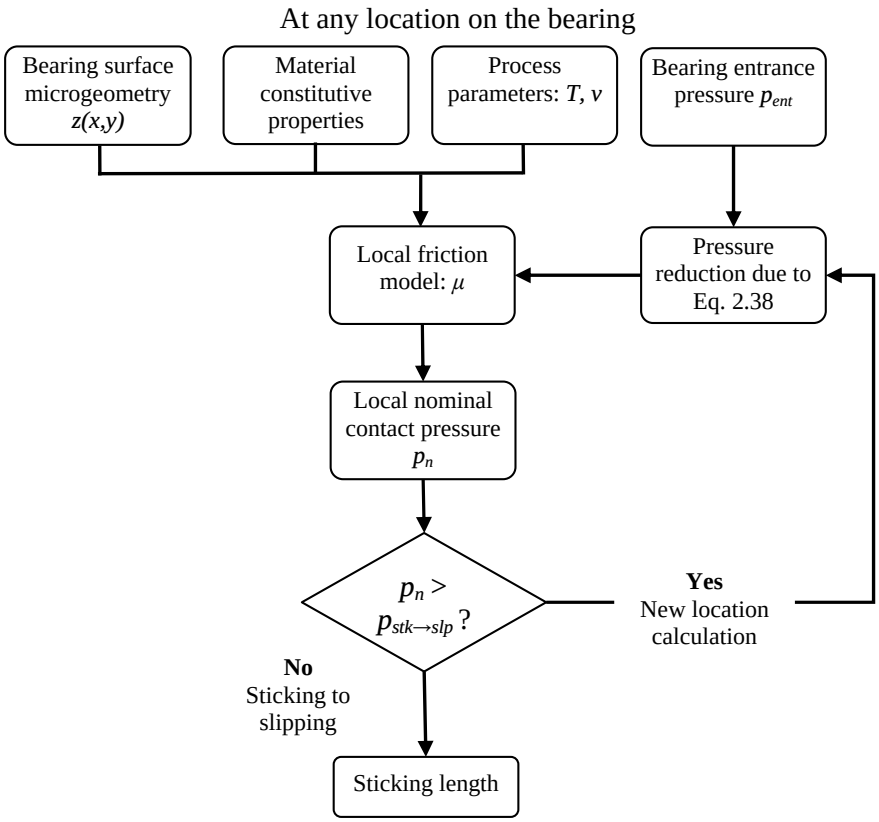

Fig. 3.17 Flow diagram of sticking/slipping length calculation.

3.5.2 Results and discussion

The input values are boundary conditions such as the bearing entrance pressure p_{ent} and process parameters such as temperature and sliding speed, and bearing microgeometry. The objective is to obtain the coefficient of friction along the bearing and hence calculate the length of the slipping (sticking) zone. The numerically generated surfaces (see Table 3-1) were used in the calculation. It should be pointed out, that according to Eq. 3.35, a large dimensionless bearing entrance pressure $p_{ent}/p_{stk \rightarrow slp}$ will apparently elongate the sticking length. Therefore any means that elevate the pressure level inside the bearing channel will increase the length of the sticking region, e.g. using a choked bearing or increased extrusion ratio. Study of this factor is not included in this section by fixing the dimensionless bearing entrance pressure. This will be elaborated in Chapter 4.

3.5.2.1 Effect of surface topography

The boundary conditions used in this section can be summarised in Table 3-2:

Table 3-2 Boundary conditions.

Boundary conditions / Process parameters	p_{ent} (MPa)	Temperature T (°C)	Exit speed v (m/s)	Surface microgeometry	Profile geometry (mm)	Bearing length (mm)
Values	200	500	0.1	Numerically generated surfaces	w = 15 t = 2	8

The coefficient of friction and the sticking length calculated for the numerically generated surfaces with different roughness values are shown in Fig. 3.18:

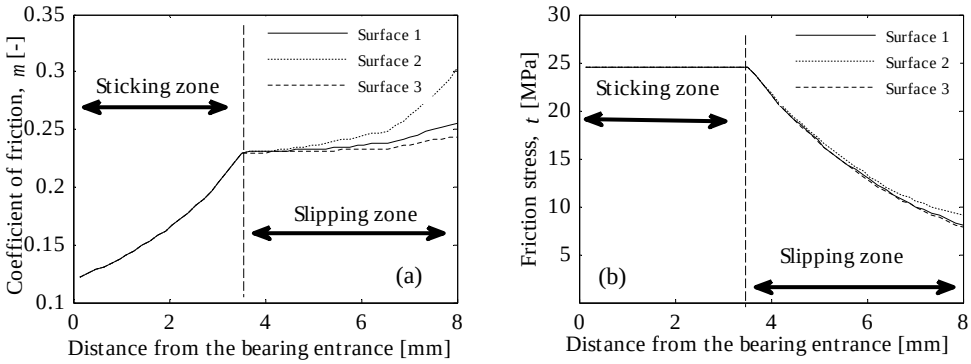

Fig. 3.18 Friction as calculated by the proposed friction model for surfaces with different roughness values: (a) coefficient of friction; (b) friction stress.

It can be seen that in the sticking region the coefficient of friction increases as the nominal contact pressure decreases towards the slip point, while the friction stress remains constant, being equal to the shear strength of the bulk material. In the slipping region the coefficient of friction can be calculated by the friction model. The coefficient of friction for surfaces with different roughness values only differs at the exit part of the bearing where the nominal contact pressure is low and the effect of contact coalescence is not significant. It can also be shown that the same conclusion can be drawn for surfaces with different anisotropy and the bandwidth parameters. Therefore, under practical conditions (roughness values 0.1 ~ 2 μm) surface topography has little influence on the length of the sticking (or slipping)

zone. According to the calculations, it suggests that in terms of the length of the two tribological zones on the bearing, the finishing process of the bearing surface, e.g. polishing, grinding, etc. is of little influence.

3.5.2.2 Effect of process parameters

The most important process parameters for contact and friction calculation are temperature and sliding speed, and they refer to the extrudate surface temperature T_{ext} and exit speed v_{ext} in aluminium extrusion processes. However, if a constant p_{ent} is input in the model, it will result in a change of the dimensionless bearing entrance pressure as temperature and speed vary, according to Eq. 3.35. This dimensionless bearing entrance pressure can be defined as the ratio between p_{ent} and the flow stress of the bulk aluminium. In actual extrusion processes, for a fixed die geometry the dimensionless bearing entrance pressure is unchanged, i.e. harder (or softer) extrudate material due to lower (or higher) temperature and faster (or slower) exit speed result in higher (or lower) bearing entrance pressure. Therefore, variations of process parameters only result in a change in the interfacial shear factor. In order to examine this effect, the input p_{ent} should be chosen such that the dimensionless bearing entrance pressure remains the same for all extrusions. In the current study, $p_{ent}/\sigma = 5$ is chosen. The boundary conditions used in this section are summarised in Table 3-3:

Table 3-3 Boundary conditions.

Boundary conditions	Cond. 1	Cond. 2	Cond. 3	Cond. 4	Cond.5	Cond.6	Cond.7	Cond.8
Temperature T (°C)	450	500	550	600	500	500	500	500
Exit speed v (m/s)	0.1	0.1	0.1	0.1	0.01	0.1	0.3	0.5
p_{ent} (MPa)	230	198	170	147	151	198	222	233

The calculated coefficient of friction and friction stress can be shown in Fig. 3.19:

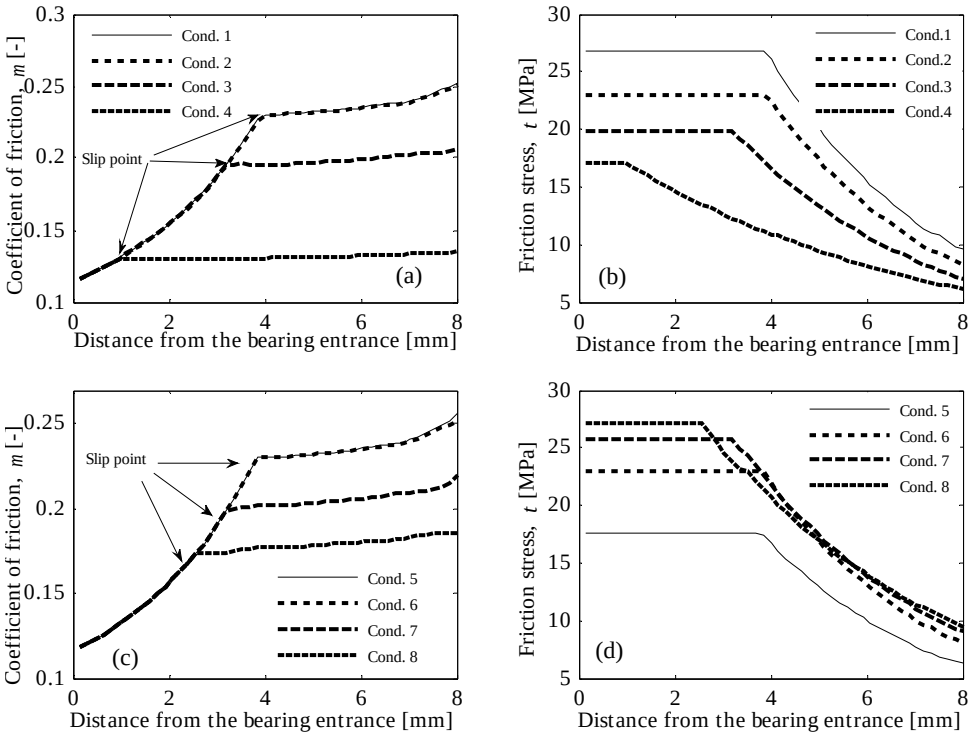

Fig. 3.19 Friction calculated by the proposed friction model for different process parameters: (a) & (b) effect of bearing temperature; (c) & (d) effect of exit speed.

It can be seen that the bearing temperature and exit speed have the same effect on friction level inside the bearing channel: as they increase, friction drops, reducing the length of the sticking zone and elongating the slipping zone, as was observed by Abtahi [63] and Tverlid [26]. This attributes to reduction of the interfacial shear factor f_{hk} as temperature or sliding speed increases. The interfacial shear factor at the slip point for the studied conditions can be demonstrated in Fig. 3.20:

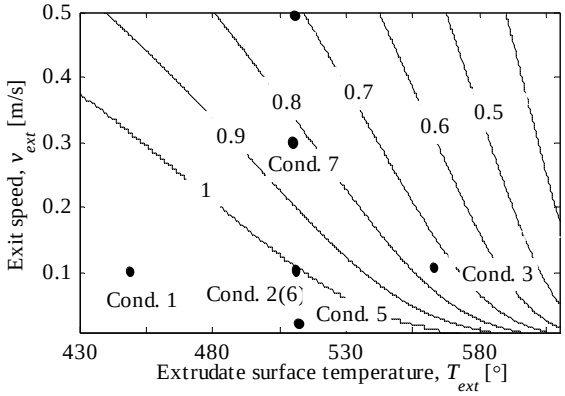

Fig. 3.20 Calculated average interfacial shear factor. Area bounded by the $f_{hk} = 1$ curve and the axes also has $f_{hk} = 1$.

Fig. 3.20 shows that when the temperature (or speed) is low enough, the interfacial shear factor f_{hk} equals unity. Conditions 1 and 2, 5 and 6 are within this area therefore their sticking lengths are exactly the same. As temperature or speed increases, f_{hk} is decreased, resulting in shorter sticking length. When the temperature and speed are too large that a viscous layer is formed at the interface, f_{hk} will drop to almost zero, resulting in zero sticking length. Since the effect of the interfacial shear factor persists at all pressure levels, it is essential to the friction level inside the bearing channel. Therefore, compared to surface topography, variations of bearing temperature or exit speed are much more influential for the tribological aspects inside the bearing channel of aluminium extrusion processes.

It has been established that since surface defects mostly form in the slipping zone, one of the implications is that temperature and exit speed should be lowered to reduce the slipping length in this regard. However, this is not favourable for productivity; therefore an alternative is to increase the P_{ent} to elongate the sticking zone. A more complete study of optimising process parameters is introduced in the following chapters.

3.6 Summary

In this chapter, the newly developed contact and friction models for aluminium extrusion processes are discussed at length.

In Section 3.1 the drawbacks of summit-based contact models are pinpointed. The

summit model is not suitable for applications where pressure is high, as single summits have already joined to form contact patches. Theoretical work concerning aspects of contact patches is reviewed; it has been found that they cannot give full description of the geometry of the contact patches. Therefore, in Section 3.2 a deterministic approach capable of modelling each contact patch as a featured geometry is presented.

A fully plastic model based on contact patches instead of summits is presented in Section 3.3. The contact model also incorporates aluminium alloys' constitutive behaviours by including effects of process parameters, e.g. temperature and sliding speed. Then a friction model is introduced in Section 3.4 based on the load dependent contact model.

The contact and friction models are applied to actual aluminium extrusion conditions in Section 3.5 to obtain the sticking / slipping length. It has been shown that the sticking / slipping length is governed by the level of friction inside the bearing channel. In order to increase the sticking length, the following means can be adopted:

- Increase the nominal contact pressure inside the bearing channel by using choked bearing geometry or increased extrusion ratio.
- Decrease extrudate surface temperature and exit speed to increase the interfacial shear factor f_{hk}. The effect of surface topography is only marginal in this regard, since in high pressure conditions such as in aluminium extrusion processes, contact coalescence eliminates the effect from local surface topography.

Chapter 4
Split die extrusion experiments
Part I: Validation of the contact and friction model

In Chapter 2 and Chapter 3 a contact and friction model developed for aluminium extrusion has been presented. In this chapter, the model is now applied to laboratory extrusion experiments for validation. It has been shown in the previous chapters that an indirect means of evaluating friction inside the bearing channel during extrusion processes is to measure the length of the sticking (or slipping) zone on the bearing surface by using split dies, as previously performed by a number of researchers [26][62][63]. Therefore, by comparing the calculated sticking / slipping lengths with the experimentally obtained values, validation can be achieved.

A split die consists of two die inserts that can be fitted together to form a closed cavity of die opening. The operation of such a device is illustrated in Fig. 4.1 and Fig. 4.2. Three series of laboratory scale split die extrusion experiments have been performed in this study, the main objectives being:

- Part I (series 1): Validate the contact and friction model by measuring the sticking (slipping) length on the die bearing surface after extrusion.
- Part II (series 1, 2 and 3): Characterise pickup formation during aluminium extrusion.

The objective of series 1 experiment is twofold as mentioned above. In this chapter, only Part I of the experiments is discussed. Part II will be discussed in Chapter 8.

4.1 Experimental arrangements

The arrangement of the experimental facilities is schematically shown in Fig. 4.3:

The assembled state during extrusion:

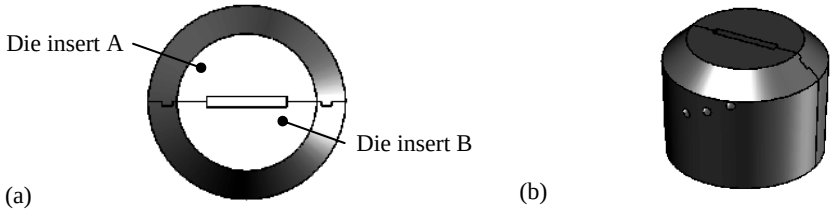

Fig. 4.1 Assembled die inserts during extrusion.

The disassembled state after extrusion:

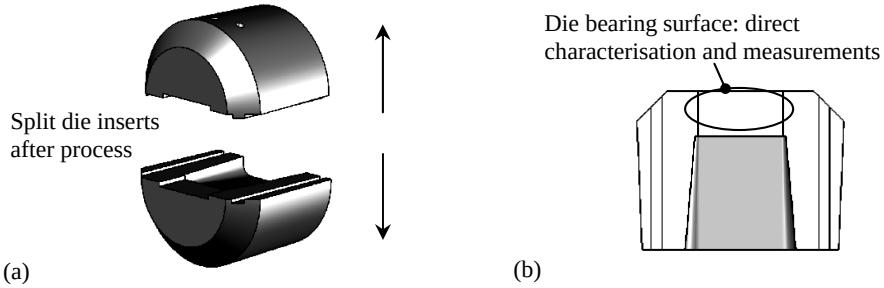

Fig. 4.2 Split die inserts after extrusion for bearing surface characterisation.

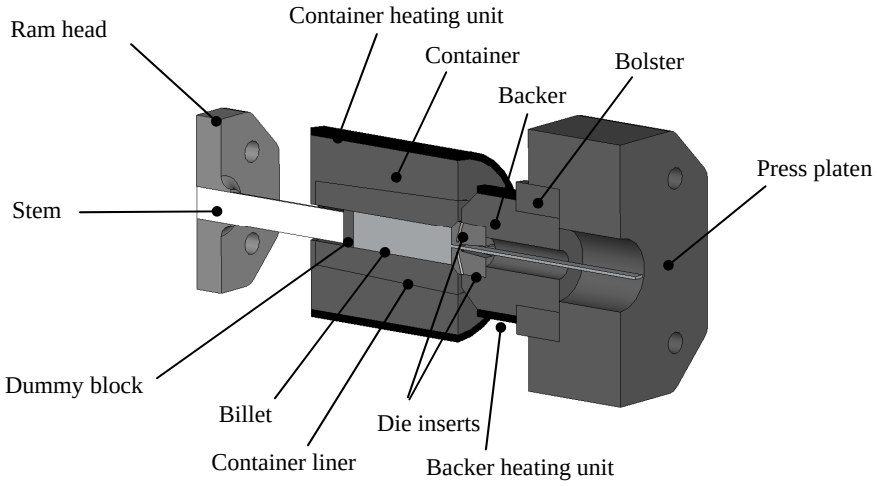

Fig. 4.3 Arrangement of the extrusion setup.

Three main components of the experimental facilities are:

- Press: The extrusion experiments were carried out in TNO's Loire (currently ACB) hydraulic extrusion press, with a capacity of 960 MPa. The dies were pushed together before the actual extrusion and then placed tightly in the backer (die holder). Heating was supplied to the container and the backer, with the die inserts isolated. During upsetting of the billet, the billet temperature became equal to the surrounding container quite rapidly. The ram stroke distance was 90 mm, therefore leaving 10 mm aluminium as the butt–end. After the process the die inserts were retracted from the container and split up.

- Billet: The extrusion billets were aluminium alloy AA 6063 cylindrical billets with a dimension of ø25.4mm×100mm. The billets were properly homogenised before being extruded. The exact chemical composition is specified in Appendix E.

- Die tooling: Impressions of the die inserts are illustrated in Fig. 4.1 and Fig. 4.2. The die opening is a rectangle of width 15 mm and various heights. The die inserts were manufactured with H1.2344 tool steel. The bearing surfaces were manufactured using EDM to give controlled roughness values. For exact specifications and construction drawings for the die inserts, the reader is referred to Appendix F; in this section the key geometrical variations of the manufactured die inserts are introduced.

  12 pairs of die inserts were manufactured, varying 4 die geometry parameters:
  - Bearing length
  - Bearing angle
  - Profile thickness
  - Bearing surface roughness

  The numbering of die inserts and corresponding geometrical features are summarised in Table 4–1. (Prop. = Proposed; Meas. = Measured). As one of the inputs in the friction model, the real bearing surface topography of each bearing has been measured by interference microscopy. 10 measurements have been made on the bearing surface of die insert B of each pair of die inserts, each covering an area of 640 μm x 480 μm and a pixel size of 1 μm.

Table 4-1 Die geometrical parameters.

Die number[1]	Feature	Die geometry properties							
		l_{db} [mm]		α_{db}[2] [°]		t [mm]		R_q [µm]	
		Prop.	Meas.	Prop.	Meas.	Prop.	Meas.	Prop.	Meas.
4	Reference	8	8	0.33	0.36	2	2	0.5	1.1
5	Reference	8	8	0.33	0.37	2	2	0.5	1.1
6	Reference	8	8	0.33	0.32	2	2	0.5	0.9
7	Reference	8	8	0.33	0.33	2	2	0.5	0.7
8	Reference	8	8	0.33	0.33	2	2	0.5	0.7
9	Reference	8	8	0.33	0.34	2	2	0.5	0.9
10	Short bearing	5	5	0.33	0.38	2	2	0.5	0.7
11	Parallel	8	8	0	-0.02	2	2	0.5	0.9
12	Relieved	8	8	-0.33	-0.32	2	2	0.5	1.0
13	Rough bearing	8	8	0.33	0.33	2	2	2.0	2.0
14	Smooth bearing	8	8	0.33	0.32	2	2	0.1	0.4
15	Thin profile	8	8	0.33	0.34	1	1	0.5	1.0

This setting has been chosen to obtain a sufficient resolution whilst covering a relatively adequate sampling area. In order to describe the surface topography as accurately and representatively as possible, the following procedure has been taken to select the "most representative surface topography" for one particular die insert to be used in model validation:

- Obtain surface height PDF for each measurement $\Phi_1(z)$, $\Phi_2(z)$, …
- Since the obtained PDFs are discrete, the "most representative" PDF can be found according to the method of Least square (minimise the residue):

$$\text{Residue} = \int_{\min(z)}^{\max(z)} \sum_{i=1}^{9} \left(\Phi_{rep}(z) - \Phi_{i\neq rep}(z)\right)^2 dz \tag{4.1}$$

  In which $\Phi_{rep}(z)$ is the "most representative" PDF.

- Surface associated with this particular PDF will be used in the model.

[1] Due to manufacturing reasons the numbering did not start from 1; this thesis sticks to this order. Any subsequent quotation of the die inserts is referred to this numbering.
[2] Positive bearing angle means choked bearing (bearing surfaces converge towards the exit). Negative bearing angle means relieved bearing. The actual bearing angle will be changed during extrusion due to elastic deformation of the die.

4.2 Experimental setup

4.2.1 Procedures

In part I of the extrusion experiment (series 1), in order to verify the contact and friction model by measuring sticking/slipping length, a number of boundary conditions / process parameters were varied:

- Bearing length: 8 mm, 5 mm
- Bearing angle: +0.33º, 0, -0.33º
- Profile thickness: 2 mm, 1 mm
- Bearing surface roughness: 1 μm, 2 μm, 0.5 μm.
- Billet temperature: 450°C, 420°C, 570°C
- Exit speed: 17 mm/s, 1.7 mm/s, 85 mm/s

The 12 pairs of die inserts were put in use in turn, each extruding two billets using the “billet on billet” approach. After the extrusion process, the die inserts were retracted from the backer with some adhered aluminium on the bearing surface. No further treatment to the bearing surfaces was performed in series 1 of the extrusion experiment.

4.2.2 Data acquisition

During the extrusion experiments, several key parameters were measured:

- Ram speed (mm/s): the forward speed of the ram is calculated by the measured ram displacement curve. The exit speed can be obtained by multiplying the ram speed by the extrusion ratio.

- Extrusion force (MN): the extrusion force was measured during extrusion by multiplying the ram pressure by the cross – section area of the container. The bearing entrance pressure p_{ent} is obtained according to Eq. 2.33.

- Die temperature (°C): The die temperature is measured by 6 thermocouples that were placed 2.3 mm beneath the bearing surface, as shown in Fig. 4.4:

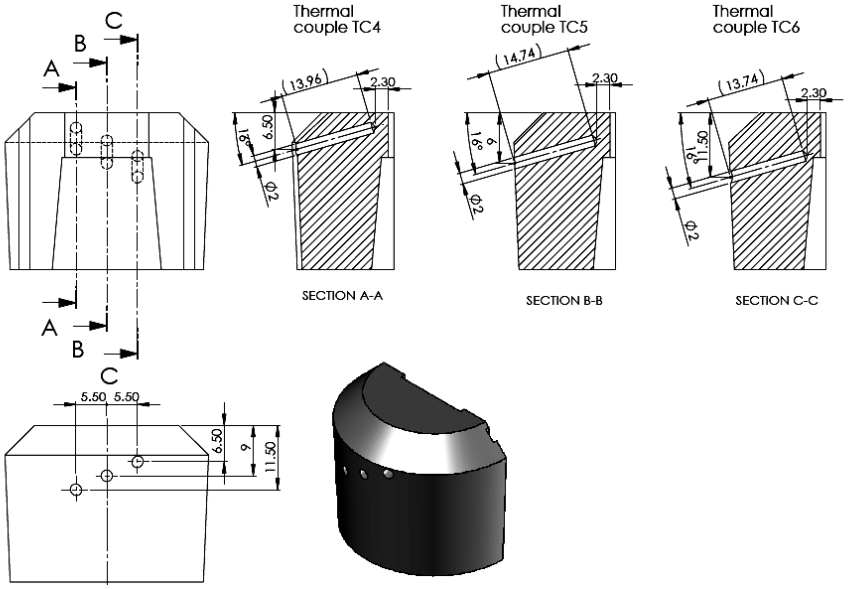

Fig. 4.4 Placement of thermocouples beneath the bearing.

The distance of 2.3mm from the bearing surface was chosen so that placement of the thermocouples would not jeopardise the stiffness of the bearing. The temperatures that are of interest are the extrudate surface temperature and the bearing surface temperature. However, the current setting of die temperature will give a reading different from the actual bearing surface temperature [78], therefore it was calibrated by a FEA model of the die heating. The bearing surface temperature and the extrudate surface temperature can be obtained from the results. Hereafter the calibrated extrudate surface temperature is presented.

4.2.3 Measurement results

It was found that temperature and extrusion force readings during extrusion of the second billets were very close to readings taken from the first billets; therefore an average of the readings from the 2 billets has been used. The extrusion readings of series 1 are given in Table 4-2:

Table 4-2 Extrusion measurement from series 1 experiment.

Extrusion runs	Die	Temperature [°C]			Speed [mm/s]		Pressure [MPa]	
		Billet	Extrudate surf.	Increase	Ram	Exit	Breakthrough	End
Reference	4	445	476	31	1	16.9	670	388
Short bearing	10	449	474	25	1	16.9	576	301
Parallel bearing	11	445	474	29	1	16.9	700	191
Relieved bearing	12	451	478	27	1	16.9	669	195
Rough bearing	13	449	480	31	1	16.9	671	392
Smooth bearing	14	451	483	32	1	16.9	677	385
Thin profile	15	452	497	45	1	16.9	800	620
Low T	5	417	448	31	1	16.9	800	443
High T	6	576	596	20	1	16.9	356	323
Fast 1	7	447	493	46	2.5	42.3	760	403
Fast 2	8	447	488	41	5	84.5	800	409
Slow	9	448	472	24	0.1	1.69	483	287

4.3 Measurement of sticking / slipping length on the bearing surface

4.3.1 Appearance of the bearing surface after extrusion

A clear separation marking can be seen on the bearing surface after the extrusion process between sticking/slipping zones on the bearing, as shown in Fig. 4.5:

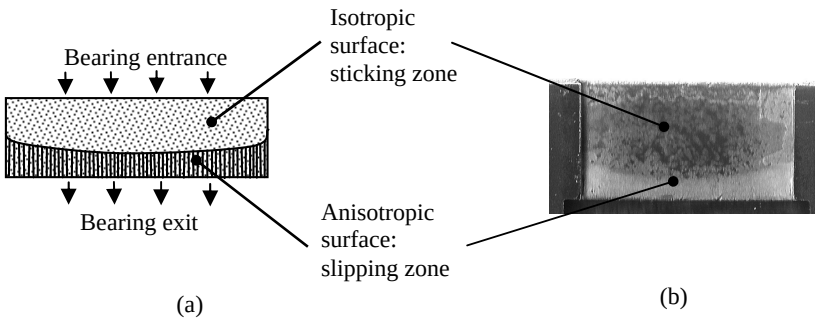

Fig. 4.5 A clear separation marking is visible on post-extrusion die bearing surfaces: (a) A schematic drawing of the sticking–slipping transition on the bearing surface, shown together is the surface topography in these two zones; (b) A photo taken of die #4, similar to Fig. 2.19, suggesting repeatability of this observation.

This marking is curved, bending towards the bearing entrance, attributed to a larger contact pressure in the middle due to velocity gradient along the cross section.

A transfer adhesive aluminium layer was present in the slipping zone whereas in the sticking zone it was absent, revealing the original bearing surface topography. This finding is consistent with other split die researchers' observations [26] [63]. The topography of two zones were analysed by interference microscopy. Anisotropic surface topography featuring surface microgeometry aligned in the extrusion direction could be observed in the slipping zone, whereas isotropic surface topography, one close to the original bearing surface topography prior to extrusion, was observed in the sticking zone:

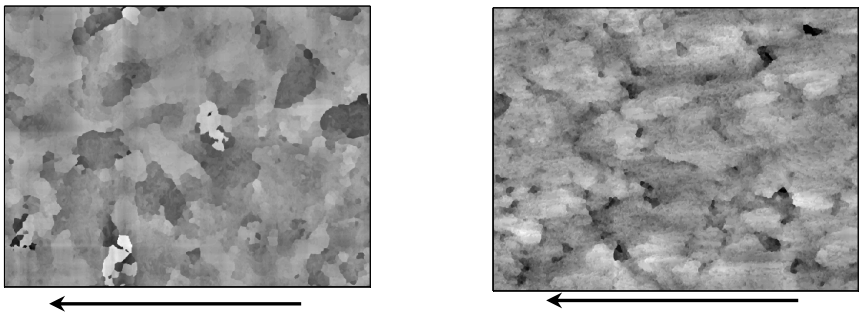

Fig. 4.6 Surface topography after series 1 extrusion in sticking and slipping zones: (a) isotropic surface topography in sticking zone; (b) anisotropic surface topography in slipping zone. Arrows indicate extrusion direction.

Surface roughness of the bearing was measured before and after extrusion:

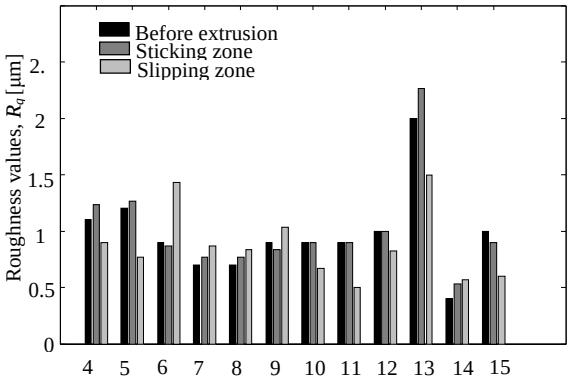

Fig. 4.7 Roughness of bearing surfaces before and after extrusion.

It can be seen that the roughness of the sticking zone is very similar to the die bearing surface prior to extrusion, suggesting that sliding between the die and extrudate was absent in the sticking zone during extrusion runs. This means the bearing surface is covered (protected) by a stationary layer, shortly after the start of the extrusion, eliminating any sliding contact between the extrudate and the bearing surfaces. On the contrary, in the slipping zone, the roughness values are quite different after extrusion; ridges (called “micro–hill” by Abtahi [63]) are aligned along the extrusion direction. This suggests sliding contact in the slipping zone.

4.3.2 Results

The sticking / slipping length has been considered as an indicator for the friction inside the bearing channel. Since the separation marking is curved, 10 measurements were taken on each die insert B, evenly distant between each other along the width of the bearing. The sticking length was then taken as the average value of the 10 measurements on each bearing surface, as shown in Table 4-3:

Table 4-3 Sticking / slipping length measurement in series 1 extrusion experiment.

Die number	4	5	6	7	8	9	10	11	12	13	14	15
Bearing [mm]	8	8	8	8	8	8	5	8	8	8	8	8
Sticking [mm]	5.5	5.6	2.9	5.6	5.1	4.8	2.1	0	0	5.9	5.8	7.0
Slipping [mm]	2.5	2.4	5.1	2.4	2.9	3.2	2.9	8	8	2.1	2.2	1.0

4.3.3 Model validation and discussion

In order to validate the contact and friction model, the measured temperature, exit speed and pressure values were input in the model. Using the approach illustrated in Fig. 3.17, the sticking length for each particular die insert was calculated, using f_{hk} value expressed in 3.33. A comparison between calculation and experiment is shown in Fig. 4.8.

It can be seen that the model and measurements are in very good agreement. Since the sticking length is directly related to the coefficient of friction (Eq. 3.35), the agreement suggests that the friction model developed in Chapter 3 is valid for aluminium extrusion processes.

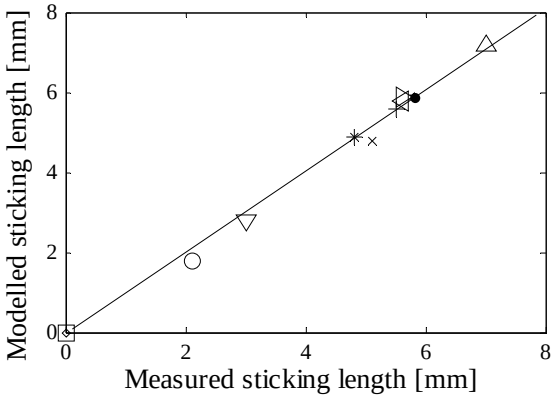

Fig. 4.8 Comparison between modelling and experiment of sticking length: + Reference extrusion; o Short bearing; ◊ Parallel bearing; □ Relieved bearing;☆Rough bearing; ● Smooth bearing; Δ Thin profile; ▷Low temperature; ▽ High temperature; ◁Fast exit speed 1; x Fast exit speed 2; * Slow exit speed.

There are a number of factors that are related to the friction level inside the bearing: surface topography of the bearing, process parameters such as bearing temperature, exit speed and the nominal contact pressure on the bearing. However, their effects on the sticking / slipping length are quite different. It should then be emphasised that according to Eq. 2.40, the coefficient of friction at the slip point is inversely proportional to the nominal contact pressure at that location on the bearing (since coefficient of friction is load-dependent), $P_{stk \rightarrow slp.}$. This shows that if the coefficient of friction between the contacting surfaces is high, only a small contact pressure is needed for sticking to occur and vice versa.

The influence of die geometry is obvious. Changing the die geometry can influence: 1) the nominal contact pressure inside the bearing channel by using different die bearing angles (Dies # 10, 11, 12) or different bearing lengths (Die # 10); 2) the perimeter/area ratio as introduced in 2.2.2.2 (Die # 15). It can be seen from Eq. 3.35 that a higher bearing pressure results in a longer sticking length. More precisely, the dimensionless bearing entrance pressure determines the sticking length. It can be also seen that a large perimeter/area ratio results in a much larger pressure gradient in the bearing, e.g. for complex profile geometry. The calculated coefficient of friction can be shown in Fig. 4.9.

It is clear that as the bearing geometry changes, sticking length is substantially affected. The sticking zones on the relieved and parallel bearing dies have completely vanished due to a very low bearing entrance pressure. Since the pressure is low, this also leads to a higher coefficient of friction than other

extrusions, as explained by the load-dependent friction model.

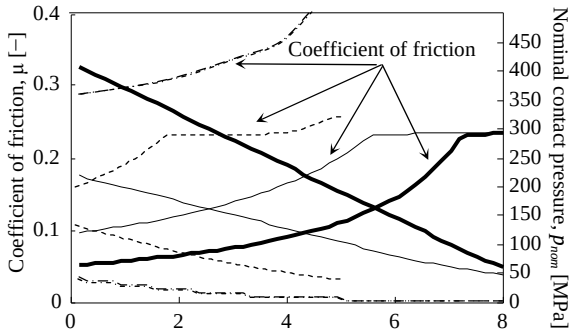

Fig. 4.9 Calculated coefficient of friction and nominal contact pressure along the bearing channel with die geometry: — Reference extrusion (l_{db} = 8 mm, α_{db} = 0.33º, t = 2 mm); — — Short bearing (l_{db} = 5 mm, α_{db} = 0.33º, t = 2 mm); — ·Relieved bearing (l_{db} = 8 mm, α_{db} = -0.33º, t = 2 mm); —·Parallel bearing (l_{db} = 8 mm, α_{db} = 0, t = 2 mm, coincide with the relieved bearing curves); ▬ Thin profile (l_{db} = 8 mm, α_{db} = 0.33º, t = 1mm).

The short bearing die, the reference die and the thin profile die have the same coefficients of friction at the slip point, but sticking lengths are vastly different due to completely different pressure levels inside the bearing channel. Note that the curves for parallel and relieved bearing actually coincide, since their pressure levels were very close. However, they were quite different from a choked bearing. This can be explained by the study of Lof [54], who showed that there is a remarkable increase in extrusion pressure when the bearing becomes even slightly choked.

Process parameters such as extrudate surface temperature and exit speed can also affect the coefficient of friction by varying the interfacial shear factor f_{hk}, as defined in Eq. 3.33. Dies # 5 ~ 9 were used to extrude with varied billet temperatures and exit speeds. The calculated coefficient of friction can be shown in Fig. 4.10. It is clear that of the five extrusion runs performed with different billet temperatures and exit speeds, the coefficients of friction at the slip point are the same except the high temperature extrusion, which is lower. Again, this can be explained by the interfacial shear factor f_{hk}, as shown in Fig. 4.11.

Due to limitations of the press arrangement, only the high temperature extrusion was able to obtain an f_{hk} value of 0.8 and the other extrusion runs were well in the range of unity. According to the friction model introduced in Chapter 3, a reduced

f_{hk} value results in an overall decrease of the coefficient of friction at all pressure levels, which corresponds to the entire slip zone on the bearing area, therefore this leads to a shorter sticking length.

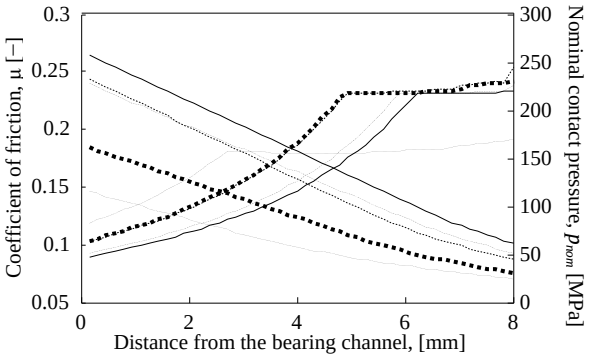

Fig. 4.10 Calculated coefficient of friction and nominal contact pressure along the bearing channel with different billet temperatures and exit speeds: — Low temperature (T_{ext} = 448°C, v_{ext} = 16.9 mm/s); — — High temperature (T_{ext} = 596°C, v_{ext} = 16.9 mm/s); — – Fast exit speed 1 (T_{ext} = 493°C, v_{ext} = 42.3 mm/s); - - Fast exit speed 2 (T_{ext} = 488°C, v_{ext} = 84.5 mm/s); ▪ ▪ Slow exit speed 2 (T_{ext} = 472°C, v_{ext} = 1.7 mm/s).

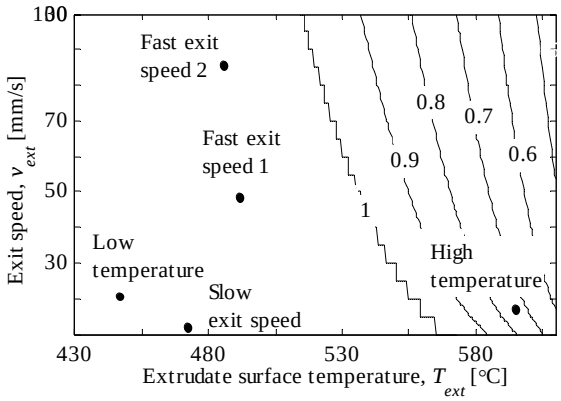

Fig. 4.11 Calculated interfacial shear factor for extrusion experiments.

In a nutshell, the coefficient of friction in the slip zone on the bearing will first remain unchanged as extrudate surface temperature and exit speed increase when the f_{hk} value is unity, then it will decrease as f_{hk} starts to reduce. The sticking zone can be completely eliminated if coefficient of friction is low enough, for example, when the extrusion speed and extrudate surface temperature are very high.

Finally, the effect of bearing surface roughness (Die # 13, 14) can be shown in Fig. 4.12:

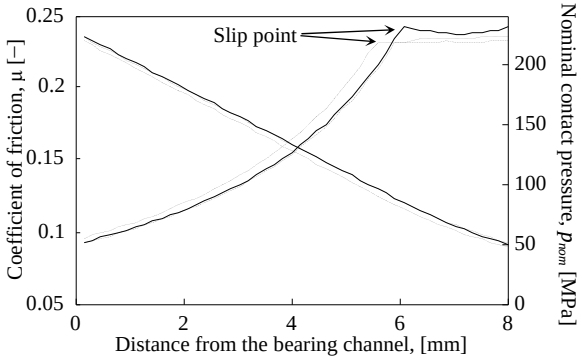

Fig. 4.12 Calculated coefficient of friction and nominal contact pressure along the bearing channel for bearings with different roughness: − Rough bearing; -- Reference die; −· Smooth bearing.

It can be seen that changing surface roughness of the bearing has almost no influence on the sticking / slipping length. The deviation between curves is caused by slightly different dimensionless bearing pressure. The coefficients of friction for bearings of different roughness are very similar, due to the fact that at the slip point the nominal contact pressure is still large enough for contact coalescence to occur, therefore surface topography does not vary the coefficient of friction greatly at the slip point. However, towards the exit of the bearing channel where the nominal contact pressure is lower, according to Fig. 3.13, there will be a difference of coefficient of friction, but in terms of the sticking length, surface roughness of the bearing does not have significant influence.

The implications from the analysis above are thus very clear: the sticking/slipping length on the bearing surface depends on:

- Coefficient of friction at the slip point (changed by f_{hk} value);
- Dimensionless bearing entrance pressure;
- Profile geometry.

It has been shown in the aluminium extrusion process where pressure is usually high, that the sticking / slipping length is not influenced by surface topography, hence surface finish of the bearing. Instead, they are greatly affected by the f_{hk} value, which can be varied by extruding at different extrudate surface temperature

and exit speed combinations. The sticking / slipping length is crucially influenced by the dimensionless bearing entrance pressure and profile geometry. Therefore, changing e.g. the bearing angle, the bearing length or extrusion ratio will have a substantial effect on the sticking / slipping length, even when the coefficient of friction at the slip point is not changed.

4.4 Summary

In this chapter Part I (series 1) of the split die extrusion experiment has been presented. The measured sticking lengths have been compared with the calculated values. It has been shown that the agreement is good. This shows that the developed contact and friction model is suitable to apply to aluminium extrusion processes.

It has been shown that the sticking / slipping length is influenced by the coefficient of friction at the slip point. However, since the nominal contact pressure at the slip point is large, surface topography is of minor influence, as can be seen from dies with different surface roughnesses. Instead, the interfacial shear factor f_{hk} is of essential effect, which is influenced by the extrudate surface temperature and exit speed.

The major effect on the sticking / slipping length comes from the dimensionless bearing pressure; this corresponds to the nominal contact pressure distribution for our model, which can be changed by the geometry of the die, e.g., bearing angle, bearing length, profile geometry etc., which can affect: 1) the dimensionless bearing entrance pressure; 2) the perimeter / area ratio. They alter the pressure distribution inside the bearing channel and thus affect the sticking / slipping length, although the coefficient of friction at the slip point is of little difference.

Chapter 5
On the formation of surface defects of aluminium extrusion products

The previous chapters have discussed and presented a contact and friction model that can be applied to the bearing channel in aluminium extrusion processes. With this model, the sticking / slipping length on the bearing surface can be readily calculated. These all serve one purpose: to model the extent of surface defects formed on the product. In the context of this study, it is assumed that they are closely related to a specific type of defect — surface pickups on aluminium extrusion products, which can even form when operating in the process window. The next step was to understand how they are formed during the process. Existing knowledge is that a number of factors can contribute to pickup formation, both mechanically and metallurgically, as discussed in Chapter 1. It is believed that both mechanical and metallurgical contributions are present, therefore controlling pickup formation probably should involve both heat treatment of the billet prior to the extrusion process, and thermomechanical tailoring during the process by using optimised process parameters. In the context of this study, the latter will be stressed, and a model will be developed for optimisation of in-process control.

In order to understand the formation mechanism, surface pickups found on as - extruded AA 6063 product surfaces have been characterised [79]. The lab analysis was performed on a lot of pickups, and all the results show good consistency. The highlights will be presented in this chapter and a formation mechanism will be proposed based on the findings. SEM, EDX and LSCM pictures are all taken from the internal report regarding this analysis with the consent of the author.

5.1 Morphology study

5.1.1 General appearance of surface pickups

Optical microscopy and SEM were used to obtain impressions of pickups. A typical surface pickup is shown below:

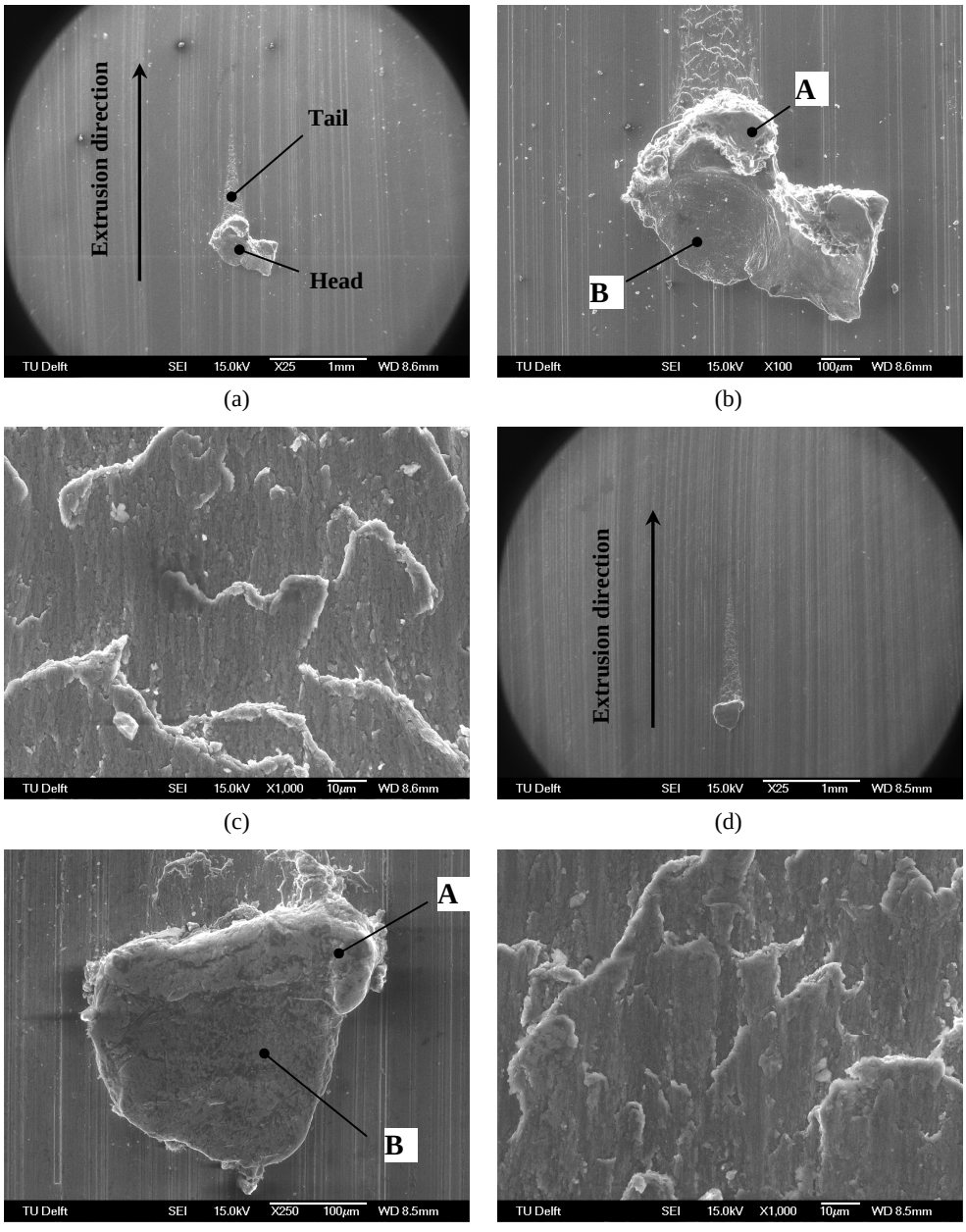

Fig. 5.1 Typical outlook of surface pickups found on extruded AA 6063 products: (a) outlook of pickup 1; (b) the “lump” of pickup 1; (c) the “tail” of pickup 1; (d) outlook of pickup 2; (e) the “lump” of pickup 2; (f) the “tail” of pickup 2.

It can be seen in Fig. 5.1 (a) and (d) that characteristics of the outlook of pickups are quite evident: it contains a fleck of material deposit and a torn region. The overall appearance resembles a comet, therefore the fleck is analogously termed the "head", and the torn region is referred to as the "tail" in this thesis. The tail points to the extrusion direction, and the head is deposited at the "far" side of the whole pickup. The observed geometry conforms to existing knowledge [1] [57]. However, it has been observed there are a lot of "tails" visible on the extrudate surface without the "head". This will be discussed later.

The head represents some interesting features: it does not have a uniform height. A plateau-like high part presents at the tail side of the head, indicated as location A in (b) and (e). The plateau is fairly flat, and has traces of wear. Location B is lower than the plateau, and forms the remaining part of the head. The shape of this kind suggests that the head has been subjected to severe bending before being deposited on the extrudate surface. This bending may be due to the friction stress inside the bearing channel, as explained later. Indeed, location A shows traces of wear.

It has been found in [57] that the head has a multi-layer structure, which is formed "through a number of discrete events". The layered structure has also been confirmed by observation, as shown in Fig. 5.2.

It can be clearly seen that layers are deposited on one another. The layer thickness is of the order of 1 μm. The shape of the layers shows that they have undergone severe plastic deformation. Therefore, formation of pickup is a successive and accumulative process.

The tail shows a lot of tensile cracks, as shown in Fig. 5.1 (c) and (f). This suggests that there is intensive material transfer — thus repeatedly attaching and detaching taking place in the torn region. The width of the tail region gradually decreases towards the extrusion direction. The topography resembles the pattern found in the groove in scratch test [80], where the cracking is caused by tensile stresses created at the rear part of the abrading slider.

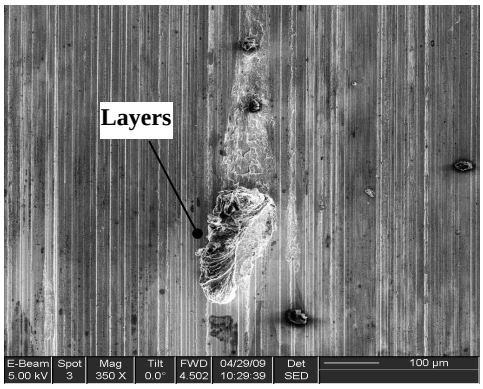

(a)

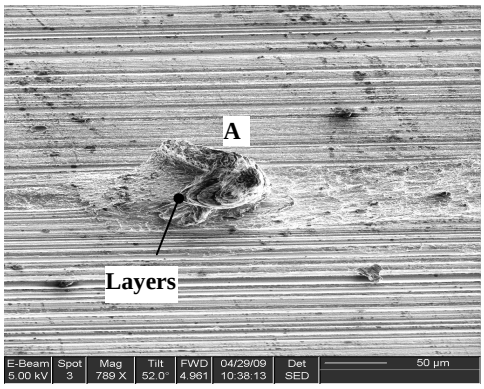

(b)

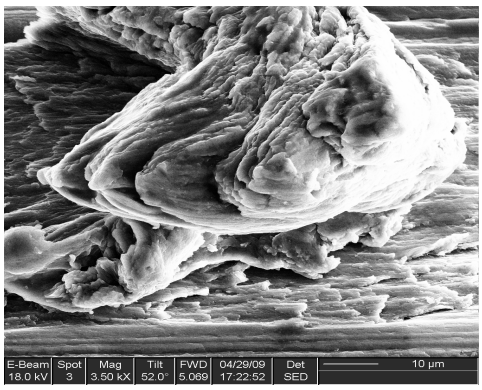

(c)

Fig. 5.2 Layered appearance of the pickup head: (a) layers on pickup 3; (b) layers on pickup 4; (c) location A on pickup 4, clearly showing that the head is made from layers of material.

5.1.2 Dimensional characteristics of surface pickups

The detailed geometrical information was obtained by LSCM, revealing the 3–D structure and dimensional characteristics of a pickup, as shown in Fig. 5.3:

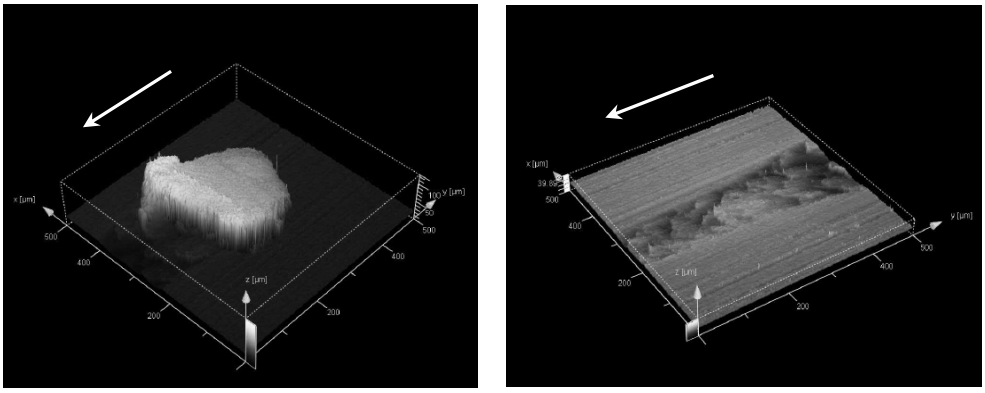

(a) (b)

Fig. 5.3 LSCM images of pickup 1: (a) the head; (b) the tail. White arrows indicate extrusion direction.

From measurements it can be concluded that the width of the head is generally 100 ~ 200 μm; the height of the plateau is 30 ~ 140 μm and the height of the low part of the head is generally below 30 μm. The tail has been seen as a groove with a depth of approximately 5 μm. Therefore, the direction of material transfer in the tail is probably from the torn region on the extrudate to the pickup head. Two scenarios are possible:

- Scenario 1: the groove is formed when the bearing asperities plough through the extrudate surface, and the plastically deformed material displaced by the asperities from the groove accumulates to form the head.
- Scenario 2: the head is not only formed by displaced material from the groove but by some other mechanism, meaning the head is formed earlier than the groove. When the head moves on the extrudate surface after it is formed, material from the extrudate transfers to the head due to strong adhesion, leaving the groove.

The difference between the two scenarios is whether the material that forms the head comes entirely from the removed material from the groove, which would be scenario 1. In this case, as no material has been observed to have been displaced to the sides of the groove, the volume of the head should have been equal to that of the groove. The values have been calculated according to LSCM measurements on a number of pickups, and the conclusions are quite consistent: the volume of the head is approximately one order larger than the removed material from the groove. This is solid proof that the head is not made of material displaced from the groove.

The implications are that the head has only been formed before the tail is formed; the removed material from the tail probably contributes to the total volume of the head, but is only a small fraction.

5.2 Microstructure analysis

The next step was to obtain microstructure information in order to understand the deformation history of the pickups. Case study of pickup 4 in Fig. 5.2 is presented in this section. FIB was used to cross section to reveal the microstructure. Two series of cross sectioning have been made, as schematically shown in Fig. 5.4:

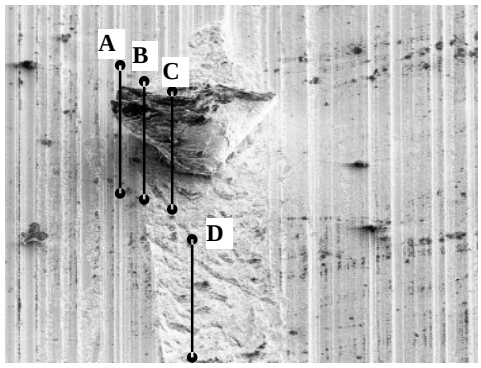

Fig. 5.4 Cross – sectioning procedure for pickup 4.

Sections A, B and C were made on the pickup head to examine its microstructure, and section D for examining the tail. Since the FIB will produce a hole along the intended section, it also reveals details at the interface between the head and the extrudate. The morphology at these four sectioning locations is shown in Fig. 5.5:

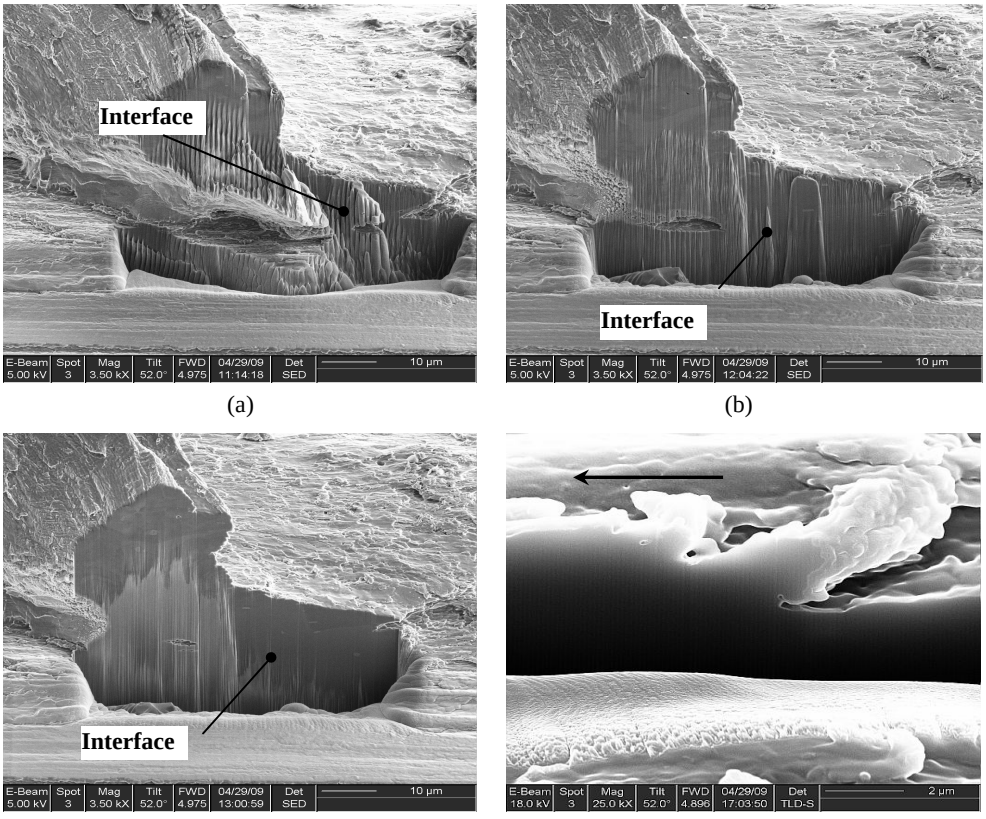

Fig. 5.5 Cross section pictures: (a) sectioning A; (b) sectioning B; (c) sectioning C; (c) sectioning D. Arrow indicates direction to the pickup head.

The column-like structure at the cross section was created during cutting by FIB. It can be seen that there is a gap between the head and the extrudate, which vanishes towards the centre of the head (from A to C). The width of the tail conforms to location B. Other than the gap, no traces of any cracking can be found on the head–extrudate interface, suggesting that a strong bonding is formed between the head and the extrudate surface due to material transfer. In Fig. 5.5 (d) it can be seen that the material has been torn in the direction of the pickup head. Cracks generally penetrate only 1 ~ 2 µm into the extrudate surface. The direction of the torn layers is consistent with the findings that material from the tail transfers to the pickup head.

The samples were etched to enable microstructure study, shown in Fig. 5.6 (a). It

can be observed that the microstructure does not correspond to the outside layered aspect of the pickup head. The grains are mostly equi-axed — suggesting that the microstructure was recrystallised after severe plastic deformation. The average grain size has been calculated as a function of the distance from the plateau of the head, as shown in Fig. 5.6 (b). In the plateau, the grain size is roughly 5 μm whereas in the low part of the head it is around 15 μm. On the extrudate surface the grains are a little bigger, around 20 μm. It is clear that the grain size is significantly reduced in the plateau. This shows that the plateau has been subjected to more plastic deformation than the low part of the head, therefore nucleation rate for recrystallisation is much higher due to granular defects formed in deformation. This corresponds to the shape of the plateau, which seems to have been bent as a result of shear force in the bearing channel.

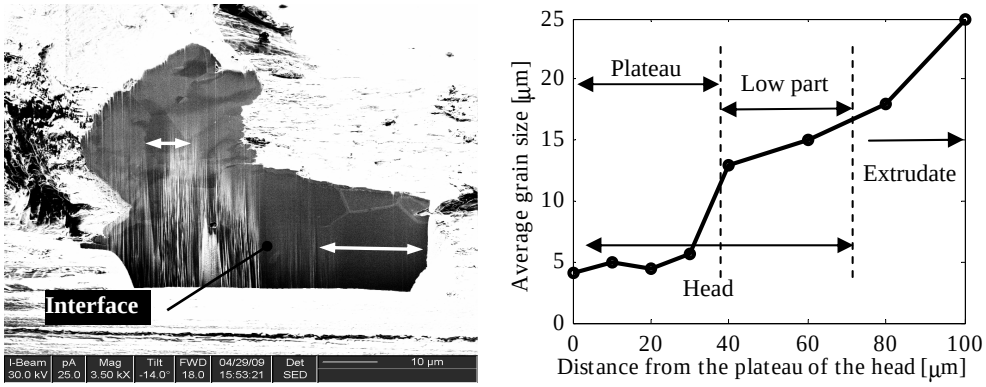

(a) (b)

Fig. 5.6 Microstructure showing recrystallised structure: (a) sectioning C; (b) Average grain size along the depth of the extrudate surface.

5.3 Composition analysis

The chemical composition analysis was carried out by EDX, on section C and D. Bright second phase particles were observed on section C, so EDX was performed on both the matrix and the second phase particles. Results are shown below:

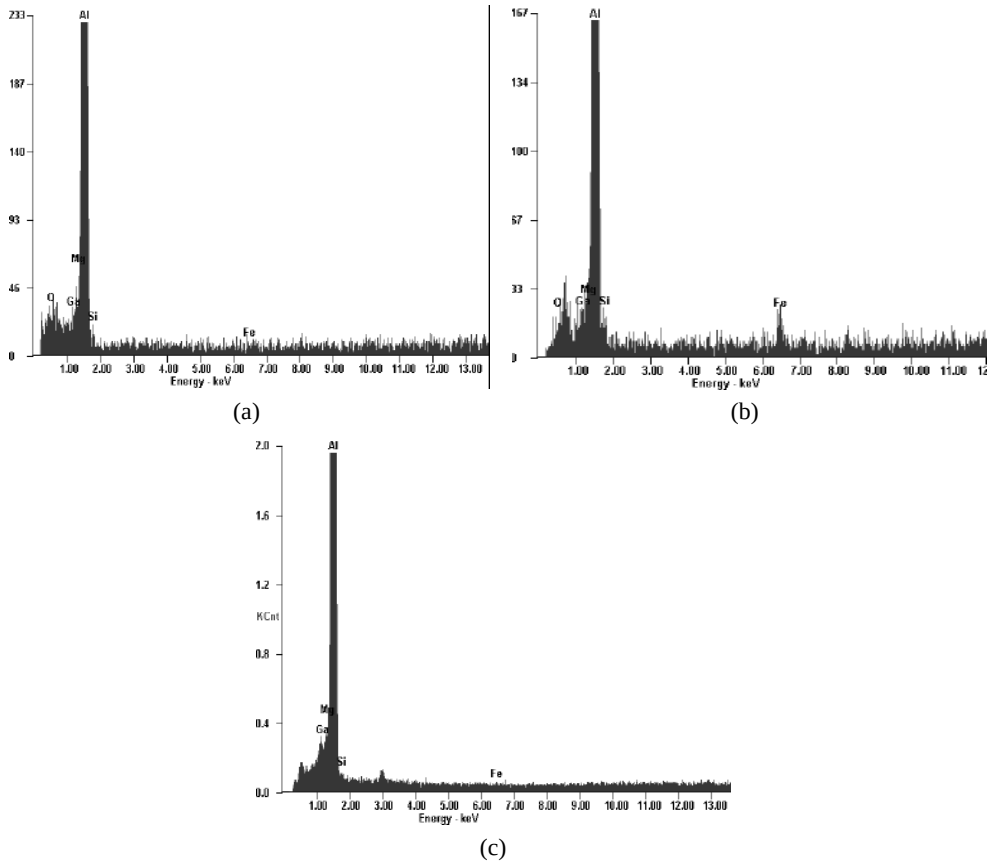

Fig. 5.7 EDX analysis of chemical composition: (a) Matrix on section C; (b) Second phase particle on section C; (c) Matrix on section D.

Apparently, EDX analysis of the matrix on section D gives us information of the bulk extrudate material, as shown in Fig. 5.7 (c). (a) shows that the matrix on section C, i.e., the pickup head, is also made of aluminium. This proves that the pickup head did come from the extrudate material. There is a significant amount of oxygen observed in the head rather than the tail, but apparently this cannot lead to the conclusion that the pickup head is made of Al or Mg oxides, as opposed to some literature [81]. The observed oxygen on section C is probably due to oxidation of the surface of the layers during formation, which became the inner matrix after the successive deposition of layers. (b) suggests that the bright second phase particles are plate-shaped AlFeSi intermetallics. In a nutshell, the pickup head is made of the extrudate material — aluminium alloy, with partial oxidation during its formation.

5.4 Discussion

This section serves to summarise our findings and observations, and clear the logic behind proposing a formation mechanism.

Characterisation of pickups has been performed to understand their origin by examining their geometry, microstructure and composition, and the results are very informative. A typical pickup resembles a comet. It contains a lump of material called the “head”, a torn region trailing from the head called the “tail”. The head has a high part and a low part. The general shape of a pickup can be schematically illustrated below:

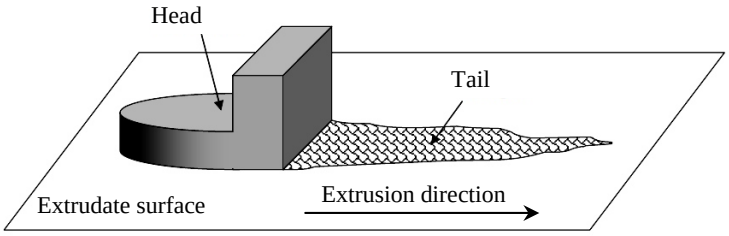

Fig. 5.8 Schematic illustration of a typical pickup found on extruded AA 6063 products [79].

The outside aspect of the pickup head suggests that the head has been bent to show a plateau-like high part. Therefore, the high part was severely deformed during formation of a pickup, which has been justified by the small equi-axed, recrystallised grains, as shown in Fig. 5.6. The top part of the high part is flat and indicates wear, suggesting that the bending results from large friction inside the bearing channel (Fig. 5.1 (b) and (e)).

SEM pictures of the tail clearly show a torn region where tensile failure dominates (Fig. 5.1(b) (f) and Fig. 5.5 (d)). The tensile stress is due to large adhesion between the head and the tail, much like when a slider grades a soft material in a scratch test. Tensile cracking suggests constant material transfer between the head and the tail. Volume analysis of the tail and the head clearly indicates that material transfer is from the tail to the head, but the contribution is minor. These indicate that the head had already been formed before the tail was produced. The tail (torn region) was formed due to large adhesion between the head and the tail and hence the tensile stress created while the head ploughs through the surface of the extrudate.

An important feature of the pickup head is that it is made of multilayers, although

the microstructure could not be matched due to recrystallisation. The layered structure suggests that the head is formed successively by the gradual addition of material. EDX analysis of the head indicates oxygen at the inside of the head, hinting that the inner core of the head was once exposed to the outside environment, as the layers were gradually deposited on one another. This shows that the head is probably initiated on the bearing.

Compositional studies reveal to us that the pickup head is made of material from the extrudate, which contains some second phase particles such as AlFeSi intermetallics. Therefore, the formation of pickup is heavily related to the process of material transfer between the bearing and the extrudate. The transfer proceeds from the extrudate to the bearing, and then from the bearing to the extrudate, leaving a pickup.

As mentioned before, there are a lot of “tails” without a “head”. This occurs when the transferred pickup head on the extrudate surface attaches again to the bearing, leaving only a torn region without the head.

5.5 Proposed formation mechanism for surface defects

Based on the above observations and conclusions, a formation mechanism for pickup, and thus for surface defects, is proposed. The formation process is presented below in Fig. 5.9, and can be categorised chronologically into four stages. An important parameter that varies in the formation process is the separation between the original bearing surface and the extrudate surface h, which is in fact the “space” for pickups with a height of several tens of microns to form.

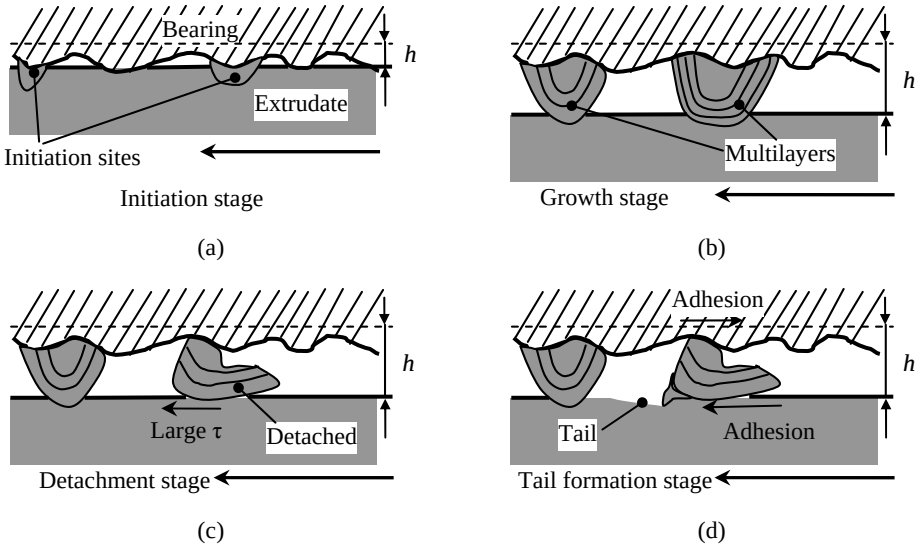

Fig. 5.9 Proposed formation mechanism for surface defects: (a) initiation stage; (b) growth stage; (c) detach stage; (c) deposition stage. Arrows at the bottom right corner indicate extrusion direction.

- Initiation stage (Fig. 5.9 (a)): as discussed above, pickup formation is initiated in the slipping zone on the bearing surface — as a result of material transfer to the bearing surface due to large adhesion between steel and aluminium at elevated temperatures. The initiation sites are mostly the irregularities on the bearing surface, for example, contact patches operating in the wedge–formation regime introduced in Section 2.1.2.3 [10]. In the initiation stage, the separation between the bearing surface and the extrudate surface is in the order of the roughness of the bearing, namely, several microns.

- Growth stage (Fig. 5.9 (b)): as the extrudate keeps exiting the bearing, the initiation sites (called “lumps” hereafter) will grow as material transfer continues. The material is added successively to the lump, forming a multilayer structure. The deformed material is recrystallised (either dynamic or static recrystallisation), eliminating the anisotropic microstructure. The surface of the lump is oxidised quite fast, which is then deposited with another layer of material. Therefore oxygen can be detected in the inside of the pickup head. During the growth stage, since lumps have different characteristics and will grow differently, it is possible that some lumps initially in contact will not be out of contact. The lumps can get to the size of about 100 μm by coalescence; in order to keep the contact area constant (nominal contact pressure remains

unchanged), the separation h is increased to approximately the height of the lumps (~ 30 μm).

- Detachment stage (Fig. 5.9 (c)): the lumps keep growing, and they acquire an increased aspect ratio (height / width). At some point the large friction between the lump and the moving extrudate creates a tilting moment (clockwise in our illustration) that detaches the lump from the bearing. The top part of the lump is still in contact with the bearing surface, which tends to bend it clockwise. The separation h in this stage remains close to the height of the lumps.

- Tail formation stage (Fig. 5.9 (d)): the detached lumps are then stuck inside the bearing channel, and the top and bottom parts of the lump are still in contact with the bearing and the extrudate surfaces, respectively. The resistance from the bearing will restrain the lump from moving together with the bearing, leaving a torn mark on the extrudate (the tail). During this period, three possibilities can be operating:

  - The lump is deposited on the extrudate surface thus forming a torn region with a head, i.e., a pickup.
  - The lump is deposited back on the bearing surface, leaving a torn region without a head. The lump can move again from the bearing to the extrudate, etc.
  - The lump becomes a loose particle inside the bearing channel.

  In the first case, lumps form detrimental pickups; in the second case they leave torn marks on the extrudate surface and increase bearing roughness. Because of their shape they are likely to be transferred again to the extrudate surface; in the third case, deep scratches will be produced that increase extrudate surface roughness. Therefore, the total amount of detached lumps is a good indicator of the surface quality of aluminium extrusion products, as they serve as the total available material to form surface defects. This will form the fundamentals for the physical model.

5.6 Summary

In this chapter a formation mechanism for surface pickups is proposed, based on a detailed study of the appearance, microstructure and composition of pickups. From

the study it is clear that pickups come from the extrudate material, and are crucially related to material transfer between the bearing and extrudate surfaces. This material transfer process will be analysed and modelled in Chapter 6.

Chapter 6
Modelling formation of surface defects on aluminium extrusion products

The fundamentals of the model have been discussed in Chapter 5. In this chapter, a physical model is presented to model the formation of surface defects on aluminium extrusion products. It has been established that the number of detached lumps is a good indicator for the extrusion product surface quality, and this serves as the foundation for the physical model. By combining the physical model and the FEA of the extrusion process that provides mechanical and thermal information, a surface quality predictor can be developed. In this way, the process parameters (extrusion temperature and exit speed) and die geometry (bearing length, bearing angle and surface roughness) can be tailored to optimise surface quality of extrusion products. This chapter will focus on two nominally flat surfaces in contact, which corresponds to a certain location on the bearing. The surface quality predictor, taking into account the entire bearing, will be discussed in Chapter 7.

6.1 Overview of the model

The physical model described in this chapter calculates formation of surface defects from a measured surface topography dataset, a given temperature and sliding speed, and a nominal contact pressure, which represent the local tribological conditions, shown as below:

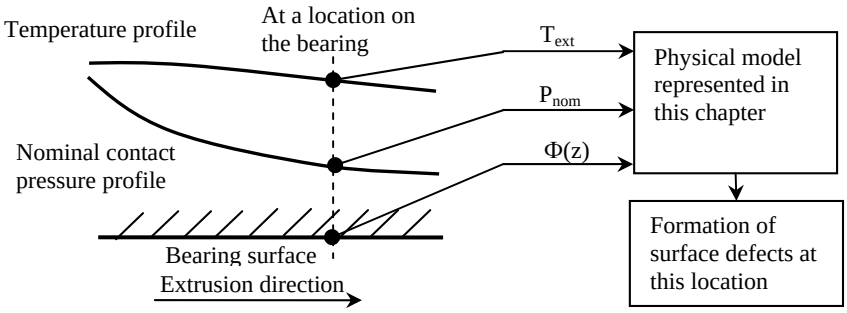

Fig. 6.1 Scope of the physical model.

Pressure, temperature profiles along the whole bearing length are not considered in this thesis. A notation custom is revisited here: local contacts not covered by aluminium are called “contact patches”, otherwise they are called “lumps”. In the very beginning of the growth process all the contacts are contact patches, whereas some may grow into lumps if aluminium is transferred onto them. Based on the previous chapter, the formation consists of several stages. Our physical model has been developed in line with the proposed formation mechanism. As has been discussed, the formation is an accumulative and successive process which evolves with process time. Therefore the physical model has been developed in such a way that it evolves with cycles instead of real world time. In each cycle the stages advance until a lump is large enough to detach. The calculation scheme of the physical model is illustrated below:

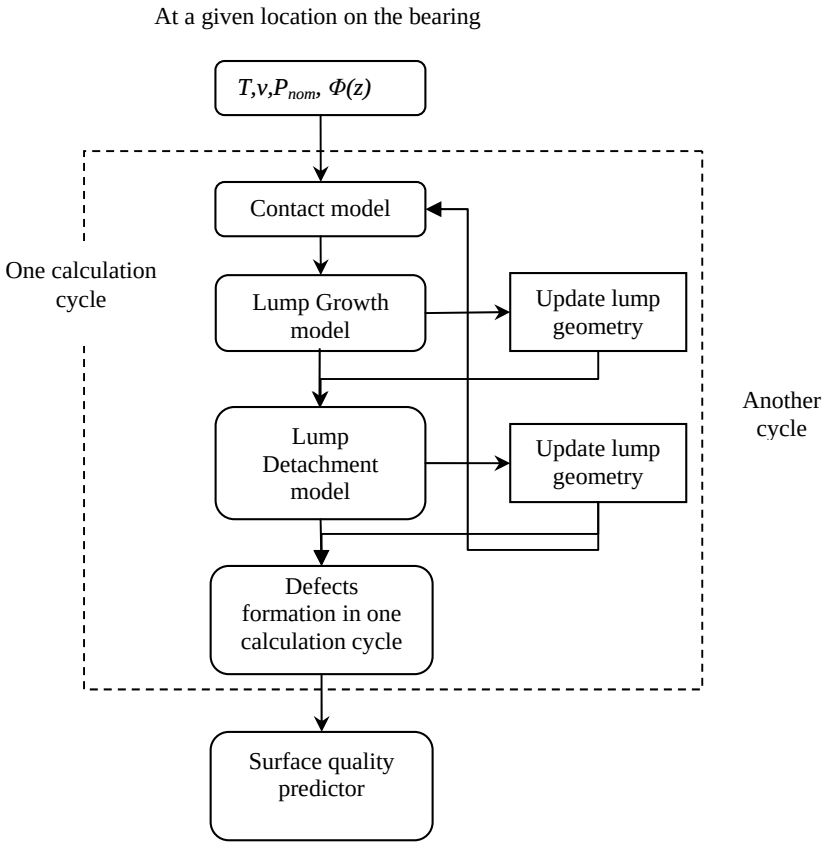

Fig. 6.2 Calculation scheme of the physical model.

The physical model is compiled based on the proposed formation mechanism, so

that lumps initiate, grow and finally detach. Lump update 1 involves replacing grown lumps' geometry with a calculated new geometry; Lump update 2 removes the detached lumps from the calculation and replaces them with the original bearing surface geometry. For the first calculation cycle, the growth model is responsible for the initiation stage of the surface defect formation process. The input values used in the calculations can be summarised in Table 6-1:

Table 6-1 Values of input parameters.

Input parameter	Unit	Values	
		Reference	Varied values
Surface roughness[1] R_q	[μm]	1	2, 0.5
Extrudate surface temperature T_{ext}	[ºC]	557	497, 517, 537, 577
Exit speed (sliding speed) v_{ext}	[m/s]	0.085	Fixed value
Degree of contact[2] α	[–]	35%	0.3%, 8.7%, 17%, 48%, 60%, 70%

In the following sections, each model will be presented together with calculation results.

6.1.1 The contact model

The contact model solves the separation h between the bearing and extrudate surfaces, given a certain applied nominal contact pressure. It is based on the fully plastic contact model presented in Chapter 3. In order to account for the changing bearing surface microgeometry due to material transfer from the extrudate, the contact module transforms an engineering surface into a set of contact patches, which will then grow or evolve according to some pattern discussed in the next section. Several aspects are characteristics for the contact model:

- The contact area is the summation of contact area of contact patches and lumps in contact; therefore the input surface height dataset is only considered in the first calculation cycle. After this, the calculation is continued using contact

[1] The same numerically generated surfaces used in Chapter 3 have been used in here.
[2] Degree of contact is a better indicator than nominal contact pressure, as the latter is in turn affected by temperature and speed.

patch and lump geometry.

- Growth of the lumps will change the bearing surface topography, therefore the surface separation will depend on how all the lumps have grown in the previous cycles, which is obtained from the growth model.

- The detached lumps will restore to the geometry of their corresponding original bearing surface contact patches in the contact model. Therefore, it is assumed that the detached material is removed out of the tribological system and does not carry load.

It can be shown that separation increases as the lump growth process proceeds. Since each lump grows differently, it is possible as the separation is enlarged, some lump that was initially in contact may later become out of contact.

6.1.2 The lump growth model

So far the only quantitative model about material transfer during sliding contact was developed by de Rooij [38], in which the plastically deformed material was considered to be the cause of "lump growth" that determined lifetime of the tool. Following Challen & Oxley's slip–line approach [37], it was assumed that only asperities operating in the wedge–formation regime resulted in wear of the softer material, and a fraction of that worn material will contribute to the material transfer process. In conjunction with experimental work, it was validated that:

- Material transfer initiates preferably at the protruding parts of the surface. They are surface "extrema" (heights and / or slopes).
- Lumps tend to grow in height.

In the current study, the fundamentals of material transfer remain unchanged, therefore the extrudate material is assumed to be transferred to contact patches (or lumps) that operate in the wedge–formation regime.

6.1.2.1 Initiation stage

The initiation stage is very crucial. As material transfer is initiated, the f_{hk} value locally will be unity (aluminium against aluminium), therefore subsequent material transfer will always prevail. Whether a contact patch operates in the wedge –

formation regime and can initiate lump growth depends on the interfacial shear factor f_{hk} and the attack angle, as shown in Fig. 6.3:

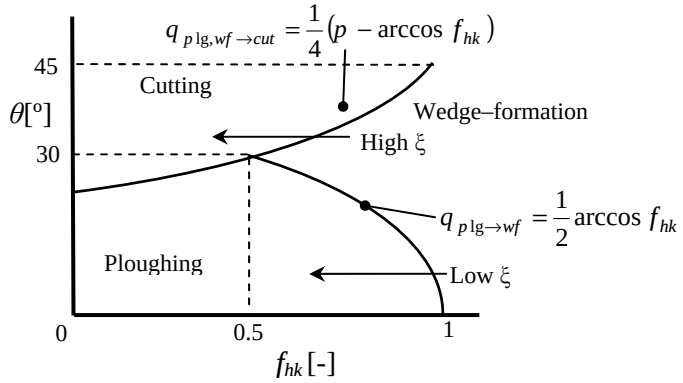

Fig. 6.3 Wear mode diagram: three different regimes illustrated schematically.

It can be seen that when the f_{hk} is smaller than 0.5, there is no lump growth possible. When it is larger than 0.5, the possibility for material transfer is increased. Therefore, factors influencing f_{hk} such as temperature and sliding speed can affect the initiation process. As the attack angle is load-dependent, the nominal contact pressure can also affect the initiation. Temperature, sliding speed, nominal contact pressure and surface topography can all affect initiation. A degree of initiation D_{ini} can be defined as the ratio between area of initiation and the nominal contact area. It is thus essential to evaluate this D_{ini} with varied f_{hk}, p_n and R_q values, as this determines how lumps will grow to form pickups.

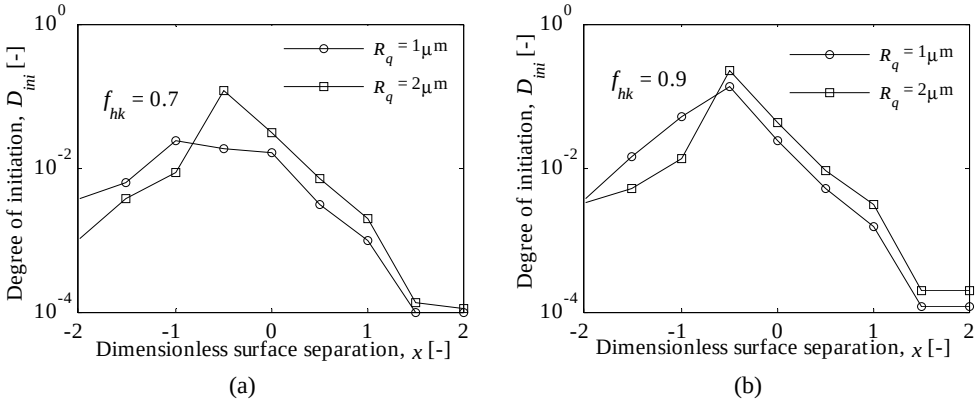

Fig. 6.4 Material transfer initiation on numerically generated surfaces (see Table 3-1 for surface parameters): (a) f_{hk} = 0.7; (b) f_{hk} = 0.9.

It can be seen that f_{hk}, p_n and R_q values affect how much material transfer will be initiated on a rough surface, the degree of initiation D_{ini}. The nominal contact pressure has a considerable (dominant) effect due to:

- It changes the real contact area. At high separation values (low p_n) the real contact area is small, therefore D_{ini} is also at a low level, which increases when the separation decreases;
- It changes the geometry of the contact patches as seen in section 3.2.3.

This leads to a reduction of initiation at very high p_n values as the contact patches are generally so blunt that they operate in the ploughing regime, as shown in Fig. 6.3. This is to say, a low to medium pressure level is conducive for material transfer initiation. The effect of f_{hk} affects initiation as shown in the wear mode diagram — a larger f_{hk} will enlarge the initiation sites.

Surface roughness also plays a role, which is though non-monotonic: at low pressure levels increasing roughness will increase D_{ini}, opposed to reducing it at high pressure levels. The above observations can be illustrated in the wear mode diagram again, where the range of attack angles of lumps is marked, as shown in Fig. 6.5.

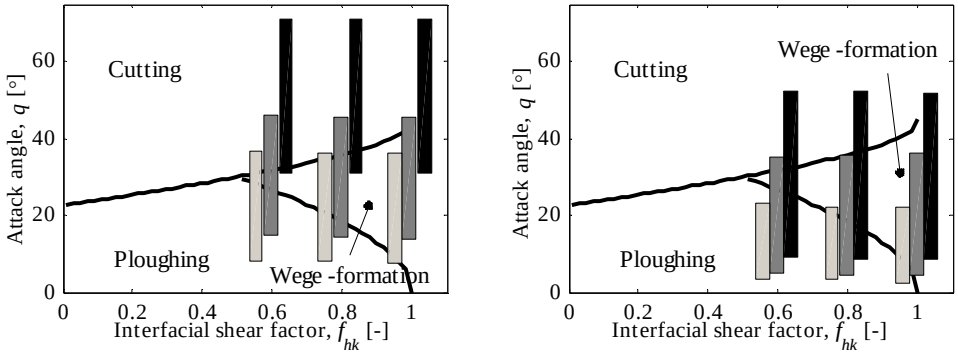

Fig. 6.5 Wear – mode diagram and range of attack angle measured from bearing surfaces: (a) at low nominal contact pressure values ξ = 1; (b) at high nominal contact pressure values ξ = -1.
R_q = 2 μm; R_q = 1 μm; R_q = 0.5 μm.

The attack angles of lumps at low nominal contact pressure values are larger than

at high pressure levels; therefore at low nominal contact pressure values, the rough surface that increases values of attack angle will tend to move the lumps from the wedge–formation regime to the cutting regime, reducing material transfer; at high pressure values it will shift into the wedge–formation regime from the ploughing regime. A smooth surface though, will tend to move the lumps into the ploughing regime in both cases.

6.1.2.2 Growth stage: volume transferred

Once material transfer is initiated at a contact patch on the bearing surface, the local f_{hk} value will be unity. Practically, this means that the initiation sites will be very likely to attract more transferred material, according to Fig. 6.3. For a contact patch with an effective attack angle θ_{eff}, the wear rate of aluminium can be written as [37]:

$$\text{Wear rate} = \frac{\text{unit distance volume loss}}{\text{normal load } F_n} = \frac{1}{2k}\frac{\sin^2 q_{eff} + \frac{1}{2}\sin\left(2q_{eff}\right)}{1+\sin\left(2q_{eff}\right)} \tag{6.1}$$

Therefore, the volume loss over a certain sliding distance l can be obtained:

$$\mathrm{V}(l) = \frac{1}{2k}\frac{\sin^2 q_{eff} + \frac{1}{2}\sin\left(2q_{eff}\right)}{1+\sin\left(2q_{eff}\right)} A_{cp} H l \tag{6.2}$$

If the sliding distance l is considered to be the distance travelled by the existing extrudate during one calculation cycle, referred to as the “cycle distance”, the volume loss during a cycle can then be related to this cycle distance:

$$\mathrm{V}_{cycle} = V(l) \tag{6.3}$$

Since it is important to study the formation of defects over a fixed length on the extruded profile (defect density), the cycle distance should also be constantly given a fixed cycle number, regardless of the exit velocity. Therefore the cycle distance l does not include the exit velocity term; rather, it is merely a magnification factor that determines how much material will be worn during one cycle.

On top of that, in reality only a fraction of the worn material will be transferred, depending on the intrinsic adhesion between the counter surfaces. This fraction also serves as a magnification factor. Therefore, it is convenient to replace the cycle distance with:

$$l = m_a F_{adh} \tag{6.4}$$

In which m_a has a unit of [m/N]. This m_a factor is only a magnification factor that can be chosen arbitrarily, only to adjust the amount of material transferred by a particular lump in one calculation cycle. The adhesion force F_{adh} for fully plastic contact can be obtained by following Chowdhury's approach [82], where the unloading period as defined in the classical JKR adhesion model had been neglected. According to this model, the adhesion for an elliptical paraboloidal indenter is a function of the effective lump tip radius and the interfacial work of adhesion:

$$F_a = p b_{eff} \Delta g = \frac{p a_{mj} a_{mn}}{2w} \Delta g \tag{6.5}$$

The interfacial work of adhesion between two contacting metallic surfaces can be related to the mutual solubility of two metallic materials [83]:

$$\Delta g = \begin{cases} 2g_{al} & \text{Aluminium – aluminium contact} \\ 0.5\left(g_{al} + g_{fe}\right) & \text{Aluminium – bearing contact} \end{cases} \tag{6.6}$$

In which the coefficient 0.5 is an approximation for fully compatible metals. Now substituting $H = 2.8\sqrt{3}k$ and combining expressions for the adhesion force, the volume of transferred material during one calculation cycle can be rewritten into:

$$V_{cycle} = m_a \Delta g A_{cp} G = \frac{2.8\sqrt{3} m_a \Delta g p^2 a_{mj}^2 a_{mn}^2}{8w} \frac{\sin^2 q_{eff} + \frac{1}{2}\sin\left(2q_{eff}\right)}{1 + \sin\left(2q_{eff}\right)} \tag{6.7}$$

Where G is purely a geometrical factor of the lump, with a unit of [m]. Eq. 6.7

shows that the amount of material transferred per unit area during one calculation cycle is only a function of the geometry of the lump, the interfacial work of adhesion and the magnification factor. The geometrical factor can be multiplicatively decomposed into an adhesive part G_{adh} and an abrasive part G_{abr} as:

$$G_{adh} = b_{eff}; \quad G_{abr} = \frac{\sin^2 q_{eff} + \frac{1}{2}\sin(2q_{eff})}{1+\sin(2q_{eff})} \tag{6.8}$$

This geometrical factor G and its decomposed components can be shown as a function of the effective tip radius:

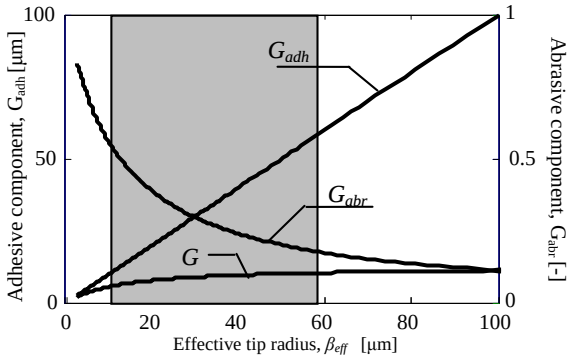

Fig. 6.6 Influence of the effective tip radius of a lump on the geometrical factor (volume transferred per unit area). Grey area indicates practical range of effective tip radius in our study, based on measured bearing surfaces.

Fig. 6.6 shows that the adhesive component of the geometrical factor is proportional to the effective tip radius as a result of intrinsic adhesion; however, the abrasive part decreases substantially with the tip radius, due to lower attack angle when tip radius is large and thus less amount of plastically deformed material. The net result is a mild increase of the geometrical factor (thus amount of material transferred per unit area) as a function of tip radius in the practical range in our study.

6.1.2.3 Growth stage: geometry change of the growing lump

The transferred material is deposited on the growing lumps. In [10] it was assumed

and later observed that most of the lumps would grow in height. This is due to 1) surface separation is increased during growth process; 2) at the operating temperature for sheet metal forming (below 300 °C), aluminium is work hardenable. Therefore the lumps made from deformed material are much harder than the work piece, and hence they can grow very high to form sharp shapes without shearing. However, at extrusion temperature well above 300 °C, aluminium cannot be work hardened, but rather, strain rate sensitive. Therefore the assumption that lumps only grow in height is untrue in the case of aluminium extrusion since that would mean that they could grow to a very sharp shape, which would probably be sheared as the materials on both sides of the contact are of roughly equal hardness. Kayaba et al. determined that once the attack angle of a ploughing asperity exceeded some critical value, the asperity itself would plastically deform and fail [84]. This critical attack angle is a function of the interfacial shear factor f_{hk} and the hardness ratio between the counter surfaces, as shown in Fig. 6.7:

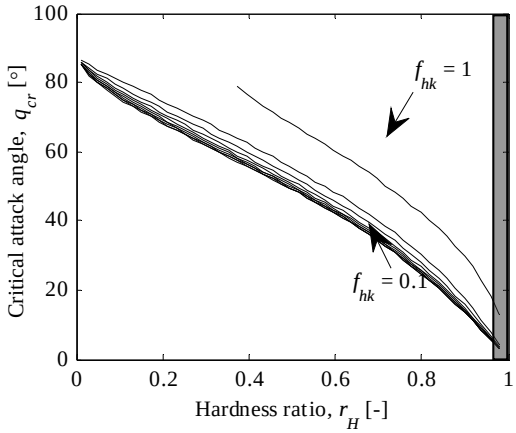

Fig. 6.7 Critical attack angle as a function of r_H and f_{hk}. Grey area indicates the hardness ratio in aluminium extrusion process.

To obtain the hardness ratio r_H, the temperature of the lump and that of the extrudate surface has to be known. A temperature drop across the interface can be shown in Fig. 6.8:

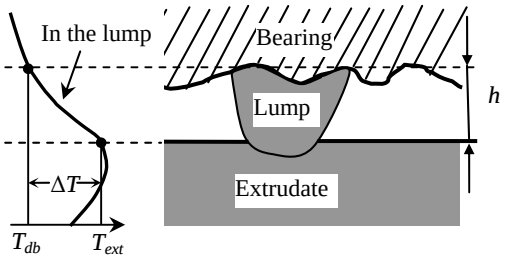

Fig. 6.8 Temperature distribution across the interface and inside the lump.

The representative lump temperature is taken as an average of the bearing and extrudate surface temperatures. The temperature difference between the extrudate and bearing surfaces $\Delta T = T_{ext} - T_{db}$ results from a thermal contact conductance, which is much smaller than the conductivity of steel. If the die outer surface is maintained at the billet temperature as a usual industrial practice and no cooling of the die is implemented, this thermal contact conductance h_{tcc} results in a temperature drop across the interface[1] [64]:

$$\Delta T = T_{ext} - \frac{h_{tcc} T_{ext} + 2K_{fe} T_{bil} / \ln(2R_{db}/t)t}{2K_{fe} / \ln(2R_{db}/t)t + h_{tcc}} \tag{6.9}$$

Where T_{bil} = 750 K is the standard billet temperature, T_{bil} = 780 K is the extrudate surface temperature, K_{fe} = 15 W/(Km) is the thermal conductivity of tool steel, R_{db} = 15 mm and t = 2 mm are the radius of the die and the wall thickness of the profile. Eq. 6.9 is a weak function of R_{db}, t, and billet temperature T_{bil} but a strong function of $T_{ext} - T_{bil}$. The thermal contact conductance is of the form [85]:

$$h_{tcc} = c_1 K^* \frac{s^*}{s^*} \left(\frac{p_n}{H} \right)^{c_2} \tag{6.10}$$

Where K^* is the combined thermal conductivity of the contacting surfaces, σ^* and s^* are combined surface roughness and absolute mean surface slope. However the coefficients c_1 and c_2 obtained from the literature are only valid for $p_n/H < 0.03$. Therefore, an effective value of h_{tcc} of $1.1 \cdot 10^4$ W/(Km^2) of aluminium – steel interface is used throughout the study (including FEA to calibrate a temperature

[1] This equation only considers radial thermal conduction in steady state situation.

reading from thermocouples)[86]. This gives a ΔT of 10 ºC, which is used as an invariant in this study.

The hardness ratio r_H can now be written as:

$$r_H = \frac{H_{ext}}{H_{lump}} = \frac{s\left(T_{ext}, \dot{\varepsilon}\right)}{s\left(T_{ext} - \frac{\Delta T}{2}, \dot{\varepsilon}\right)} \tag{6.11}$$

Given an r_H value approaching unity, it can be readily shown by the above analysis that the critical attack angle at aluminium–bearing interface in aluminium extrusion is quite small — in the order of 10º, shown as the grey area in Fig. 6.7. Therefore, the assumption adopted in this thesis is that lumps first grow in height until the attack angle reaches this critical value; the increased volume in this case is denoted as ΔV_{cr} and the height δ_{cr}. Then the lump will grow in width to maintain the critical attack angle so it will not shear under the application of a friction force. The transferred material is assumed to cover the entire surface area of the contact part of the lump instead of only the frontal area, under the condition of the friction stress [10]. Three growth patterns can be categorised:

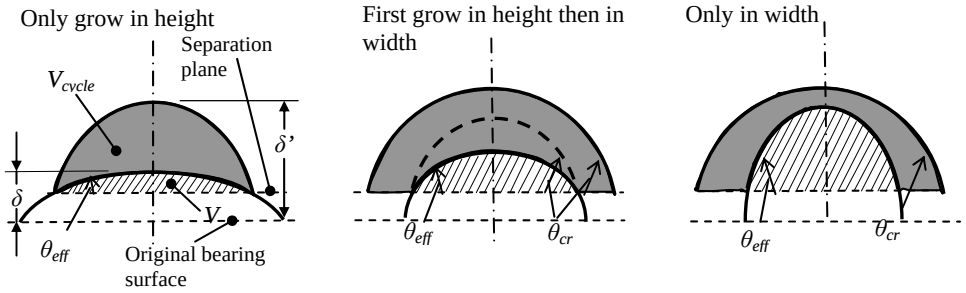

Fig. 6.9 Growth patterns for lumps with different attack angle: (a) the lump only grows in height; (b) the lump first grows in height then in width; (c) the lump only grows in width. Grey areas indicate the transferred material during one calculation cycle. Striped areas indicate the original lump before the calculation cycle.

- $\theta < \theta_{cr}$, $V_{cycle} < \Delta V_{cr}$

The lump only grows in height, as shown in Fig. 6.9 (a). In this case, the contact

radius will not change, but a new height of the lump can be expressed as:

$$d' = d + 2\frac{\left(V + V_{cycle}\right)}{p a_{mj} a_{mn}} - w \tag{6.12}$$

In which V stands for the volume of the lump in contact (above separation plane) before material transfer. δ' is the height of the lump after transfer and ω is the original indentation depth before growth.

- $\theta < \theta_{cr}$, $V_{cycle} > \Delta V_{cr}$

The lump first grows in height then in width. In this case, the lump increases its lateral dimension. Suppose the increased major contact radius length can be given by $a_{mj}' = ca_{mj,}$ the contact radius and new lump height can be expressed as:

$$c = \sqrt[3]{\frac{V + V_{cycle}}{V + \Delta V_{cr}}}; \qquad d' = d - w + \left(d_{cr} - d + w\right)\sqrt[3]{\frac{V + V_{cycle}}{V + \Delta V_{cr}}} \tag{6.13}$$

- $\theta >= \theta_{cr}$

The lump directly grows in width and increases its lateral dimension. In this case the original attack angle is larger than the critical value so material will attach to the side to maintain the critical attack angle. Together with the previous scenario, the lump will grow both in height and width. This might result in a mushroom-like shape of the grown lump, as shown in Fig. 6.9 (b) and (c), which seems to fit the layered outside aspect of the pickup heads. The geometry of the new lump can be defined:

$$c = \sqrt[3]{\frac{2\left(V + V_{cycle}\right)}{p a_{mj} a_{mn} w}\frac{\tan q}{\tan q_{cr}}}; \; d' = d + w\left(\sqrt[3]{\frac{2\left(V + V_{cycle}\right)}{p a_{mj} a_{mn} w}\left(\frac{\tan q_{cr}}{\tan q}\right)^2} - 1\right) \tag{6.14}$$

It can be seen that the geometry of the lump after material transfer is proportional to the volume of transferred material in one calculation cycle V_{cycle}, which is controlled by the magnification factor m_a. This magnification factor does not change the characteristics of the growing process but only serves as an indicator of how the growing process is refined into each calculation cycle.

As the lumps grow and separation is increased, the multilayered lump does not possess the geometry of a paraboloid anymore. The attack angle θ is taken as an effective value by considering the equivalent height, likewise with Eq. 3.10:

$$w = 2V/pa_{mj}a_{mn} \tag{6.15}$$

The effective attack angle is obtained according to Eq. 3.13. However, the contact volume V and contact radius a_{mj} of a multilayered lump at any separation can only be precisely obtained by extracting geometrical information for each "layer". For this purpose, the geometry of each layer calculated from Eq. 6.12, 6.13 and 6.14 is stored, from which the effective attack angle θ_{eff} and contact radius can be obtained for each cycle.

On top of the change of geometry of each individual lump, lump coalescence is inevitable as lumps grow both in height and width. As in our fully plastic contact model, neglecting this coalescence process leads to an erroneous result as lumps cannot grow in width anymore when they "meet" another lump. An algorithm is made that lumps interfering with others will be detected and treated as a single lump with the same contact area and volume, likewise is done in the fully plastic contact model.

6.1.3 Detachment model

As lumps grow higher and bigger, the large friction between the lump and the extrudate creates a tilting moment that detaches the lump from the bearing. As the lump always has an attack angle not larger than the critical attack angle, the detachment is assumed to always occur at the lump–bearing interface. Fig. 6.10 shows schematically the loading condition for a lump.

A lump is constantly subject to a transverse friction force and a vertical force resulting from plastically indenting the soft material. The loading condition can be characterised by the degree of indentation D_i, the degree of contact radius D_c, and the aspect ratio defined as:

$$D_i = w/d\ ; \qquad D_c = a/a_{lump}\ ; \qquad r_{asp} = d/a_{lump} \tag{6.16}$$

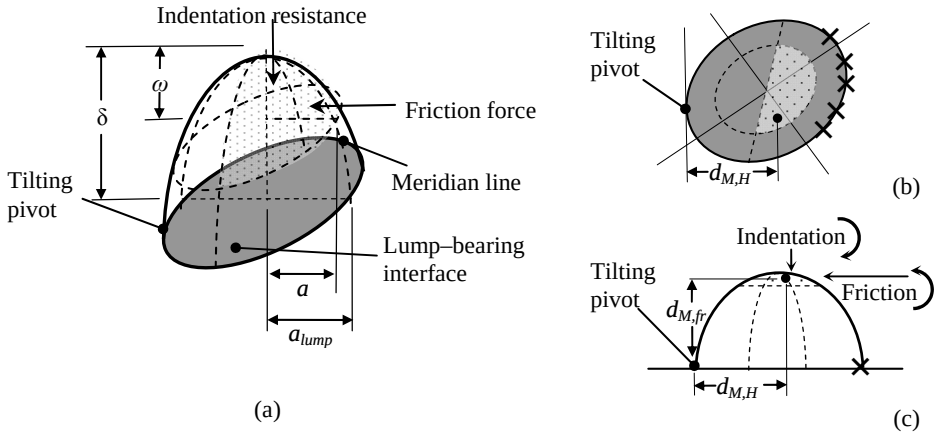

Fig. 6.10 Loading condition of a lump: (a) iso-view; (b) top-view showing the tilting pivot and calculation of lateral distance *d*; (c) front-view showing components of the tilting moment. Cross marks indicate failure initiation sites. Grey area indicates the bearing–lump interface.

The lump has a tendency to tilt around its pivot, depending on the tilting moment. The pivot is the leftmost point at the interface, as marked in the figure. The total tilting moment is supported by the counter clockwise moment of friction, and opposed by the clockwise moment of the indentation force. For the detachment to occur, a dual criterion has been implemented:

- Since the lump has been sitting on the bearing surface for a while, a metallurgical bonding has formed at the interface. Therefore, the first criterion is that the interface between the lump and the bearing has to fail. Failure needs to initiate at the free edge at the lump–bearing interface, as marked by cross marks in Fig. 6.10 (b) and (c).
- To form the bent shape the lump has to tilt under the loading condition so that the interfacial failure can propagate (the interface continues to fail).

6.1.3.1 Interfacial failure

For the interfacial failure, a strength-based approach censoring the stresses at the free edge has been used. A quadratic failure criterion is implemented since both normal and shear stresses are present at the interface [87] [88]:

$$\begin{cases} \left(\frac{s_n}{s_{cr}}\right)^2 + \left(\frac{t_{xz}^{\ 2} + t_{yz}^{\ 2}}{t_{cr}^{\ 2}}\right) = 1 \\ s_n > 0 \end{cases} \tag{6.17}$$

In which x,y are in-plane coordinates and z points to the vertical direction. The first item in the quadratic failure criterion states that some critical stress values need to be reached; the second implies that a positive normal stress (thus tensile) at the free edge is a prerequisite for failure criterion [88]. The critical stresses are properties of the interface. Szeto et al. [89], by performing button shear test, found that between two adhesive surfaces τ_{cr} is much larger than σ_{cr} due to the mechanical interlocking effect of surface roughness. Therefore, in our study, the critical value for shear τ_{cr} is considered to be equal to the shear strength of the lump. It has been found in our particular case, the exact value of σ_{cr} is of minor importance as in most cases when the normal stress is positive, the shear stress itself already exceeds τ_{cr}. The critical values are prescribed as: $\tau_{cr} = k$; $\sigma_{cr} = 0.5k$ in this study according to findings from Szeto [89].

FEA has been utilised to obtain an accurate stress distribution along the lump–bearing interface. The geometry of the lump is input in FEM package Comsol®'s elasto – plastic structural mechanics module. Boundary conditions are set exactly as the actual loading conditions and the mesh size at "dangerous locations" such as free edges and boundaries is refined until no further change in stress is observed[1]. After calculation the resolved stress values at the lump – bearing interface are examined by the quadratic criterion to determine failure initiation.

It has been found by parametric study that failure initiation is influenced by the loading condition (D_i and D_c) and the aspect ratio of the lump defined in Eq. 6.16. As the loading condition is changed, the stress distribution on the lump–bearing interface also changes, leading to different failure initiation. An example of this involves the change of loading condition as a lump grows, therefore both the degree of indentation and degree of contact radius change. The purpose is to see if a prescribed coefficient of friction (μ = 1) can initiate failure by our quadratic failure criterion, when the loading conditions are changed on the same lump.

[1] For purely elastic analysis the magnitude of stress on these "dangerous locations" will increase and not level off when mesh size is reduced since singularity exists at the free edges. For elasto–plastic analysis this singularity is absent.

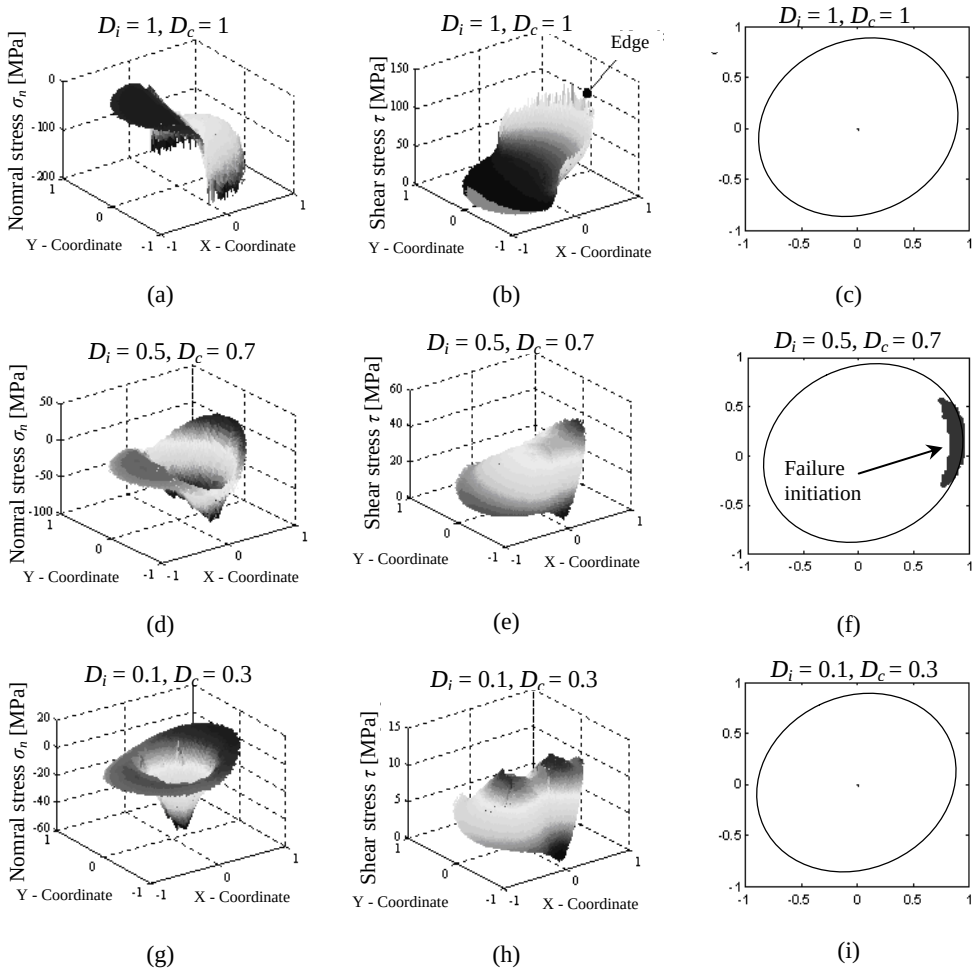

Fig. 6.11 Interfacial failure when loading condition is changed. Note: the stress scales are different.

It can be seen that when contact area covers the entire frontal area as seen in Fig. 6.11(a) to (c), shear stress at the free edge is very large. However, the normal stress remains largely compressive therefore failure initiation cannot occur (as shown in (c)). As the degree of indentation and degree of contact radius decreases, the normal stress at the free edge is tensile, in this case failure can initiate at the free edge. When the loading area keeps shrinking the stress is too little to fulfil the quadratic criterion, and maximum shear stress shifts from the free edge towards the centre of the lump–bearing interface. Therefore no initiation can take place. The

above analysis suggests that under each combination of loading condition and geometry of the lump, a critical coefficient of friction exits, above which failure is guaranteed to initiate. This critical coefficient of friction $\mu_{int,cr}$ can be shown to be influenced by D_i, D_c and r_{asp} :

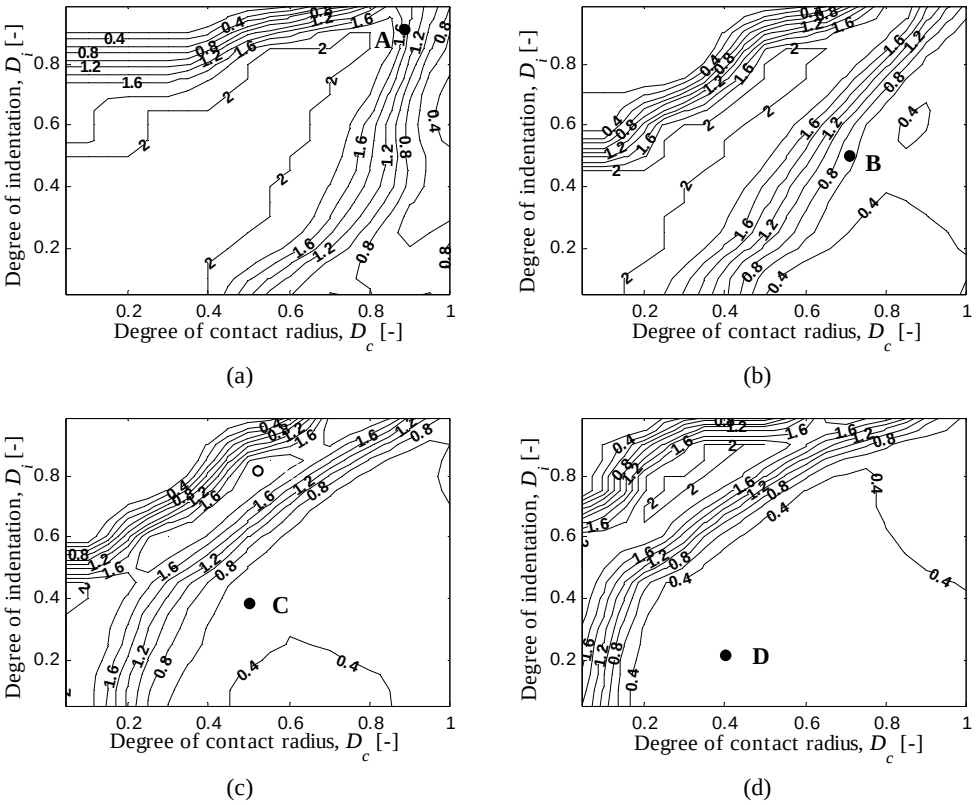

Fig. 6.12 Critical coefficient of friction for interfacial failure: (a) r_{asp} = 0.1; (b) r_{asp} = 0.5; (c) r_{asp} = 1; (d) r_{asp} = 2.

The critical coefficient of friction for interfacial failure depends a lot on the geometry of the lump itself. It can be seen clearly that the critical coefficient of friction decreases significantly as the aspect ratio of the lump increases — as the lump grows. The top left corner features lumps with extremely sharp tip (high degree of indentation with low degree of contact radius) which is rare for real lumps, therefore the extremely low critical friction is less than meaningful. The real lump growth will commence at A in Fig. 6.12 (a) where both D_i and D_c are close to unity. In this case the critical coefficient of friction is around 1.4. As the lump

grows to point B in (b), D_i decreases much more than D_c due to geometry of the lump, and the critical value drops to 0.6. As the lump keeps growing, the critical value continues to drop. This illustrates that during the growth phase of a lump, interfacial failure becomes progressively likely to occur.

6.1.3.2 Lump tilting

In order for a lump to detach, only interfacial failure is not enough. It has been assumed in this study that a lump which is only sheared off from the tool will not appear as a pickup on the extrudate. The total moment for lump tilting consists of the tilting moment from friction force M_{fr} and the opposing moment from indentation M_H (effect of gravity is not considered). If the lump were rigid, the entire lump would be just about to tilt when M_H is equal to $M_{fr,}$. However, the lump itself can deform during this tilting process, therefore to what extent the lump has to tilt in order for a pickup to form is unknown, which is a function of the deformation characteristics of the lump and mutual adhesion with the bearing (thus the bearing–lump material combination). For the study of lump detachment in a single tribological system, it is logical to assume that the second criterion in the dual criterion requires that the ratio between M_{fr} and M_H (thus called "dimensionless tilting moment" hereafter) be above some critical value $r_{M,cr}$.

The moments of friction force and indentation resistance can be obtained by integrating over the entire contact area. This yields:

$$M_{fr} = mH \iint_{contact} d_{M,fr}(x,y))\mathrm{dxdy} \tag{6.18}$$

$$M_H = H \iint_{contact} d_{M,H}(x,y))\mathrm{dxdy} \tag{6.19}$$

$$r_M = \frac{M_{fr}}{M_H} \geq r_{M,cr} \tag{6.20}$$

In which the lengths $d_{M,fr}$ and $d_{M,H}$ are schematically shown in Fig. 6.10 (b) and (c). They are only a function of the lump geometry, which is updated after each cycle of growth. The dimensionless tilting moment r_M is a function of the loading condition, geometry of the lump and obviously the coefficient of friction. Since the effect of coefficient of friction is linear, only the effects of other factors are presented in Fig. 6.13 (a) (for a prescribed coefficient of friction μ = 1). Similarly, the critical coefficient of friction for lump tilting $\mu_{tilt,cr}$ can be shown as a function

of the loading condition with $r_{M,cr}$ taken as unity:

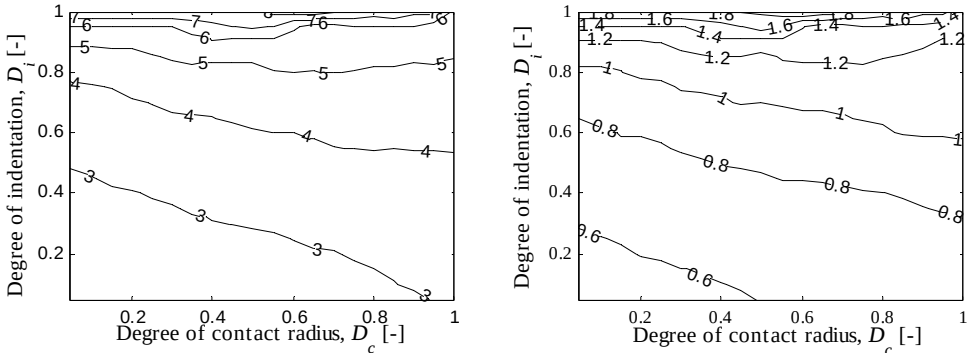

Fig. 6.13 Critical coefficient of friction for lump tilting failure: (a) r_{asp} = 0.5; (b) r_{asp} = 1.

It can be seen that the shape of the lump is crucial to tilting failure. Apparently sharp lumps with large aspect ratios have large dimensionless tilting moments and tend to tilt easily. Equally important is the fact that as the degree of indentation decreases, the dimensionless tilting moment increases. This shows that if a lump only grows in height, as the indentation in this case will not change, the lump will be difficult to tilt. On the other hand, if a lump grows both in height and in width, as the lump grows bigger, the degree of indentation decreases and this lump becomes increasingly easier to tilt. Lumps that are most likely to tilt are sharp lumps loaded at only a fraction of their frontal area.

6.1.3.3 Detachment of lumps

To formulate the dual failure criterion, the coefficient of friction calculated by Challen & Oxley's model [37][1] is compared with the critical values of coefficient of friction from the dual criterion. A lump will detach if:

$$m(q, f_{hk}) \geq \max\left(m_{\text{int},cr}, m_{tilt,cr}\right) \tag{6.21}$$

Whether a lump will detach can also be shown as related to D_i, D_c and r_{asp}, as a "detach diagram".

[1] Calculation was performed for f_{hk} = 0.95 to account for aluminium – aluminium contact.

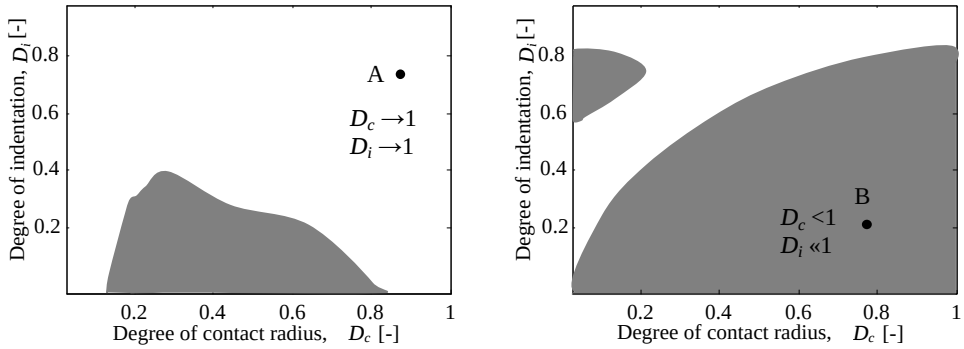

Fig. 6.14 The detach diagram as a function of D_i, D_c, r_{asp} : (a) r_{asp} = 0.5; (b) r_{asp} = 1. Grey area indicates detached lumps.

It can be seen that amongst the geometrical factors, the aspect ratio has the most profound effect – sharp lumps with large aspect ratios tend to detach more easily. At lower aspect ratio values (Fig. 6.14 (a)), detached lumps are only loaded at the top part (small D_i value); at higher aspect ratio values detachment will occur at a wide range of D_i and D_c. Regarding the lump growth process, this suggests that a lump will grow most likely until a certain aspect ratio is reached, when detachment will follow. The growth of a lump will initiate at point A in Fig. 6.14 (a) where D_c and D_i are both close to unity. This is unlikely to trigger detachment. As the lump grows, D_i will considerably decrease while D_c decreases only moderately due to constant load, at point B shown in Fig. 6.14 (b). This suggests that lump detachment only occurs after certain growth.

The dimensionless tilting moment can be chosen arbitrarily; however, a larger value requires a lump to reach a higher aspect ratio. The dimensionless tilting moment can be obtained by performing lab – scale extrusion experiments and measuring pickup geometry.

6.2 Results and discussion

It is worthwhile at this stage to revisit the fact that calculations shown in this thesis do not give an exact number of surface defects, but only the material available for their formation. It is for this reason that the term “detached lumps” is used in this chapter.

The input parameters for calculations have been shown in Table 6-1 and other important parameters adopted in the model are listed below:

Table 6-2 Input parameters for calculations.

Parameters	Unit	Value
Magnification factor, m_a	[m/N]	$2.8 \cdot 10^{-2}$
Free surface energy of aluminium γ_{al}	[N/m]	0.8 [90]
Free surface energy of iron γ_{fe}	[N/m]	2.4 [90]
Dimensionless tilting moment $r_{M,\,cr}$	[–]	1
Bearing–extrudate temperature difference $\Delta T = T_{ext} - T_{db}$	[°C]	10
Calculation cycle number N	[–]	100

The number of calculation cycles N has been selected as relatively large, as a small amount of calculation cycles yielded unstable results. The magnification factor has been chosen accordingly to give a reasonable calculation time. The dimensionless tilting moment has been proved to yield detached lumps with aspect ratios conforming to experiments.

6.2.1 Typical growth pattern of a bearing surface

The evolution of a bearing surface with material transfer from the extrudate can be illustrated by the surface separation. As lumps grow in width, the separation is increased gradually. The typical growth pattern of a bearing surface can be visualised as follows:

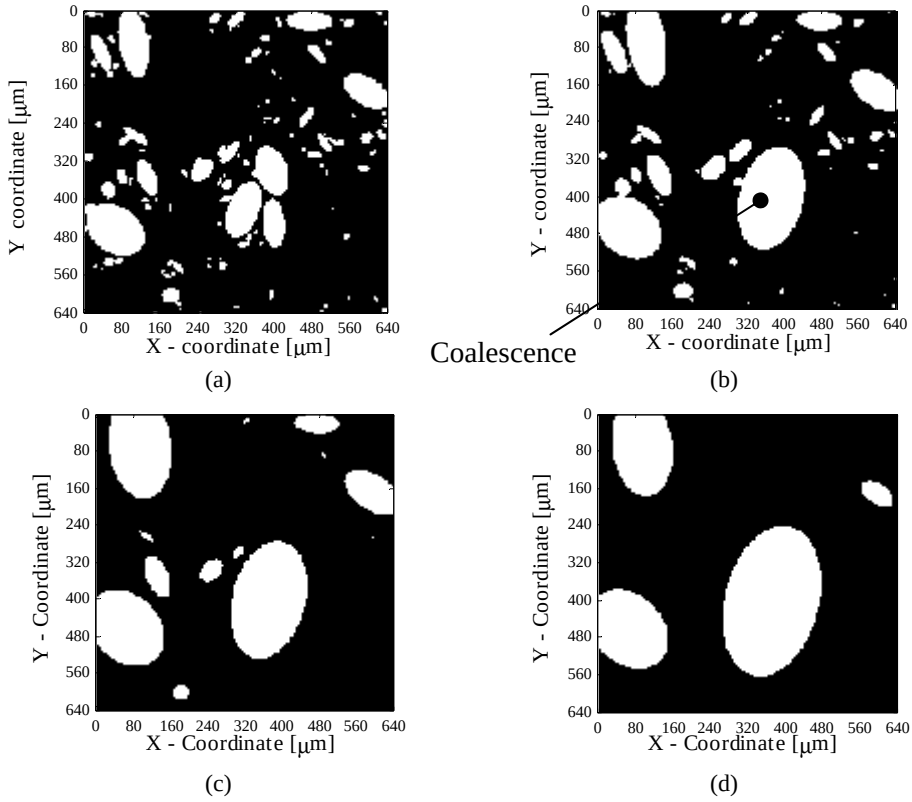

Fig. 6.15 Typical growth pattern of material transfer.

It can be seen that as the material transfer process proceeds, several events occur:

- Lumps get bigger due to material transfer, as from Fig. 6.15 (a) to (b);
- Adjacent lumps coalesce to form a composite lump, which will replace individual small lumps in the subsequent calculation cycles, for example from Fig. 6.15 (a) to (b); The coalesced composite lump takes the contact area equal to the summation of that of individual lumps;
- Small lumps grow slower, therefore some lumps that were initially in contact are not in contact in later stages, as from Fig. 6.15 (b) to (c) and to (d);
- Due to constant growing of lumps, the number of lumps in contact (available for pickup formation) is decreased, and the separation between the original bearing surface and the extrudate surface is increased to the order of the height of a pickup (~ 10 μm).

Separation elevation can be defined as the difference between calculated separation at a certain calculation cycle and initial separation (without material transfer). The separation elevation and number of detached lumps after 30 calculation cycles can be shown in the following curves to indicate the evolution of a growth process:

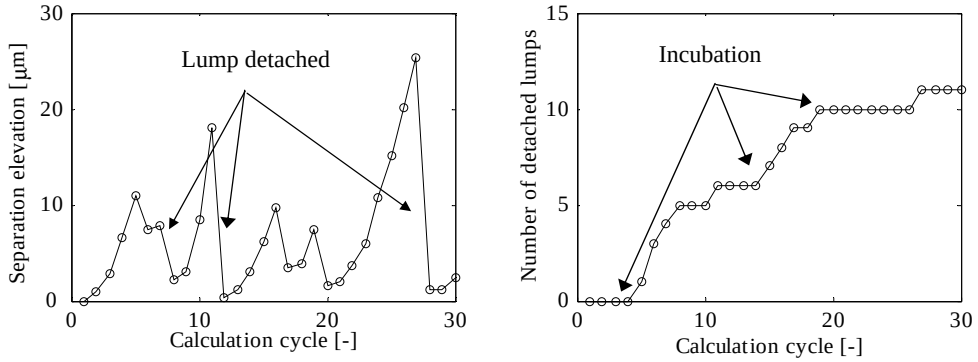

(a) (b)

Fig. 6.16 Evolution of separation and total number of detached lumps during 30 calculation cycles.

It shows in Fig. 6.16 (a) that the separation between the original bearing surface and the extrudate surface is increased due to lump growth until it reaches a critical height of pickups in the order of 10 μm, followed by detachment of lumps. Since one or more lumps fail at this point, the available bearing area at the high separation level is decreased, requiring the separation to drop to a lower level. This incurs a periodic change of the surface separation. The decreasing phases of the separation (as marked in Fig. 6.16 (a)) correspond to detachment of lumps in Fig. 6.16 (b), whilst the increasing phases indicate the growth stage of lumps. Macroscopically, these manifest themselves as “incubation” periods where no pickups are formed. The length of the “incubation” periods varies with input surface topography due to the deterministic nature of the model, therefore a calculation cycle number of 100 has been chosen in all calculations to decrease the variation; here the number of detached lumps at the end of 30 cycles is shown to give a reasonable length of the “incubation periods”.

6.2.2 Influence of process parameters

In this section calculations were performed using the reference surface with a roughness of 1 μm.

In terms of process parameters that are of significance to this study, the input pressure (the nominal contact pressure), temperature (extrudate surface temperature) and sliding speed (exit speed) are the most important factors. In Chapter 3 it has been established that extrudate temperature and exit speed have similar effects — high temperature and / or exit speed lead to a reduction of f_{hk}; thus in this section, the exit speed is fixed at 0.085 m/s with merely the temperature varied. A by-product of varying the temperature is the change of hardness of the material, which in turn alters the degree of contact. Therefore, the degree of contact α has been varied according to prescribed values instead of nominal contact pressure; the consequence of this is that the nominal contact pressure is different for different temperature inputs. Fig. 6.17 (a) shows the total number of detached lumps at the end of 100 cycles as a function of the extrudate surface temperature; Fig. 6.17 (b) shows the effect of degree of initiation D_{ini}:

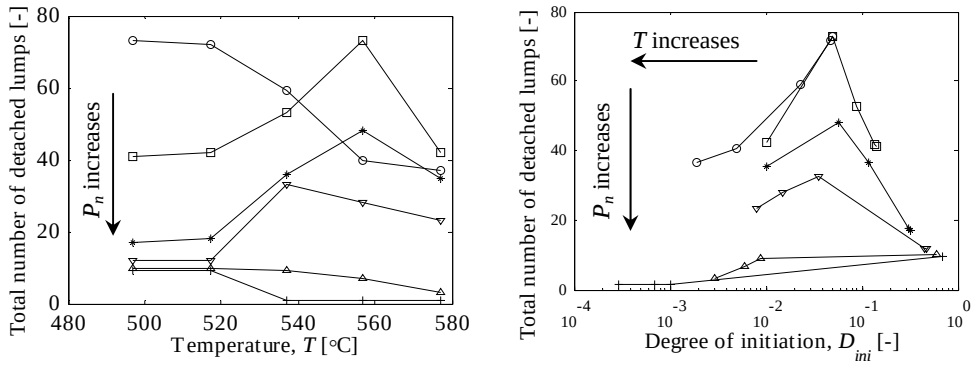

Fig. 6.17 Number of detached lumps formed as a function of process parameters. Different curves were obtained using varied degree of contact (nominal contact pressure): ○ α = 9%; □ α = 17%; ∗ α = 35%; ▽ α = 49%; Δ α = 60%; + α = 70%.

It should be noted that temperature and speed do not contribute to the amount of material transferred during each calculation (the growth model), and they are also certainly not influential in the detachment model. Therefore, temperature and speed influence detached lump formation by changing the value of f_{hk}, which governs the initiation of material transfer; once material transfer is initiated, the associated f_{hk} is not critical anymore since subsequent f_{hk} will be equal to unity. It is then more meaningful to plot the number of detached lumps as a function of the degree of contact α and the degree of initiation D_{ini}, as shown in Fig. 6.17 (b). The corresponding D_{ini} values are shown in Fig. 6.18.

What can be studied is that as the temperature increases, the f_{hk} value decreases, and this leads to a drastic change in the degree of initiation, depending on the degree of contact. When p_n is large, there is an abrupt change of D_{ini} from almost full to zero initiation; when it is small, the transition takes place in a much wider temperature range. Overall, between 510 ~ 550 ºC initiation is varied significantly, leading to a considerable change in formation of detached lumps, as can be seen in Fig. 6.17 (a). From Fig. 6.17 (b) the implications are clear. The general conclusion is that as p_n increases, the number of detached lumps is reduced substantially due to lump coalescence. This conforms to the findings by Parson [57] that there is a complete absence of pickup formation on profiles extruded with fully choked dies, i.e. a high pressure.

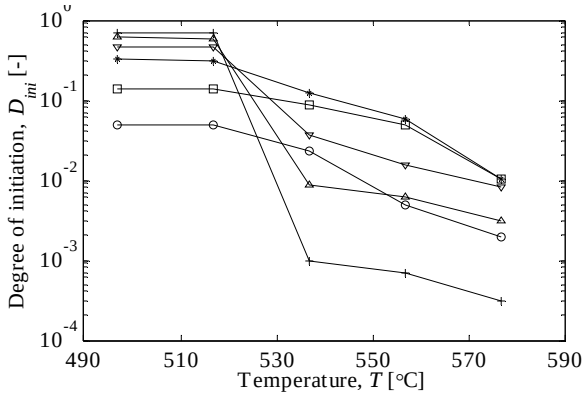

Fig. 6.18 Degree of initiation as a function of temperature and degree of contact: ○ α = 9%; □ α = 17%; ∗ α = 35%; ▽ α = 49%; Δ α = 60%; + α = 70% .

The growth process depends on the degree of initiation D_{ini} according to the following control mechanisms:

- When initiation spots are close to each other as in the case of large D_{ini}, it is likely that a lot of lumps will coalesce to form big lumps. This is referred to as the “coalescence controlled mechanism”.
- When initiation spots are far apart from each other as in the case of small D_{ini}, the initiation spots are more likely to grow “on their own”, forming multiple but smaller lumps. In this case the time by which these individual lumps grow to a critical size determines how many detached lumps will form. This is termed the “growth controlled mechanism”.

It can be seen in Fig. 6.17 (b) that as the temperature is increased (D_{ini} decreased),

the formation of detached lump is first coalescence controlled, where large D_{ini} promotes coalescence and decreases the number of detached lumps. As D_{ini} is decreased furthermore, coalescence becomes less prominent and the growth controlled mechanism dominates. In this case large D_{ini} reduces the time required for a lump to grow to the critical size and increases the number of detached lumps. The two control mechanisms interplay and form a "dangerous zone" in particular favour of detached lump formation, as shown in Fig. 6.19:

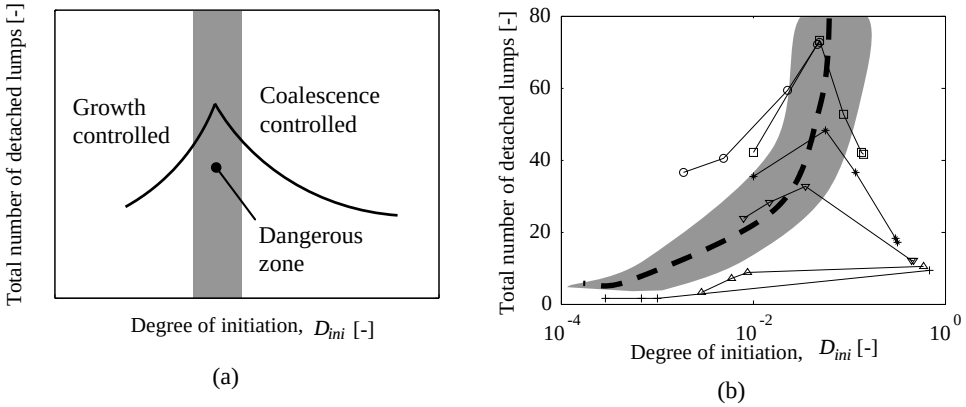

Fig. 6.19 Two control mechanisms form a "dangerous zone" in particular favour of detached lump formation: (a) schematic; (b) calculations. ○ α = 9%; □ α = 17%; ∗ α = 35%; ▽ α = 49%; Δ α = 60%; + α = 70% .

In addition, since these two control mechanisms are also influenced by the degree of contact α, the dangerous zone as shown in Fig. 6.19 (b) is not located at the same D_{ini} value. A small degree of contact will not be conducive to coalescence anyway as the final size of lumps is limited by the degree of contact. Therefore, the dangerous zone occurs at low values of D_{ini} for large values of degree of contact. The ambiguity exists at curves with high α values, for example, the curves for α = 60% and 70% in Fig. 6.17 (b). In these cases the initiation spots will keep growing until they coalesce to one or two very large lumps, therefore it is more suitable to identify them as "growth controlled". Shifting away to both ends will impede the formation process.

The conclusions regarding the above considerations can be clearly visualised in Fig. 6.17 (a):

- The number of detached lumps decreases remarkably with increasing nominal contact pressure (increasing α).
- At small α values (low nominal contact pressures α < 10%), coalescence is insignificant and the process is growth controlled. Therefore the number of detached lumps is reduced at high temperatures.
- At small to medium α values (10% < α < 50%), the number of detached lumps first increases to a peak value, and then decreases, as temperature is elevated.
- At large α values the number of detached lumps decreases with increasing temperature.

As Fig. 6.17 (b) contains characteristics of the growth process, it is called the "growth diagram". In subsequent sections it will be discussed whether this diagram is prone to change as a result of variation in other factors such as surface topography.

6.2.3 Influence of roughness of the bearing

In this section the effect of bearing surface roughness is studied by using the previously numerically generated surfaces with different roughness values of 0.5, 1 and 2 μm, with temperature and speed settings unchanged. Again, the associated "growth diagram" is studied.

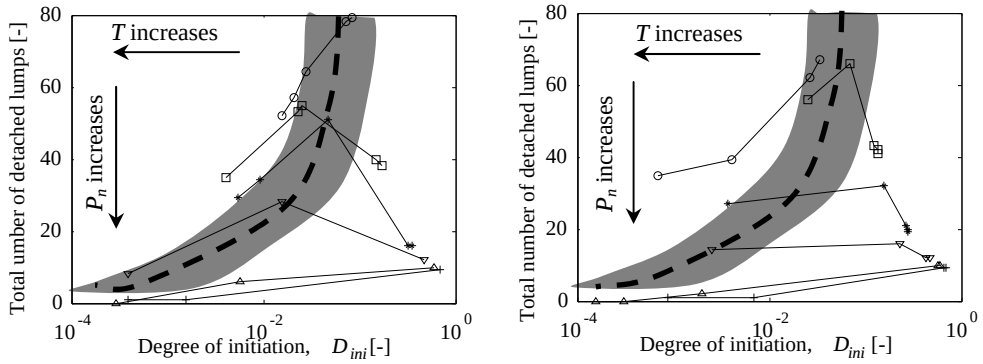

Fig. 6.20 Effect of surface roughness on the number of detached lumps: (a) R_q = 0.5 μm; (b) R_q = 2 μm. ○ α = 9%; □ α = 17%; ∗ α = 35%; ▽ α = 49%; Δ α = 60%; + α = 70% .

Similarly, the dangerous zones are marked to compare with the calculations for reference surface with a roughness of 1 μm. At the same temperature and degree of contact levels, the degree of initiation of a smooth surface with R_q= 0.5 μm is shifted away from the grey band towards the lower end of the spectrum, indicating limited material transfer initiation. For the rough surface with R_q = 2 μm, the degree of initiation is shifted towards the lower end at low nominal contact pressure values, but towards higher degrees of initiation with a high nominal contact pressure, which can be explained by Fig. 6.5 and the associated discussion about attack angles at high and low pressure levels. Drifting away from the dangerous zone results in a reduced number of detached lumps for both cases compared to the reference roughness value. This shows that there is a non – linear effect of the bearing roughness on the surface defect formation.

It has been previously shown in Chapter 3 that the roughness of the bearing surface only has a marginal effect on friction, but it can be shown here that it has a remarkable yet nonlinear effect on detached lump formation. Furthermore, another complexity is added since the number of detached lumps also does not change monotonically with the degree of initiation. The most dangerous surface roughness would be one that resides well in the marked “dangerous zone”. Understandably, this “dangerous” surface roughness value is unfortunately influenced by surface topography measurements, for example, sampling resolution as limited by measuring techniques. For current calculations, either a rough (R_q = 2 μm) or a smooth (R_q = 0.5 μm) surface tends to drift away from this “dangerous” surface roughness. Therefore, it is difficult to recommend an optimum bearing roughness value that would result in a good surface quality.

6.2.4 Influence of temperature drop across the bearing interface

A temperature drop of 10 ºC across the extrudate–bearing interface has been assumed in this study for dies without additional cooling. A larger temperature drop can be achieved by implementing die cooling, and the effect is studied in this section.

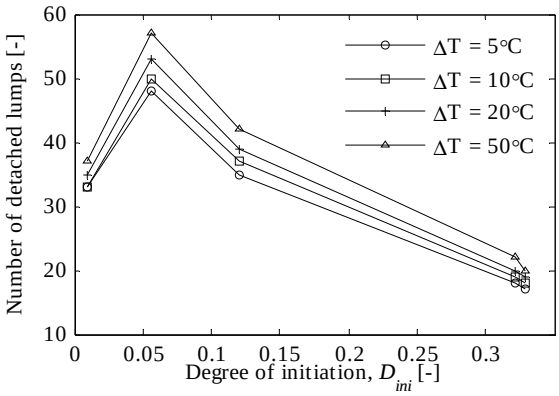

Fig. 6.21 Influence of temperature drop across the bearing interface on the number of detached lumps.

The change of this temperature drop leads to the following consequences:

- Increasing the temperature drop enlarges the hardness ratio and therefore the critical attack angle, as well as reducing the tip radius of lumps, which in turn leads to a mild decrease of the amount of material transfer during each calculation cycle and slows down the growing process marginally (Fig. 6.6).
- Increasing the critical attack angle allows a lump to grow in height for a longer period of time, therefore lump coalescence is reduced, resulting in an increased amount of detached lumps.
- Increasing the critical attack angle results in an increased coefficient of friction, in which case the lumps detach more easily.
- An increasing critical attack angle leads to a sharper lump with a high degree of indentation D_i,, as shown in Fig. 6.22. This tends to impede detachment by reducing the ratio of moments r_M (Fig. 6.13).

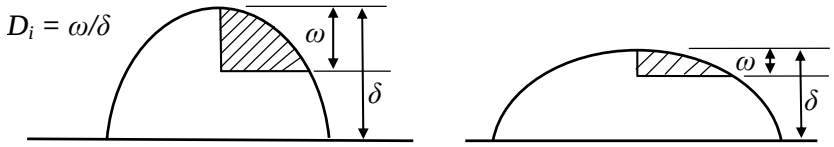

Lump with a large θ – large ΔT Lump with a small θ – small ΔT

Fig. 6.22 Lump shape of different temperature drop ΔT.

These consequences have opposing effects, but the combined result is that it can be

seen that as the temperature drop across the interface is enlarged, the number of detached lumps shows a mild increase. This shows that at the same extrudate surface temperature, the formation of detached lump favours a large temperature difference across the interface. The situation is worsened by the fact that the detached lumps are sharp in this case and scoring of the extrudate surface will follow.

However, if ΔT is large enough (roughly 100 ºC according to calculations), the critical attack angle is so large that the wear mode is effectively cutting, as seen in Fig. 6.3. The growth process of a lump will be terminated once the attack angle reaches the transition line from wedge–formation to cutting. Therefore the lump cannot grow in width and coalesce with other lumps before it stops growing. It results in sharp yet small lumps that cut through the profile and give a smooth finish, whilst remaining adhered on the bearing surface. A large temperature drop can be achieved by, say, liquid nitrogen cooling of the die, as has been performed in practice in which a superior surface finish was observed without the presence of pickups.

6.2.5 Size of detached lumps

The numbers of detached lumps shown above was obtained without considering the size of detached lumps. In reality, not all of the detached lumps should be counted — a general convention is that they only are detrimental until a threshold size is reached. The choice of this threshold length, however, remains largely subjective, for example, Parson [57] suggested that a pickup with a total length of 500 μm (head + tail) be considered critical whilst Peris [2] reckoned a value of 200 μm. De Rooij [10], by consulting experienced industrial specialists, showed that the typical defects on the product surface which are still visible after a paint procedure has a threshold depth of 20 μm and a length of 50 μm. The same convention is followed in this study, where detached lumps with a representative lateral size l_{lump} (geometrical mean of major and minor axis lengths) larger than 50 μm are considered detrimental. The average size of detached lumps is shown in Fig. 6.23:

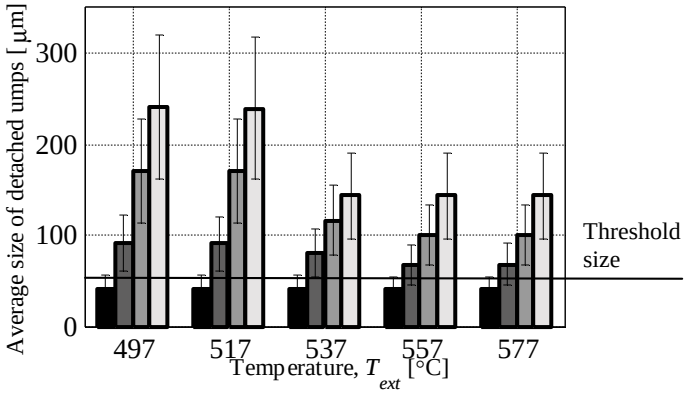

Fig. 6.23 Average size of detached lumps: α = 8.7%; α = 17.5%; α = 35 %; α = 48 %.

From the above graph it can be seen that as the nominal contact pressure is increased, the average size of the detached lumps increases. This is because the total area of lumps supporting the load is apparently larger, combined with the fact that fewer lumps are formed due to coalescence. When the threshold size is imposed, Fig. 6.17 (b) can be reproduced to consider this effect:

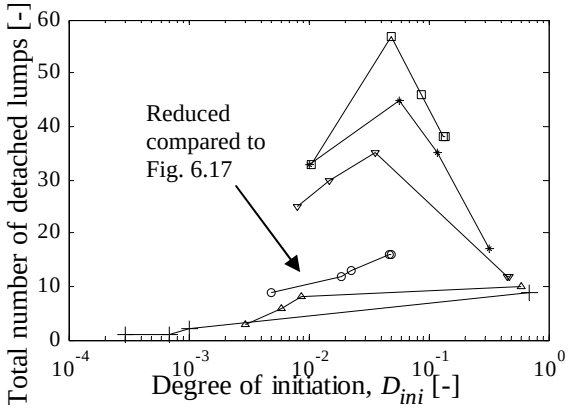

Fig. 6.24 Number of detached lumps considering the threshold size for detrimental lumps. ○ α = 9%; □ α = 17%; ∗α = 35%; ▽α = 49%; Δ α = 60%; + α = 70% .

It can be seen that the amount of detrimental detached lumps at low nominal contact pressure is significantly lessened because they are essentially smaller in size and should not be regarded as deteriorating. For larger pressure, the number is less affected as their size is mostly above the threshold value. The effect is

consistent with Parson [57] who found no pickup formation with a fully relieved die bearing.

6.3 Summary

In this chapter a physical model has been presented to calculate the detached lump formation — a direct indicator of degree of surface defects on extrusion products.

The model indicates the following:

- Formation of detached lumps is crucially influenced by the nominal contact pressure, which can be affected by the extrusion ratio, die bearing geometry, etc. At high pressure levels the number of detached lumps decreases significantly, yet the average size of the lump increases. At low pressure levels the number of detached lumps is large but size is generally smaller. This indicates that extremely low pressure reduces the number of detrimental lumps, as in agreement with industrial experience.

- Extrudate surface temperature and exit speed in combination influence detached lump formation by varying f_{hk}. A peak has been found in terms of their formation, which can be explained by interplay between the two control mechnanisms, i.e. the growth and coalescence mechanisms. It is known from industrial experience that extrudate surface temperature and exit speed are important factors influencing surface quality.

- The formation of detached lumps is very sensitive to bearing surface roughness, unlike coefficient of friction. However, the effect is very non – linear and measurement-dependent. Therefore it is difficult to recommend an exact roughness value that would yield a good surface quality.

- The temperature drop across the extrudate–bearing interface influences the amount and shape of detached lumps. Cooling encourages their formation mildly and incurs deep die lines. However, intensive cooling for example by liquid nitrogen of the die that results in a temperature difference larger than 100 ^{o}C can terminate the growth process at a premature stage, which gives superior surface quality. This is in agreement with industrial experience.

Chapter 7
Surface quality predictor — towards application to aluminium extrusion

In this chapter, the physical model discussed in Chapter 6 will be applied to the aluminium extrusion process in order to predict the surface quality of extrusion products. An example is presented, and guidance on how this surface quality predictor can be utilised is given at the end.

7.1 The surface quality predictor

The physical model presented in Chapter 6 deals with formation of detached lumps over a certain number of calculation cycles, between a nominally flat contacting pair. The result corresponds to the number of detached lumps formed at a certain location on the bearing, as shown in Fig. 6.1. When the surface quality of an extrusion product is concerned, the total number of detached lumps deposited over a certain area (thus a certain length) of the profile surface is relevant. It has been established in Chapter 6 that the exact length of the studied area is only correlated with the number of calculation cycles; and it has been shown that this value is not important as long as it is much larger than the "incubation period" occurring at the very beginning of the extrusion process where transferred aluminium is being accumulated. A large calculation cycle number also helps the solution to be less dependent on the stochastic of the input surface microgeometry. For this purpose the calculation cycle has been fixed to 100 for this study.

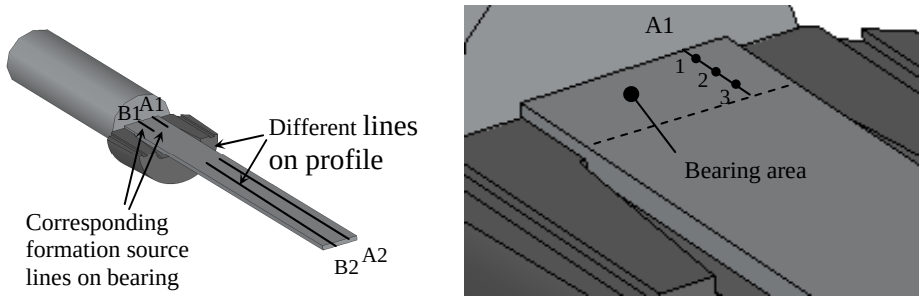

Fig. 7.1 Quantifying surface quality of an aluminium extrusion product

Suppose a certain length of the profile is studied (Fig. 7.1 (a)), it is obvious that every location of the bearing within the slipping zone contributes together to detached lump formation. As the detached lumps only move along the extrusion direction, the total number of detached lumps formed along line A1 on the bearing surface corresponds to surface defects found on the profile along line A2 (Fig. 7.1 (a)), etc. As pressure distribution along different lines (A, B, etc.) can be different for an extrusion process, it is sensible to study the situation along lines on the bearing surface (Fig. 7.1 (b)). For this purpose the studied line is segmented to several calculation locations, e.g. points 1, 2 and 3 in Fig. 7.1 (b)). The number of calculation locations is determined by dividing the bearing length with the length of the calculation area (in this study the length of the calculation area is 640 μm). Within one calculation area, the nominal contact pressure is assumed to be constant and takes the average value at that location from the pressure distribution profile along the bearing length. The summation of results from all calculation locations indicates surface defects formed along line A2 on the profile. The calculation scheme for the surface quality predictor is summarised below:

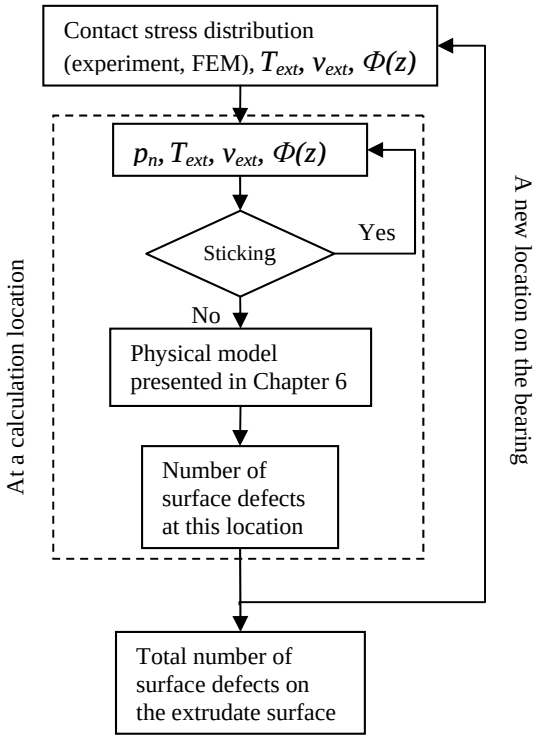

Fig. 7.2 Calculation scheme of the surface quality predictor.

7.2 An example

The nominal contact pressure distribution can be obtained from measurements or FEM. In this chapter a case study is presented where FEA of an extrusion process was performed and the nominal contact pressure has been obtained along the bearing length. The surface quality predictor has been applied to the FEM model.

7.2.1 FEM model

The 3–D FEM model simulates the extrusion of a rectangular solid profile, using MSC. Marc®. The geometry and the finite element mesh are shown in Fig. 7.3:

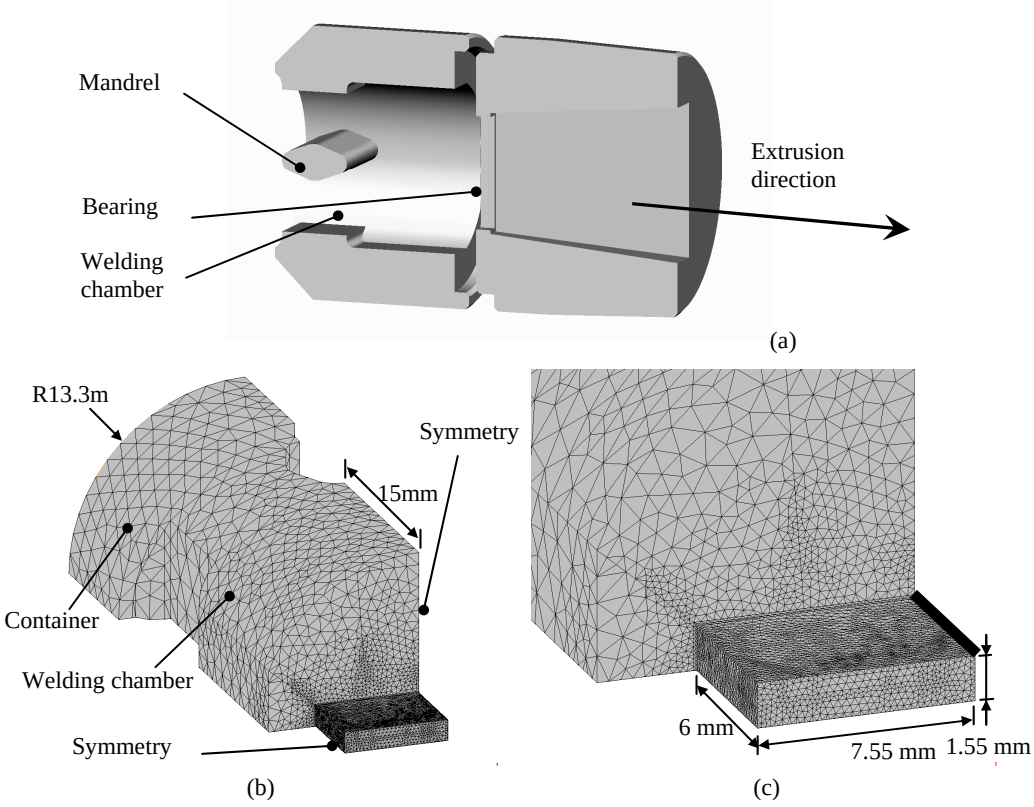

Fig. 7.3 The FEM model: (a) the die and welding chamber geometry; (b) the finite element mesh of the calculation domain; (c) the refined mesh in the bearing channel.

The extrusion profile is a rectangular solid strip with a width of 15.1 mm and a

thickness of 3.1 mm. The model features:

- Iso-thermal extrusion;
- Fully plastic constitutive behaviour of the billet material with the material data for AA 6063 used in this study;
- Fully rigid die with a parallel bearing of 6 mm bearing length;
- Full sticking boundary condition specified to the extrudate – bearing interface. This is likely to overestimate the friction level inside the bearing channel.

Simulations were run using several extrudate surface temperature values T_{ext} and exit speed values v_{ext}:

- Extrudate surface temperature: 500 ºC, 520 ºC, 540 ºC, 560 ºC, 580 ºC;
- Exit speed: 0.1 m/s, 0.2 m/s, 0.3 m/s.

7.2.2 Nominal contact pressure

The pressure distribution is obtained at the centre-line at the top bearing surface, marked as the solid bold line in Fig. 7.3 (c). The nominal contact pressure distribution along the bearing length is shown in Fig. 7.4:

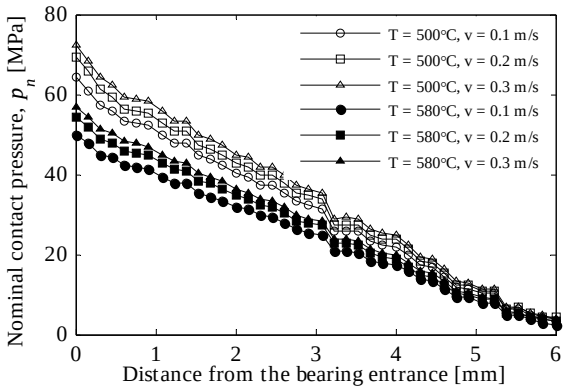

Fig. 7.4 Nominal contact pressure distribution along the bearing length from FEM.

The gradient of contact pressure inside the bearing channel is proportional with the friction stress (rewrite Eq. 2.37) considering force equilibrium:

$$\frac{\partial p_n}{\partial x} = -ct \tag{7.1}$$

Where x is the distance from the bearing entrance. Therefore the linear reduction of contact pressure towards the bearing exit can be explained by a constant shear stress equal to the shear strength at the interface, as full sticking boundary condition has been applied. It can also be seen that the pressure level decreases with temperature but increases with exit speed. This is due to the constitutive behaviour of the aluminium alloys.

7.2.3 Effect of temperature and exit speed on surface quality

The calculated number of detached lumps is shown in Fig. 7.5:

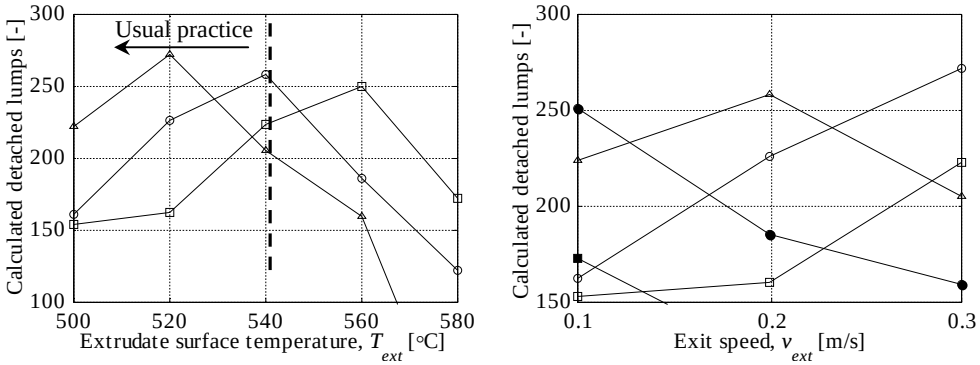

Fig. 7.5 Calculated number of detached lumps for an extrusion process: (a) "peak" over temperature; (b) "peak" over exit speed. Legend: (a) □ v_{ext} = 0.1 m/s, ○ v_{ext} = 0.3 m/s, Δ v_{ext} = 0.3 m/s; (b) □ T_{ext} = 500 ºC, ○ T_{ext} = 520 ºC, Δ T_{ext} = 540 ºC, ● T_{ext} = 560 ºC, ■ T_{ext} = 580 ºC.

It can be seen that "peaks" of detached lumps (thus surface defects) occur both for temperature and exit speed; that means surface quality does not deteriorate or improve monotonically with temperature or exit speed. The surface quality deteriorates with increasing extrudate surface temperature or exit speed until a peak is reached; further increase in temperature or exit speed actually reduces surface defect formation and thus improves surface quality. The position of the peak varies with temperature and speed though: for extrusion with a high extrudate surface temperature, surface defect formation peaks at a lower exit speed (Fig. 7.5(b)); likewise, for extrusion with a high exit speed, the worst surface quality appears at a lower temperature (Fig. 7.5(a)). This is due to variation of f_{hk} value as a result of changing T_{ext} and v_{ext}. The results are in good agreement with observations from Parson et al. [57], which are shown in Fig. 2.23.

The above results can be related to the varied f_{hk} value at different temperature and / or speed, as has been discussed in Chapter 6. This suggests, in order to avoid pickup problems, that one should extrude using process parameters far away from those "peaks". This effectively means that either low temperature or / and exit speed values should be used in order to form a continuous aluminium transfer layer on the bearing, or extruding over the "peaks" using high temperature and exit speed values, in order to weaken the interface and therefore decrease the amount of transferred material. The surface quality is inferior when speckled transfer material spots are deposited on the bearing surface. However, for AA 6063 extrusion, the acceptable exit temperature should be limited to no higher than 530 ~ 540 ºC [91] otherwise grain growth leading to dull appearance becomes a problem itself. It thus becomes questionable whether extruding using very high exit temperature is valuable. Nevertheless, from Fig. 7.5(b) it can be concluded that for this particular extrusion, extruding with an exit speed higher than 0.3 m/s can actually be beneficial, provided the exit temperature can be controlled well (this value of 0.3 m/s is, however, dependent on the f_{hk} expression, as will be discussed in Chapter 9).

7.2.4 Constructing a surface quality diagram

The above results are not directly implementable unless a surface quality diagram is constructed to form a process window in terms of surface defects, incorporating the extrudate surface temperature and exit speed. Such a surface quality diagram for this particular extrusion has been constructed and is shown in Fig. 7.6:

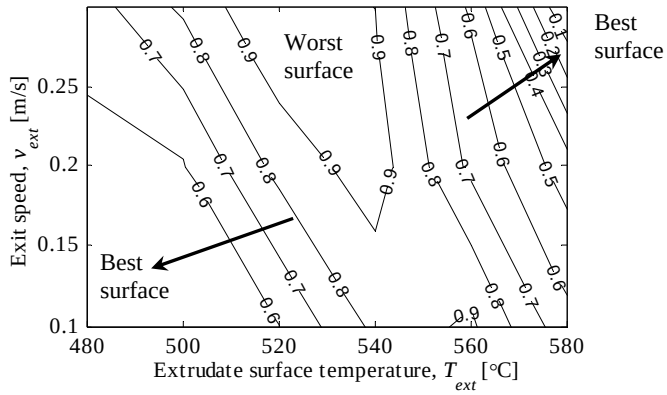

Fig. 7.6 The surface quality diagram for the example extrusion. Arrows indicate directions of good surface quality.

The normalised numbers in Fig. 7.6 show the relative number of surface defects,

with “1” suggesting the worst surface quality. The area for the worst surface quality forms a narrow band, and is inclined: for higher exit speed values the temperature at which this worst surface quality occurs is decreased. The two arrows indicate how the process parameters can be adjusted to improve surface quality — to get away from the “worst surface” by following the arrows.

It is worth mentioning that such a surface quality diagram is subject to change, if e.g. the nominal contact pressure level or bearing roughness value are changed. For a certain bearing the surface quality diagram is constant. This suggests, if it is only the process parameters (temperature and exit speed) that are to be selected (after the die has been designed), a surface quality diagram showing normalised numbers such as Fig. 7.6 can suffice. Rather, when die and bearing design is part of the design process, such a surface quality diagram should be calculated for each bearing geometry, and in this case the exact number of surface defects needs to be compared between different diagrams in order to optimise die bearing design with respect to surface quality.

7.3 How to extrude according to the surface quality predictor?

To end this chapter, the surface quality predictor is placed inside the design cycle of an extrusion process. How to extrude according to the surface quality predictor? The proposed procedure is as follows:

- Construct the conventional limit diagram. This diagram shows the appropriate process window for a particular aluminium extrusion process. The limit diagram usually consists of loci constraining press capacity (curve A in Fig. 7.7), prevention of surface tearing (curve B) and the desired mechanical properties (curve C). Additional constraints can be added to achieve other requirements.

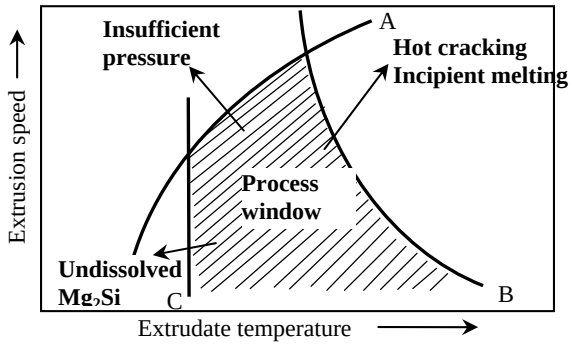

Fig. 7.7 The limit diagram (reprint of Fig. 1.4) of aluminium extrusion.

- If surface quality is of utmost importance, the surface quality diagram should also be taken into account.

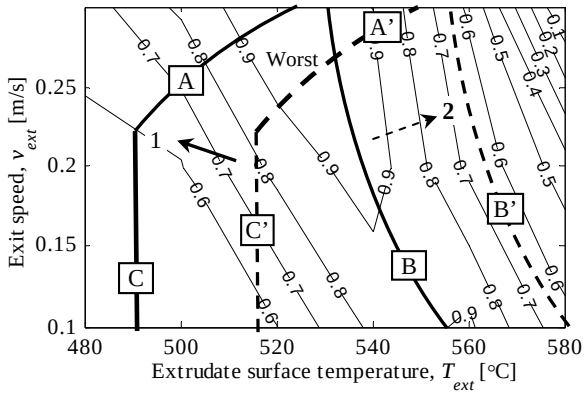

Fig. 7.8 Design a process based on both the limit diagram and the surface quality diagram.

In this case, suppose the bold solid lines (A, B and C) in Fig. 7.8 enclose the process window determined from the limit diagram, and surface quality is important so the surface quality diagram and the limit diagram are superimposed to design the process. One should then try to get away from the "worst surface" area as much as possible. Usually productivity cannot be compromised, and the combination of temperature and exit speed should be selected to the vicinity of line A and C, for example location 1 will be a good selection in Fig. 7.8. However, if the process window is enclosed by the dotted lines (A', B' and C'), one has the opportunity to extrude "over the peak", as indicated by the dotted arrow to location 2. It can be seen that as the surface quality diagram and the limit diagram are vastly different for

each particular extrusion process, the design process should really be customised.

7.4 Summary

This chapter presents the developed surface quality predictor and how it can be used to achieve good surface quality, in terms of a surface quality diagram. An example has been given, in which FEM of the extrusion process is included to obtain the pressure distribution along the bearing. It can be concluded:

- The surface quality predictor results in the same observation as previous findings: surface quality generally deteriorates with increasing extrudate surface temperature and exit speed until a peak is reached; further increase will improve the surface quality.

- With the combination of the limit diagram and the surface quality diagram, an extrusion process can be tailored to give the best results in terms of productivity and surface quality.

Chapter 8
Split die extrusion experiments
Part II: Validation of the surface quality predictor

In part II of the experiments the objective was to measure surface pickups on extruded profiles to validate the surface quality predictor. As discussed in Chapter 5, two forms of surface defects are of interest: 1) A tail of torn region with a fleck of material in the front — the "head"; 2) only the torn region without the head. Aesthetical or functional problems arise from those with the head typically larger than 50 μm; this threshold value was imposed on the measurements and will be discussed in this chapter.

8.1 Experiments

8.1.1 Experimental setup

In part II the arrangement of extrusion facilities remains the same as part I (Chapter 4). It contains three series:

- Series 1: Select dies that produce a significant amount of pickups.
- Series 2: Study the effect of extrusion history on the formation of pickups.
- Series 3: Study the effect of extrudate temperature on the size and number of pickups.

In series 1 of the extrusion experiments twelve dies were used for extrusion, each extruding two billets one after the other. In order to validate the contact and friction model, the reference dies were made with a choked bearing of +20' so that the separation marks for sticking and slipping zones could be clearly seen. However, these settings might not be optimal for observing surface defect formation. Therefore another objective of series 1 was to select dies that would produce a good measurable amount of pickups on profiles. The aim of series 2 and 3 was to study formation of surface pickups. The temperature and speed measurements are shown in Table 4-2.

It has been found that profiles produced by die #11 and #12 show a significantly

larger amount of surface pickups. These two dies were selected for series 2, and each die extruded three billets. The objective was to measure formation of pickups as a function of extrusion time (therefore extrusion history). For this purpose the two bearings were not cleaned prior to extrusion, so that the initiated lumps on the bearing from series 1 could grow in series 2 and in the end contribute to pickup formation. In this way, the formation of surface pickups for the first five billets could be monitored as a function of extrusion time. Similarly, the extrudate surface temperature for series 2 can be shown in Table 8-1:

Table 8-1 Extrusion measurements from series 2 experiments.

Extrusion runs	Die	Temperature [°C]			Speed [mm/s]		Pressure [MPa]	
		Billet	Extrudate surface	Increase	Ram	Exit	Breakthrough	End
Parallel bearing	11	448	471	23	1	16.9	700	185
Relieved bearing	12	451	473	22	1	16.9	669	181

By comparison with Table 4-2 it can be seen that the extrusion pressures of die #11 and die #12 decreased compared to the previous series, due to a very small amount of die deflection. After the extrusion processes, the dies were split up for characterisation. The number and size distribution of pickups were measured on products extruded from the first, the second and the third billet, respectively, to study the effect of extrusion history.

In series 3 the same dies were selected. The objective was to observe the influence of process parameters on the formation of pickups. The selected dies extruded with four different billet temperatures, with three billets extruded with each temperature setting. The objective was to examine the effect of temperature on the formation of pickups. The extrusion measurements are shown below in Table 8-2:

Table 8-2 Extrusion measurements from series 3 experiments.

Extrusion runs	Die	Temperature [°C]			Speed [mm/s]		Pressure [MPa]	
		Billet	Extrudate surface	Increase	Ram	Exit	Breakthrough	End
Parallel bearing	11	489	517	28	5	84.5	481	179
Relieved bearing	12	415	460	41	5	84.5	630	223
Parallel bearing	11	558	577	19	5	84.5	335	137
Relieved bearing	12	537	557	20	5	84.5	400	154

It can be seen that as the billet temperature increases, the extrusion pressure is decreased substantially due to thermal softening of the aluminium.

8.1.2 Measurement of surface defects

In this thesis surface defects found on the extruded profiles were evaluated in the following forms:

- A “pickup head” with a lateral dimension larger than 50 μm;
- A “tail” without a “head” with a length larger than 200 μm. This value has been chosen as it was the shortest tail length of any detrimental pickup heads found on the profile.

The total number of these two categories of surface defects also corresponds to the calculated number of detached lumps from the surface quality predictor described in Chapter 7. The total number of surface defects found on one side of the extrudate suface has been counted. The height and length of pickup heads were measured using an optical microscope at a magnification of 25 times. The height of the pickups has been obtained by measuring the length of the shadow created, as a result of illumination of the pickup head from its side at a given angle of 18.4º. This angle gives a height/shadow ratio of 1/3.

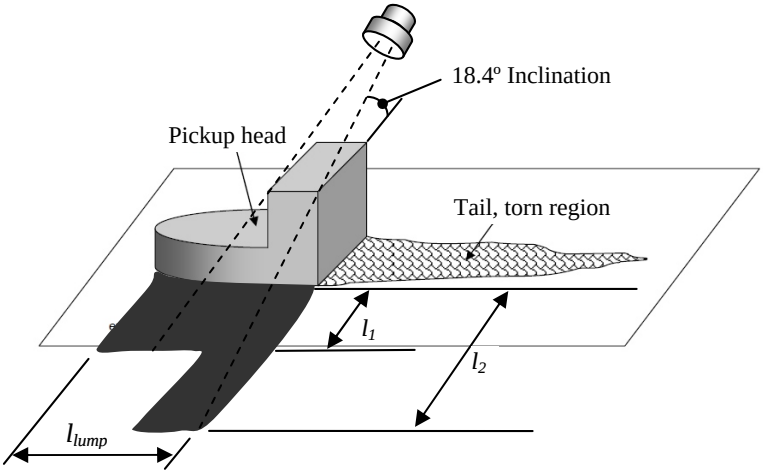

Fig. 8.1 Geometrical measurements of a pickup head.

It should be noted that as the high part of the pickup head attributes to bending of the lump, the pickup height measurement should be correlated to the shadow length

of the low part, l_1 in Fig. 8.1; so that $h_{lump} = l_1/3$.

8.2 Validation scheme

Following the approach of the surface quality predictor introduced in Chapter 7, a validation scheme can be presented. The number of calculation locations on the bearing is 13 for reference bearing length die and 8 for the short bearing length die.

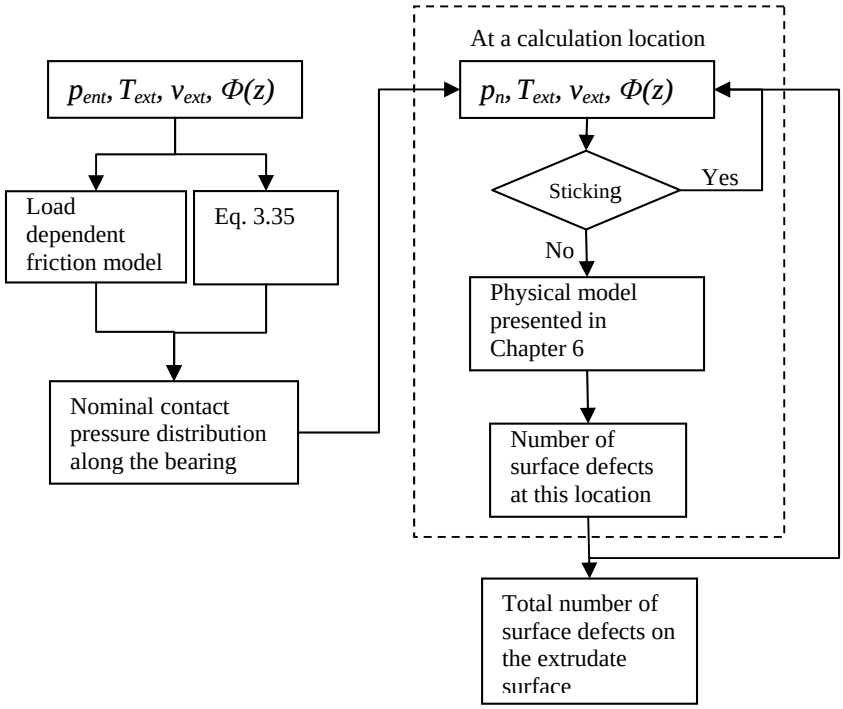

Fig. 8.2 Validation scheme of the surface quality predictor.

The input surface height data conforms to the measured surfaces according to procedures mentioned in Section 4.1.

8.3 Results and discussion

8.3.1 Series 1

8.3.1.1 Measurements

In series 1 each die extruded two billets. On the surfaces of extrudates from the first billets, the visual surface characteristics are quite identical: the samples are full of die lines; no severe score lines can be found; pickups are very rare. On the surfaces of products extruded from the second billets, the amount of surface defects generally increased; a reasonable amount of pickups appeared on all the samples, especially on the extrusions from the parallel die and the relieved die. The result is shown in Fig. 8.3 (numbering of dies and associated extrusion conditions are shown in Table 4-2). The measuring area corresponds to one side of the extruded strip of one billet, which is 1520 mm × 1mm.

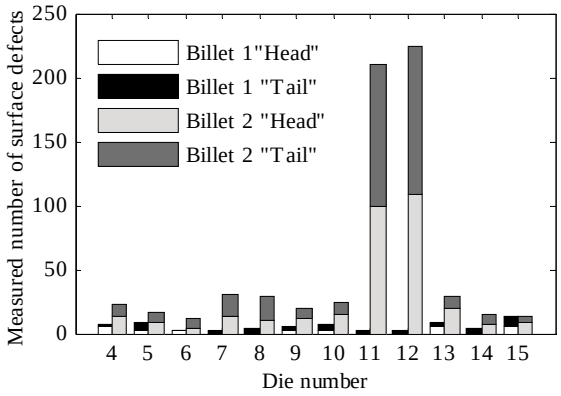

Fig. 8.3 Measured number of surface defects on extrusion product surfaces from series 1. “Head” refers to the pickup head; “Tail” refers to the torn region without a pickup head.

The average size of pickup heads from billet 2 is shown in Fig. 8.4:

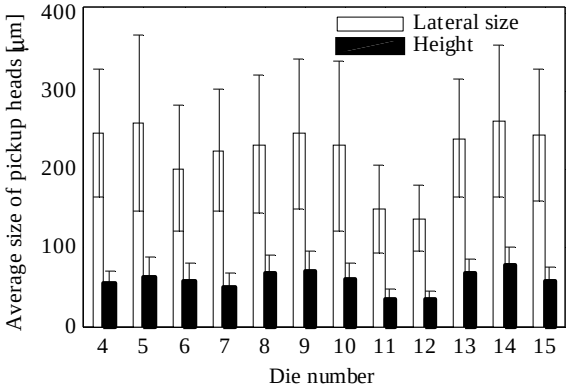

Fig. 8.4 Measured size of surface defects on extrusion product surfaces from series 1.

EDX analysis of the bearing surface reveals that the transferred aluminium acquires different morphology on a parallel / relieved die bearing from a choked bearing, as shown in Fig. 8.5:

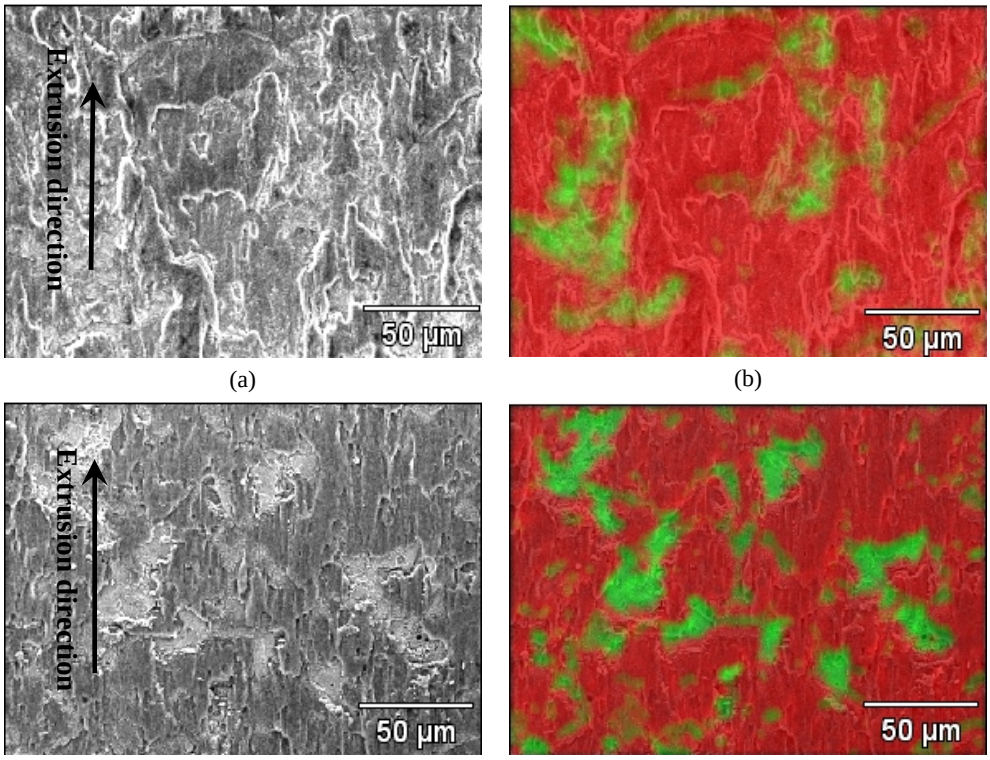

Fig. 8.5 Observations of the transferred aluminium on die bearings: (a) morphology of the transferred aluminium on die #4; (b) EDX analysis of the transferred aluminium on die #4: red – aluminium, green – iron; (c) morphology of the transferred aluminium on die #12; (d) EDX analysis of the transferred aluminium on die #12: red – aluminium, green – iron.

From Fig. 8.3 and Fig. 8.4 it can be clearly seen that:

- On product surfaces from billet 2, the amount of surface defects increased substantially. Therefore billet 1 can be correlated with the “incubation period” observed from the physical model described in Chapter 6.
- Die #11 (parallel bearing) and die #12 (relieved bearing) produced significantly more surface defects than other extrusion runs in billet 2

extrusion.

- The effect of bearing roughness on surface defect formation cannot be clearly concluded from the experiments, as the amount of surface defects was not substantial.
- The number of “tails without heads” is roughly equal to the number of pickup heads.
- The average size of pickup heads varies and no clear indication is shown. Pickup heads from die # 11 and 12 show smaller sizes.

The most important observation is that dies with parallel and relieved bearings produced significantly more surface defects than the other dies. This can be related to a low contact stress within the bearing channel associated with the non – choked dies, as can be concluded from Chapter 6. Transferred aluminium morphology and EDX studies of the relieved die (#12) and the reference die (#4) show that the transferred aluminium coalesced to form a continuous layer on the choked die bearing, whilst on the relieved die bearing, the speckled appearance indicates that it is growth controlled rather than coalescence controlled, as discussed in Chapter 6.

The number of “tails without heads” being roughly equal to that of the pickup heads suggests that the total number of these two forms can be related to the amount of pickup heads, which are detrimental to surface quality. This means that what the surface predictor calculates, which is the total event of detached lumps, can be directly related to surface quality deteriorating pickup heads.

8.3.1.2 Validation

Calculations have been performed to give the total number of detached lumps (thus corresponding to the summation of pickup heads and “tails without heads” from the experiment measurements) at the end of 100 calculation cycles to reduce the dependency of the result on the input surface microgeometry. Since the number of detached lumps from the surface quality predictor does not numerically correlate to the number of measured surface defects, all the numbers have been normalised by that of the relieved die to enable comparison. A discussion on how to interpret the calculated numbers is raised in Chapter 9. The normalisation procedure means that the measured number of surface defects has been normalised by measured surface defects found on die #12 product surface, and the calculated number of detached lumps has been normalised by the calculated number of detached lumps of die #12.

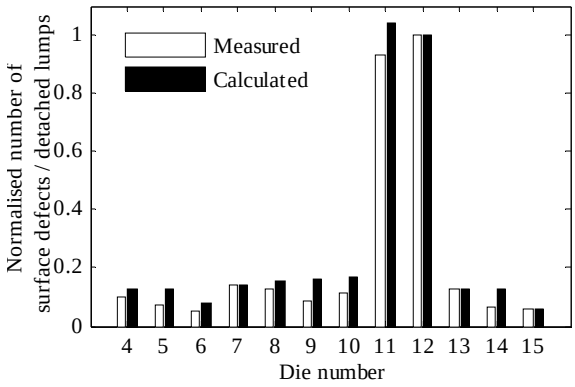

Fig. 8.6 Comparison between measured and calculated number of surface defects / detached lumps for series 1 extrusion experiments.

Similarly, the average lateral size of the surface defects can be compared:

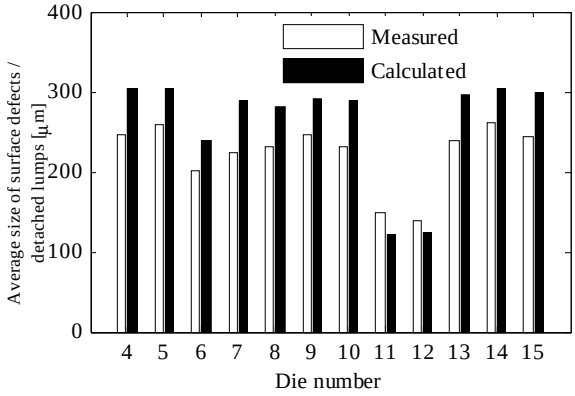

Fig. 8.7 Comparison between measured and calculated average lateral size of pickup heads / detached lumps for series 1 extrusion experiments.

It can be seen from the above figures that the model captures the fact that a low contact stress inside the bearing channel is favoured by surface defect formation. This is due to the fact that: 1) the parallel and relieved dies have longer slipping zones due to low contact pressure; 2) coalescence of transferred aluminium is hindered by the low contact pressure which encourages formation of detached lumps, as discussed in Chapter 6. Predictions of other dies are also reasonable; however, the results are less accurate because the dies did not produce a large amount of surface defects and the measured values were more subject to local

instabilities. From Fig. 8.7 it shows that the model agrees with the measurements that die # 11 and #12 produced smaller defects than other dies, however, there is some discrepancy between the exact figures.

8.3.2 Series 2

In series 2 the effect of extrusion history was studied. For this purpose the chosen dies from series 1 (the parallel bearing die and the relieved bearing die) were not cleaned before each extruded three billets in this series. It was found that right from the first billet of this series pickups started to form without the presence of an incubation period, suggesting indeed that the adhered aluminium from the previous series contributed to the formation of pickups in this series. Therefore, the effect of five billets extruded could be studied. The number of pickups is shown below (billet 1 and 2 from the first series, billet 3, 4 and 5 from the second series):

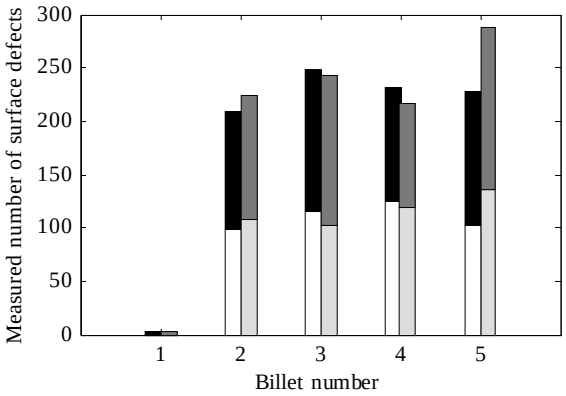

Fig. 8.8 Measured number of surface defects on extrusion product surfaces from series 2 and series 1 (First 5 billets of die #11 and die #12): die #11 head; die #11 tail; die #12 head; die #12 tail.

It can be seen that as the extrusion process proceeded, the amount of pickups reached a steady state, for both dies. This steady state, in the settings of this study, is after one billet. This means that the steady state for pickup formation was reached already in the beginning of the second series. The steady state corresponds to cancelling out of the “incubation period” of pickup formation at different locations of the bearing due to different nominal contact pressure values whereas in the very beginning of the extrusion process every part of the bearing is in the accumulating stage of the growth process, thus revealing a macroscopic incubation period. This observation matches the fact that a steady state also appeared during

the calculation of the number of detached lumps over calculation cycle.

8.3.3 Series 3

8.3.3.1 Measurements

In series 3 of the extrusion experiments the same dies were selected again to study the effect of process parameters, namely, extrudate surface temperature. Different extrudate surface temperatures were achieved by prescribing billet temperature. The bearings were completely submerged in caustic soda at 80 ºC so that any transferred aluminium from the previous two series was removed. The incubation period occurred again due to nascent bearing surfaces, therefore all the measurements were taken from billet 3 of this series. The measured number of surface defects of series 3 is shown in Fig. 8.9:

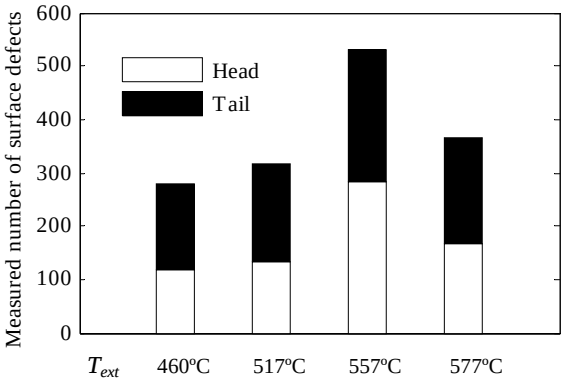

Fig. 8.9 Measured number of surface defects on extrusion product surfaces from series 3.

The average size of pickup heads can be shown in Fig. 8.10. It can be seen that the measured amount of surface defects slightly increases from an extrudate temperature of 460 ºC to 517 ºC, and then rapidly increases to and peaks at T_{ext} = 557 ºC. For a higher temperature the amount decreases again. The average lateral size of pickup heads generally decreases as the extrudate surface temperature rises. The effect can be explained by different f_{hk} values as a result of increasing extrudate surface temperature at the interface, as shown in Fig. 8.11. This figure shows that when the temperature or speed is low, the f_{hk} value reaches unity, indicating a very strong interface between the bearing and extrudate surface. This results in transfer of an aluminium layer instead of speckles, which impedes pickup formation. As the temperature or speed increases, the f_{hk} value decreases, resulting

in speckled growth of transferred aluminium, which tends to increase pickup formation, according to the physical model.

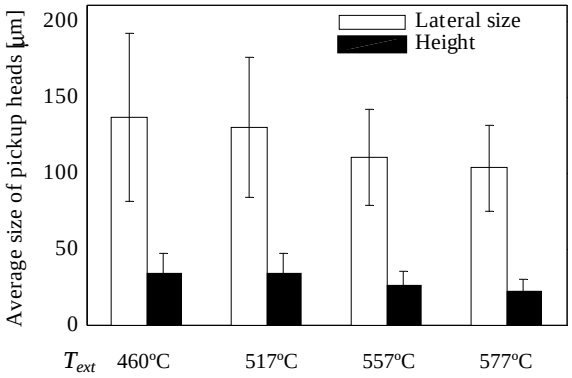

Fig. 8.10 Measured size of surface defects on extrusion product surfaces from series 3.

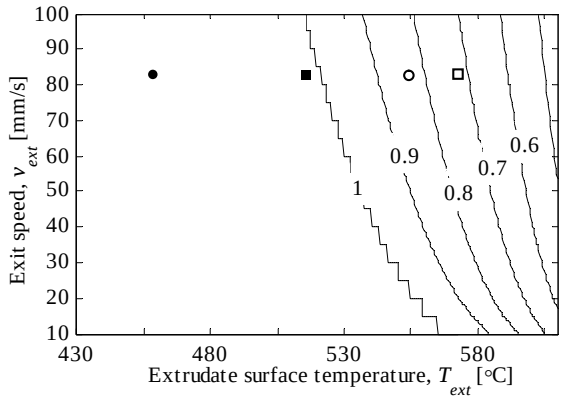

Fig. 8.11 Interfacial shear factor for series 3 extrusion experiments:
● 460 ºC; ■ 517 ºC; □ 557 ºC; ○ 577 ºC.

8.3.3.2 Validation

Similar to Section 8.3.1.2, the normalised number of detached lumps is used as an indicator for validation, as shown in Fig. 8.12:

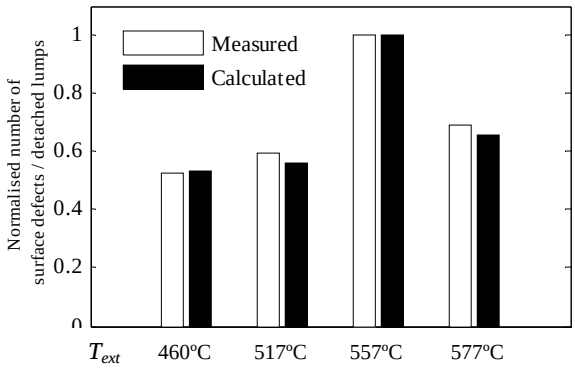

Fig. 8.12 Comparison between measured and calculated number of surface defects / detached lumps for series 3 extrusion experiments.

Comparison for the average lateral size of the surface defects is in Fig. 8.13:

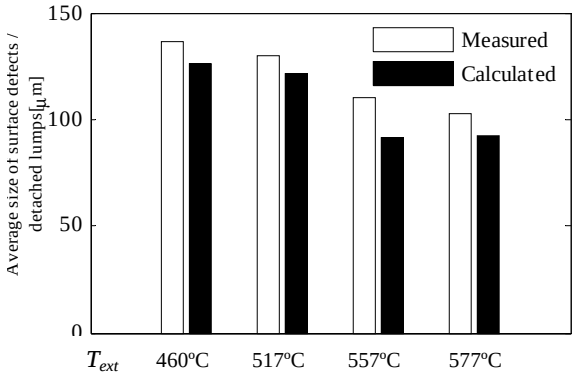

Fig. 8.13 Comparison between measured and calculated average lateral size of pickup heads / detached lumps for series 3 extrusion experiments.

The above results show that the surface quality predictor gives good predictions of the (normalised) number of surface defects as well as their size. The model captures the effect of f_{hk} values (extrudate surface temperature) and its effect on the size of surface defects: the amount of surface defects increases with temperature until a peak is reached; further increase in temperature actually reduces surface defect formation, as discussed in Chapter 7.

8.4 Summary

This chapter presents and discusses validation of the surface quality predictor developed in Chapter 6 and Chapter 7 by means of split die extrusion experiments. The amount of surface defects of two forms (the pickup heads and "tails" without a head) was measured, as well as the average size of the pickup heads. It has been shown that the surface quality predictor gives a good prediction on both the (normalised) amount of surface defects and the size of them. According to both the developed model and measurements, the following conclusions can be drawn:

- Variation of nominal contact pressure along the bearing results in substantial change in surface quality — surface defect formation favours a low to medium pressure level. Such conditions elongate the slipping zone, and in the meantime the formation mechanism is changed from coalescence controlled to growth controlled.
- Bearing roughness has been shown to have an effect on surface defect formation, but due to short slipping zones in series 1, no clear indication can be justified.
- Operational conditions such as extrudate surface temperature and exit speed influence surface quality by varying the f_{hk} value. It has been shown that the amount of surface defects increases with T_{ext} until a peak is reached; further increase in temperature leads to less surface defect formation.

Chapter 9
Conclusions, discussions and recommendations

This chapter closes the research and summarises the most important conclusions, which have already been presented at the end of each chapter. Some discussions were raised during the period of this study and are presented in this chapter as well. Finally, recommendations for further research will be proposed.

9.1 Conclusions

Chapter 3: Modelling contact and friction in aluminium extrusion processes.

- The classical summit-based contact model fails to accurately describe the contact situation under high contact pressure conditions, as individual summits have already coalesced with each other to form “contact patches”.

- The coalescence process has been tackled by developing a contact patch-based contact model — the load dependent contact model. This contact model gives an accurate description of the contact area and geometry of the contacting spots. It shows that the contact situation is load dependent: at small loads separation is high, therefore contact patches are roughly equivalent to summits; at high loads summits coalesce together to form contact patches, resulting in a much blunter contacting microgeometry.

- A friction model has been developed based on the load dependent contact model. The model shows the coefficient of friction is influenced by the nominal contact pressure and the interfacial shear factor f_{hk}. Surface roughness is only influential at small loads.

- The developed load dependent contact and friction model has been applied to the bearing area, which shows that in aluminium extrusion the bearing surface roughness does not alter the coefficient of friction significantly. Instead, the f_{hk}

value (thus temperature and exit speed) and the nominal contact pressure inside the bearing channel proved to be the most influential.

- The coefficient of friction inside the bearing channel can be evaluated by measuring the length of sticking / slipping zones on the bearing. The larger the friction, the longer the sticking zone (the shorter the slipping zone).

Chapter 4: Split die extrusion experiments — Part I: Validation of the contact and friction model.

- It has been shown that the surface roughness of the bearing has little influence on the sticking / slipping lengths (therefore coefficient of friction); increasing the contact stress levels, however, substantially elongates the sticking length and vice versa; varying operational conditions such as extrudate surface temperature and exit speed also influences the sticking / slipping lengths. The contact stress levels can be changed by using different bearing angles, bearing lengths, and extrusion ratios.

- Sticking / slipping zones can be measured on the bearing surface using split die extrusion. There is transferred aluminium adhered on the bearing surface in the slipping zone; the layer in the sticking zone was removed by the splitting of the die.

- A comparison of the model and experiments shows that the load dependent contact and friction model predicts well the level of friction inside the bearing channel.

Chapter 5: On the formation of surface defects of aluminium extrusion products.

- The formation of surface defects, including pickup heads and “tails without heads”, is closely related to material transfer between the bearing and extrudate surfaces. In a nutshell, a surface pickup is formed from extrudate material, following a cycle of transfer to the bearing, growth, detachment and back transfer to the extrudate.

- Surface defects investigated can be related to detached lump formation; although they are not necessarily deposited on the extrudate surface.

Chapter 6: Modelling formation of surface defects on aluminium extrusion products.

- A physical model that describes the formation of detached lumps has been developed.

- The model shows that the formation of detached lumps is crucially influenced by the nominal contact pressure. The number of detached lumps increases substantially with decreasing pressure, while the average size decreases. When the threshold value for detrimental defects is imposed this shows that at extremely low pressure surface defect formation is alleviated, albeit the total amount of detached lumps is high.

- The f_{hk} value also greatly influences detached lump formation. As f_{hk} value decreases from unity to 0.5 (increasing extrudate surface temperature or exit speed), detached lump formation is first coalescence controlled, then growth controlled. This manifests as a peak in detached lump formation over a certain temperature or exit speed.

- Although bearing roughness has little influence on the coefficient of friction, it does affect formation of detached lumps. The effect is largely nonlinear and measurement-dependent.

- Increasing the temperature drop across the bearing–extrudate interface mildly increases detached lump formation. However, the process can be fully terminated when a very large temperature difference is present, e.g. by nitrogen cooling of the die.

Chapter 7: Surface quality predictor — towards application to aluminium extrusion.

- The surface quality predictor indicates the same observations as previous findings: surface quality generally deteriorates with increasing extrudate surface temperature and exit speed until a peak is reached; further increase will

improve the surface quality.

- An extrusion process can be tailored, using both the limit diagram and the surface quality diagram.

Chapter 8: Split die extrusion experiments — Part II: validation of the surface quality predictor.

- Results from the surface quality predictor, i.e. the number of detached lumps and their size, are in good agreement with split die extrusion experiments.
- Surface defects favour low pressure level inside the bearing channel.
- Surface defects have a close relationship with the f_{hk} value, which can be changed by extrudate surface temperature and exit speed.

9.2 Discussions

9.2.1 Metallurgical aspects

The approach undertaken in this study is based on a mechanical process of material transfer and lump detachment. This study explores fundamentals and means in terms of adjusting the operation to better surface quality. The approach derives from chemical and microstructural analysis of the pickup deposits, which shows that they are made of exactly the same material as the bulk extrudate. This analysis invalidates the previous conclusions made in the literature [26] that pickups are formed by Al or Mg oxides.

However, one should not overlook the metallurgical aspects of the aluminium extrusion process, as they have been repeatedly reported to have a stem in surface quality of extrusion products [7][91][92]. Means to control surface quality with respect to metallurgical aspects are: 1) chemical composition of the billet and the tool; 2) homogenisation prior to extrusion. It has been said that the essence of reducing pickup is to minimise the content of the plate-shaped β–AlFeSi particles, by means of implementing full homogenisation of the billets [6][7][91], increasing Fe content and / or decreasing the Mg content [7], and increasing Mn content to decrease homogenisation time [6].

Furthermore, how do these plate-shaped intermetallic particles contribute to the proposed surface defect formation mechanism? Is there a way to integrate both

mechanical and metallurgical influences? It has been said that the peritectic reaction in Al–Fe–Mg–Si alloys at grain boundaries creates liquid phase and weakens the grain boundaries.

Al + **Mg_2Si** + **$FeSiAl_5$** (β) ↔ **Liquid** + **Fe_2SiAl_8** (α) at 576ºC

A formation mechanism of surface defects was proposed by Minoda [7] that involves such weakening of the grain boundaries and "dropping out" of the extrudate surface material:

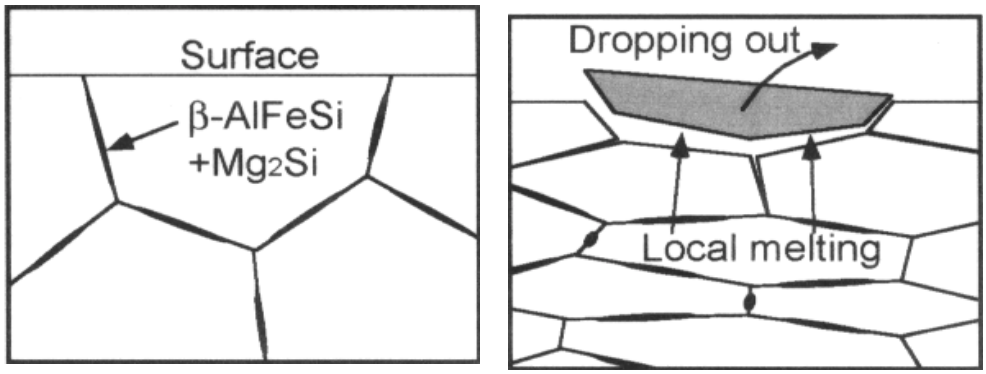

(a) (b)

Fig. 9.1 A pickup formation mechanism involving peritectic reaction at the grain boundaries at 576 ºC, proposed by Minoda: (a) before extrusion; (b) during extrusion [7].

The above statements effectively suggest that if there is no melting occurring at the grain boundaries, i.e. temperature is not high enough (< 576 ºC), there would be hardly any pickup formation, which is inconsistent with industrial experiences.

The approach adopted in this study, however, does not emphasise that local melting has to actually occur to form pickups; instead it is believed that the presence of these plate-shaped β–AlFeSi particles induces a lot of stress concentration along the grain boundaries during contact with the bearing, resulting in an inhomogeneous matrix of the extrudate surface. The transfer of material studied in this thesis is based on a homogeneous soft matrix; when taking into account the grain boundary weakening effect and the heterogeneity of the surface, the amount of material transferred during each calculation cycle is different. This means the magnification factor m_a will in fact depend on metallurgy of the surface material, e.g. grain size and second phase particle distribution.

Therefore it can be stated that operational conditions being the same (temperature, exit speed, die geometry), a high content of β–AlFeSi particles alters the stress field in the extrudate surface material and contributes to surface defect formation. In this way, mechanical and metallurgical aspects are correlated.

9.2.2 The interfacial shear factor f_{hk}

In this study, the coefficients c_1, c_2 in the expression of interfacial shear factor f_{hk} (Eq.3.32 and Eq. 3.33) have been determined to fit Tverlid's split die experiment and their sticking / slipping length measurements [26]. However, as it is an interfacial parameter based on mutual adhesion, it is largely dependent on the interfacial chemistry and local conditions. More importantly, the actual value of f_{hk} is crucial in determining the optimum condition in terms of surface quality. In aluminium extrusion, the value of these coefficients can be altered due to a number of reasons:

- Different atmospheric conditions (possible oxide layer formed to decrease adhesion);
- Different alloy composition and bearing surface combinations (altered interfacial chemistry and adhesion).

The atmospheric condition in the bearing area of aluminium extrusion is close to an inert environment with partial oxidation. Under these conditions metal–metal adhesive contact is dominant. However, this condition can be changed by artificial feeding of air, or on the other hand inert gas such as helium. Feeding of air into the bearing channel incurs excessive oxidation of the extremely reactive nascent aluminium surface, reducing adhesion between contacting surfaces. This results in a weaker interface and a reduced f_{hk} value. Feeding of inert gas flushes away oxygen and prevents oxidation, results in pure metal–metal contact and large f_{hk} value. The effect was verified by Tverlid [26], who showed that flow of air into the bearing area results in longer slipping length (lower friction and f_{hk}) and flow of helium with longer sticking length (higher friction and f_{hk}). The atmospheric condition also varies with bearing length: at the bearing exit it is easier for oxygen to penetrate to the contact than close to the bearing entrance. This suggests that the f_{hk} value will in reality vary along the bearing length. The obtained value from the sticking / slipping length measurements is only an average value.

Changing the interfacial chemistry, e.g. alloy composition or surface treatment of

the bearing surface can also change mutual adhesion and therefore f_{hk}. Take 7XXX aluminium alloys for example, with the addition of Cu and Zn which are fully compatible with iron [83], their mutual adhesion with the bearing surface is similar to 6XXX aluminium alloys with silicon. However, 7XXX alloys are twice as hard [1], therefore it can be postulated that at the same temperature and sliding speed condition, the f_{hk} value of 7XXX alloys is lower. On the contrary, the f_{hk} value for soft alloys such as 1XXX alloy is higher because of low hardness. In order to quantify the effect, additional calculations based on pressure profile and temperature obtained in Chapter 7 were made using different f_{hk} expressions (c_1 refers to Eq. 3.32):

- $c_1 = 0.16$ to simulate effect of inert environment and soft alloys. The corresponding surface quality diagram is shown in Fig. 9.2 (a);
- $c_1 = 0.1$ to simulate effect of oxidative environment and hard alloys such as 7XXX or 2XXX aluminium alloys. The corresponding surface quality diagram is shown in Fig. 9.2 (b).

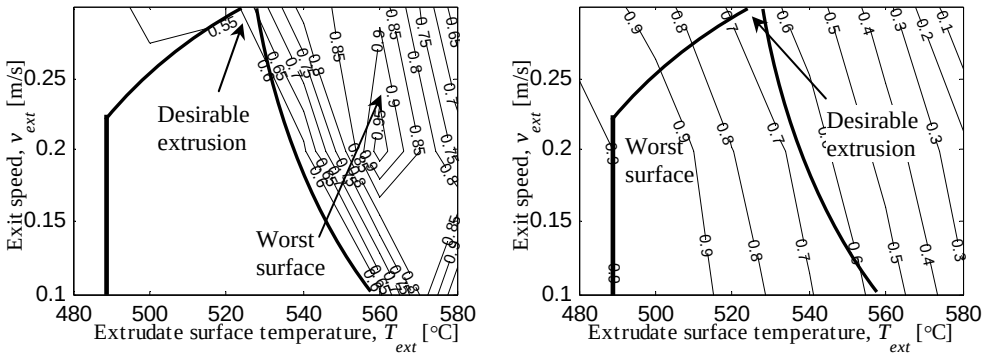

Fig. 9.2 Surface quality diagrams for different f_{hk} expressions.

Compared to Fig. 7.6, it can be seen that when the f_{hk} value is lowered, the worst surface quality is shifted towards higher temperature values, and vice versa. Suppose the process window determined by the limit diagram stays the same, in the case of Fig. 9.2 (a) the desirable extrusion parameters can be set at the top vertex of the process window as good surface quality retains at a large area of the process window and thus productivity can be optimised; in Fig. 9.2 (b) the desirable extrusion can be again set at the same place, but this time due to an improved surface quality by low material transfer between the bearing and the extrudate. Therefore, with what process parameters the process should be performed really

depends on the f_{hk} value (thus the surface quality diagram) and where the existing process window is located.

It can however be generalised that within the process window case (a) produces better surface quality. This could be the reason why harder alloys such as 7XXX alloys and non-inert atmospheric condition cause worse surface quality.

9.2.3 Interpretation of results from the surface quality predictor

It has been mentioned that the results from the surface quality predictor do not correspond directly to the number of surface defects found on an extrusion product surface for the following reasons: 1) the calculated number of detached lumps is based on a line along the bearing length on the profile surface, as opposed to actual measurements which are counted within a certain area; 2) the results are calibrated with the magnification factor m_a, which is chosen to give satisfactory results and solution time. Since this parameter has been kept unchanged for all the calculations, the "surface quality diagram" as shown in Chapter 7 is both quantitatively and qualitatively valid: one can then determine at what operation conditions a good surface quality is most likely to be obtained. For a more precise value of the m_a factor, one can incorporate effects of metallurgy of the surface material as mentioned in section 9.2.1.

The calculated size values of detached lumps, however, can be quantitatively compared to the actual lateral size of pickup heads. This is due to the selection of an appropriate calculation area (640 × 480 μm). When the calculation area is small, the actual size of pickup heads (~ 200 μm) is actually larger than the calculation area. Therefore, to obtain the correct size, this sampling area is recommended.

9.2.4 Procedures of implementation of the surface quality predictor

AA 6063 has been studied in this thesis, however, the surface quality predictor can be applied to a large variety of alloy / bearing combinations. The nominal contact pressure distribution along the bearing length, the local contact temperature and sliding speed as well as material's constitutive equations are to be adapted. Together with this are the correct coefficients in the f_{hk} expression, which need to be measured by performing split die extrusion experiments. Therefore, the procedures for implementing the surface quality are:

- Perform split die extrusion experiments to obtain the coefficients in the f_{hk}

expression in Eq. 3.32: The experiments should be performed with exactly the same alloy / bearing combination, including alloy type, treatment of the bearing (hardened / nitrided). The f_{hk} coefficients can be fitted by measuring the sticking / slipping lengths on the bearings, extruded at different combinations of process parameters (T_{ext} and v_{ext}).

At least six extrusion runs should be performed with at least two extrudate surface temperature values and three exit speed values. Due to the characteristics of the f_{hk} value, the following is to be considered when selecting the parameters:

- When temperature and / or exit speeds are low, f_{hk} is always equal to unity. Therefore high values of both temperature and exit speed are suggested during the fitting extrusion experiments.
- In order to make sure both sticking and slipping zones are present on the bearing surface, a slightly choked bearing is desirable. With a fully relieved or parallel bearing the sticking zone might be absent and determination of the f_{hk} value is not possible.

- Obtain pressure distribution with respect to different operational conditions: For complex profiles FEM should be performed with each combination of operation conditions in order to obtain the corresponding nominal contact pressure distribution along the bearing length. For simple solid profiles the simple slab–analysis can be performed as illustrated in Chapter 4.

- With the above data a surface quality diagram can be constructed as shown in Chapter 7 so that process parameters can be tailored to give good surface quality — reduce surface defect formation.

9.3 Recommendations

9.3.1 About this work

Chapter 3: Modelling contact and friction in aluminium extrusion processes.

- A better understanding of the interfacial shear factor f_{hk} is beneficial. In this study the coefficients in Eq. 3.32 were obtained based on fitting them with experimental results from other research [26]. The model developed in this

study shows how f_{hk} influences the surface quality; with a thorough understanding of this parameter, it can be intentionally controlled towards a better surface quality. Further study should include effects of atmospheric conditions on the f_{hk} value, effects of surface treatment or coating of the bearing surface and effects of alloy composition, etc.

- The contact and friction model generally can be applied to any application involving metal–metal contact under high nominal contact pressure condition, e.g. metal forming processes. The model can also be extended to include the effect of bulk deformation.

- Although it has been established that the coefficient of friction inside the bearing channel varies with temperature and exit speed, and there are both sticking and slipping zones present, it is not recommended to implement the friction model to FEM of aluminium extrusion due to: 1) friction inside the bearing does not contribute significantly to the deformation zone, which is the core of FEM research on aluminium extrusion; 2) numerically it is unstable to implement both sticking and slipping boundary conditions. However, it is recommended to use the friction model as a post-processor for FEM simulation.

Chapter 4: Split die extrusion experiments — Part I: validation of the contact and friction model.

- The way the pressure distribution along the bearing was obtained is based on some empirical relations and a simple slab analysis. The method works fine for simple profiles as pressure variation along the cross section is small compared to along the extrusion direction. For complex profiles the pressure distribution along the bearing is not as smooth, and should then be obtained by FEM calculations.

Chapter 6: Modelling formation of surface defects on aluminium extrusion products

- As discussed in Section 9.2.1, a more precise m_a factor can be obtained by considering the grain boundary weakening effect from β–AlFeSi particles. The physical model can thus be extended to cover metallurgical aspects of the extrudate material.

Chapter 7: Surface quality predictor — towards application to aluminium extrusion.

- Not only can the surface quality predictor be applied to the actual surface quality control, but it can also be applied to the quality of weld seams of the extrusion products, as pickups can jeopardise the strength of the weld seams. The surface quality predictor can be applied to two tribological situations in this regard to model possible surface defect formation: 1) the leg–extrudate interface; 2) the weld seam. For the latter case adaptation is needed as the counter surfaces are of equal hardness.

- At the moment running the surface quality predictor is very time consuming, it is thus advisable to make a compact version of the model, e.g. create a lookup table, so that it can be readily adopted by industry.

- It is also valuable to create a user friendly interface which guides the user (extruders) through the procedures described in Section 9.2.4. The interface can also communicate with FEM models so that necessary data can be transferred.

Chapter 8: Split die extrusion experiments **—** Part II: validation of the surface quality predictor.

- The model indicates a very nonlinear effect of bearing roughness to surface quality of the products. However, in the extrusion experiments this has not been clearly verified. In the first series bearings with different roughness values were used, however, the amount of pickups produced were too small to make a valid comparison. It is therefore recommended that the effect of bearing roughness on surface quality be studied using relieved bearing so that the total number of measurable pickups is increased.

9.3.2 Practical solutions towards good surface quality

From this study it has been shown that there are several solutions to obtain a good surface quality. Regarding industrial practices, the following recommendations are to be considered:

- Maintain a high contact stress level inside the bearing channel. This helps formation of a continuous aluminium transfer layer on the bearing channel; a large contact pressure level also elongates the sticking length. The following are proposed:
  - Use a slightly choked bearing (< 1º) to maintain contact pressure inside the bearing. When designing the die, the elastic compliance of the die bearing during extrusion must be taken into account.
  - Extreme care must be taken when "correcting" the die geometry, after the die has been delivered from its manufacturer. The correction quite commonly is done by manual polishing of the bearing surface along the extrusion direction (which is easier to perform); however, when not done properly the effective bearing angle (choked or relieved) could be altered without noticing it.

- Adjust the extrusion conditions and as a result the f_{hk} values so that formation of the transferred aluminium does not fall into the "dangerous zone" as discussed in Chapter 6. The following are proposed:
  - Adjust extrudate surface temperature and exit speed so that pickup formation is away from the peak shown in the pickup diagram. This means either temperature and speed is low, or they are high over the peak.

- Reduce exposure of the extrudate to the surface defect formation area on the bearing – the slipping zone:
  - Reduce slipping length by increasing f_{hk} value or increase contact pressure.
  - Reduce the overall bearing length, provided the velocity control effect of the bearing is adequate (avoid using zero bearing). This effectively means that the best option would be a short, choked bearing.

- Alter the morphology of the transferred aluminium:
  - Apply die cooling so that the temperature drop across the extrudate - bearing interface is large enough to terminate the growth process.
  - Artificially deposit a continuous aluminium layer on the bearing surface prior to extrusion, e.g. by brush coating. In this way, discrete aluminium speckles on the bearing surface cannot form.

Appendix A
Summit-based contact model

The conventional way of describing the true contact area between two rough surfaces is to assume that contact only occurs at the summits — local surface maxima. The summit-based contact model enables representation of contact spots by a certain geometry, for example, spherically tipped summit in the Greenwood and Williamson model [13][14], paraboloidal summit with an elliptic cross section [33] and body of revolution with a power-law generatrix [19][20], etc. The geometrical parameters determining the exact shape can be extracted solely by analysing the local summit geometry as introduced in Section 2.1.1.1. In this section only spherically tipped summits are elaborated.

A.1 Single summit

A.1.1 Static contact

First of all, it has been shown in Section 2.1.1.3 that two rough surfaces contact can be reduced to the contact between a perfectly smooth surface and a surface with equivalent surface roughness. In most cases a rigid smooth surface in contact with a deformable rough surface is considered. A single deformable summit in contact can be schematically shown in Fig A.1(a):

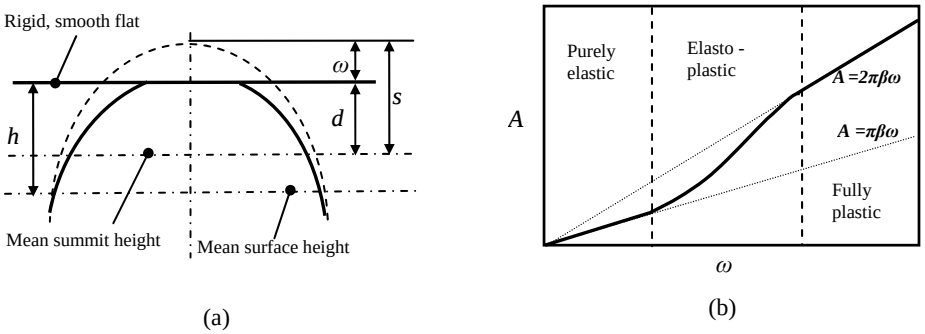

Fig A.1. Schematic illustration of the single summit model and contact area as a function of the deformation mode and contact interference ω.

The deformation modes of the summit essentially depend on the geometry of the summit and the interference ω. The deformation of this summit can be elastic, fully plastic or elasto–plastic. When the interference is smaller than the elastic to plastic deformation transition value at which onset of plastic deformation occurs, the contact remains purely elastic, and can be described by the Hertzian contact theory [71]:

Conditions: $$w < w_{el,st,trans} = \left(\frac{0.3pH}{E^*} \right)^2 b^* \tag{A.1}$$

Load carried: $$F_{el,st} = \frac{4}{3} E^* \left(b^* \right)^{1/2} w^{3/2} \tag{A.2}$$

Contact area: $$A_{el,st} = pb^* w \tag{A.3}$$

It can be shown that fully plastic deformation occurs when the interference reaches 54 times the elastic to plastic deformation transition value [71]:

Conditions: $$w \geq w_{pl,st,trans} = 54 w_{el,st,trans} \tag{A.4}$$

Load carried: $$F_{pl,st} = 2pb^* wH \tag{A.5}$$

Contact area: $$A_{pl,st} = 2pb^* w \tag{A.6}$$

In between these two modes the deformation is elasto–plastic, where Zhao's model [17] applies:

Conditions: $$w_{el,st,trans} \leq w < w_{pl,st,trans} \tag{A.7}$$

Load carried:
$$F_{ep,st} = \left(1 - 0.6 \frac{\ln w_{pl,st,trans} - \ln w}{\ln w_{pl,st,trans} - \ln w_{el,st,trans}} \right) \left[1 - 2\bar{v}^3 + 3\bar{v}^2 \right] pb^* wH \tag{A.8}$$
$$\bar{w} = \frac{w - w_{el,st,trans}}{w_{pl,st,trans} - w_{el,st,trans}}$$

Contact area: $$A_{ep,st} = pb^* w \left[1 - 2\bar{w}^3 + 3\bar{w}^2 \right] \tag{A.9}$$

The load–displacement relations of different deformation modes is shown in Fig A.1(b).

A.1.2 Sliding contact

For sliding contact the situation in which a rigid summit slides against a deformable surface is discussed for convenience. As the rigid asperity slides through the flat counterpart, the morphology of the groove generated by the asperity and the shape of the contact area vary with deformation modes, as schematically shown in Fig. A.2:

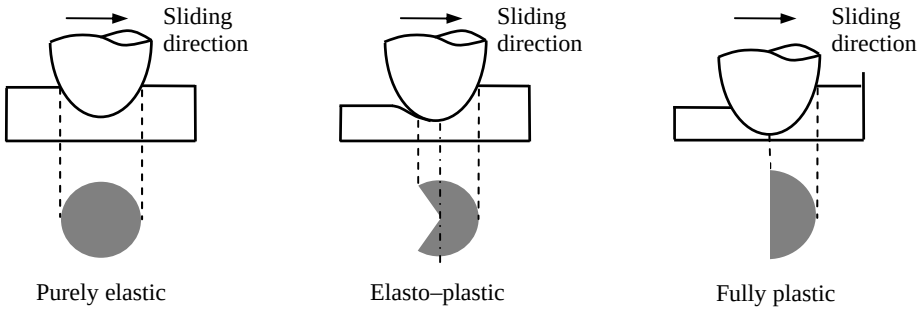

Fig. A.2 Schematic illustration of deformation modes and contact area in sliding contact condition.

The above figures show that as the indenter has passed the contact spot, the deformed material can fully recover in the purely elastic mode, but it cannot at all if the deformation is fully plastic, forming a semi-circular contact area. In the elasto–plastic regime the deformed material can partially recover, leaving a backwards "Pac–man" shaped contact area. Therefore, in the purely elastic sliding contact mode, the expressions of contact area and load are the same as static contact, whereas in the fully plastic mode the contact area is only a half of what it would be in static contact. The elastic to elasto–plastic transition interference can be obtained by letting the maximum Von–Mises stress in the contact region be equal to the yield stress. In order to obtain the Von–Mises stress, the stress tensor can be calculated using the explicit equations developed by Hamilton [93]. The contact area and load in elasto–plastic contact in sliding situation are summarised below:

Conditions: $$w_{el,sl,trans}\,(s_V = Y) \le w < w_{pl,sl,trans}\left(F_{pl,sl,trans} = 400F_{el,sl,trans}\right) \tag{A.10}$$

Load carried: $$F_{ep,sl} = \left(1 - 0.6\frac{\ln w_{pl,sl,trans} - \ln w}{\ln w_{pl,sl,trans} - \ln w_{el,sl,trans}}\right) pb^{*}wH \tag{A.11}$$

Contact area: $A_{ep,sl} = pb^{*}w$ (A.12)

A.2 Multi-summit contact

When the separation h between two engineering surfaces is to be solved, the situation involves multi-summit contact. Instead of taking into account the interaction between summits as in the contact patch-based model, the summit-based model assumes each summit contributes to load bearing and does not interfere with others. Assuming that all the summits are spherically tipped with radius β, which can be obtained by taking the average tip radius for all the summits, the following expressions give the load carried by a contact pair at a certain surface separation h. For static contact:

$$F_{st}(h) = \frac{4}{3} n \sqrt{b^{*}} E^{*} \int_{h}^{w_1} w^{\frac{3}{2}} f(s) ds + pnb^{*} H \int_{w_1}^{w_2} \left(1 - 0.6 \frac{\ln w_{pl,st,trans} - \ln w}{\ln w_{pl,st,trans} - \ln w_{el,st,trans}} \right) \times \left[1 - 2\overline{w}^{3} + 3\overline{w}^{2} \right] w f(s) ds + 2pnb^{*} H \int_{w_2}^{s_{\max}} w f(s) ds$$

(A.13)

For sliding contact this writes:

$$F_{st}(h) = \frac{4}{3} n \sqrt{b^{*}} E^{*} \int_{h}^{w_1'} w^{\frac{3}{2}} f(s) ds + pnb^{*} H \int_{w_1'}^{w_2'} \left(1 - 0.6 \frac{\ln w_{pl,st,trans} - \ln w}{\ln w_{pl,st,trans} - \ln w_{el,st,trans}} \right) \times w f(s) ds + pnb^{*} H \int_{w_2'}^{s_{\max}} w f(s) ds$$

(A.14)

Where $\omega_1 \sim \omega_3$ and $\omega_1' \sim \omega_3'$ are the transition interferences for static and sliding contact conditions, respectively. By equating the calculated load with the input load, the surface separation and contact situation can be solved.

Appendix B
Nayak's analytical model for the number of contact patches

In Chapter 3 the problem of contact coalescence was addressed and a deterministic contact model based on contact patches was presented. It has been shown that the ratio between the number of contact patches in contact, and that of the summits in contact, can be determined by the deterministic model. This model has been compared with Nayak's analytical model based on random process theory [15]. Specifically, Nayak considers the number of closed contours on a rough surface. Unfortunately, a contact patch counted already as one closed contour might contain "holes", which is also counted as closed contours. This problem was then solved by Greenwood [67], who offered a speculative yet quite accurate solution. This section will be based on the contribution from the two.

Nayak shows that for an isotropic Gaussian surface, the difference between number of contact patches and that of holes can be related with the number of summits, shown as:

$$r_{cp}(x) - r_h(x) = \frac{1}{(2p)^{3/2}} \left(\frac{s_s}{s} \right)^2 x \exp\left(-0.5x^2\right) \tag{B.1}$$

Where ρ is the density of a surface feature (number / area), ξ is the dimensionless surface separation, σ and σ_s are RMS of surface height and surface slopes, respectively. However, the density of "holes" cannot be determined by random process theory. Alternatively, Greenwood suggested that at high separation (small load), the number of holes (thus the number of surface minima above ξ) can be approximated to that of the number of surface minima below ξ, which in turn is equal to the number of summits above $-\xi$. The density of summits is also given by Nayak's random process model [9]:

$$r_s(x) = \int_x^\infty f_s(s) ds \tag{B.2}$$

$$f_s(x) = \frac{1}{6p\sqrt{3}}\left(\frac{s_s}{s_k}\right)^2 P(x,y) \tag{B.3}$$

$$P(x,y) = \frac{3}{2p}\frac{\sqrt{2y-3}}{y}x\exp\left(-C_1x^2\right) + \frac{3\sqrt{3}}{2\sqrt{2p}}\frac{1}{y}\left(x^2-1\right)\exp\left(-0.5x^2\right)\left[1+\mathrm{erf}\left(C_2x\right)\right]$$
$$+\sqrt{\frac{y}{2p(y-1)}}\exp\left(\frac{-yx^2}{2(y-1)}\right)\left[1+\mathrm{erf}\left(C_3x\right)\right]$$

(B.4)

$$C_1 = \frac{y}{2y-3};\ C_2 = \sqrt{\frac{3}{2(2y-3)}};\ C_3 = \sqrt{\frac{y}{2(y-1)(2y-3)}} \tag{B.5}$$

Where the bandwidth parameter ψ can be related to moments of the surface PDF:

$$y = \frac{m_0 m_4}{m_2^2} = \left(\frac{s\,s_k}{s_s^2}\right)^2 \tag{B.6}$$

The density of contact patches can thus be rewritten into:

$$r_{cp}(x) = r_s(-x) + \frac{1}{(2p)^{3/2}}\left(\frac{s_s}{s}\right)^2 x\exp\left(-0.5x^2\right) \tag{B.7}$$

A more illustrative number, the ratio between number of contact patches and summits can be shown to have the form:

$$\frac{r_{cp}(x)}{r_s(x)} = \frac{6p\sqrt{3}}{(2p)^{3/2}}\frac{yx\exp\left(-0.5x^2\right)}{F(x,y)} + \frac{F(-x,y)}{F(x,y)} \tag{B.8}$$

This suggests that the ratio is merely a function of the dimensionless separation ξ and the bandwidth parameter ψ. Plotting of Eq. B.8 is shown in Fig. 3.2; a comparison with the deterministic contact patch model is shown in Fig. 3.4. They show that the number of contact patches decreases significantly as separation is

reduced, due to event of contact coalescence.

Appendix C
Ploughing, wedge formation and cutting during sliding contact

When a hard asperity is sliding through a soft surface, three wear modes can be distinguished: ploughing, wedge–formation and cutting [40]. These regimes can be shown in a wear mode diagram as a function of the attack angle of the sliding asperity θ and the interfacial shear factor f_{hk}, as shown in Fig C.1:

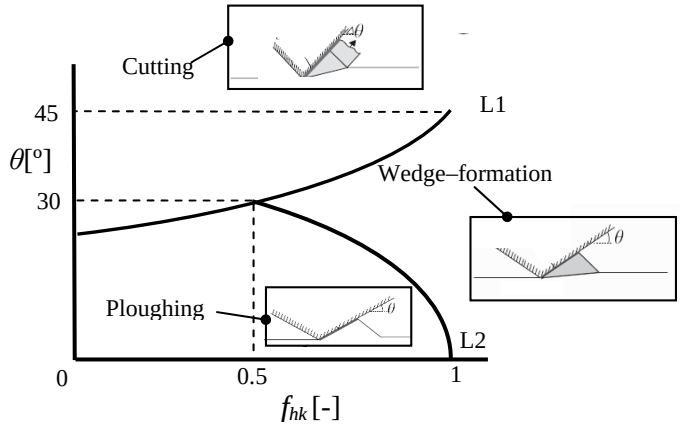

Fig C.1 Wear mode diagram.

The transition lines L1 and L2 can be quantified as [10]:

Ploughing → wedge–formation (L2) $$q_{p\lg\to wf} = \frac{1}{2}\arccos f_{hk} \quad \text{(C.1)}$$

Ploughing, wedge–formation → cutting (L1) $$q_{p\lg,wf\to cut} = \frac{1}{4}\left(p - \arccos f_{hk}\right) \quad \text{(C.2)}$$

In the cutting regime, the asperity cuts through the substrate with a small coefficient of friction, usually resulting in wear debris in the form of chipping. Wear debris will most likely be transferred to the low parts of the tool surface and not to the most critical high parts, the contact patches. In the ploughing regime, the

material will be displaced to the ridges on both sides of the track and no material removal occurs. However, in the wedge–formation regime the deformed material transfers to the front of the asperity, forming a wedge shape. This fleck of material is stuck in between the asperity and the substrate, therefore is prone to material transfer. In this study material transfer is only considered to occur in the wedge–formation regime.

The resultant coefficient of friction associated with different regimes was studied by Challen and Oxley [37] by constructing slip–line field for the perfectly plastic deformation, which is suitable for the scope of this study. They studied a sliding wedge that has an attack angle θ. In this study the 2–D attack angle can be related with the degree of penetration of an elliptical paraboloid to make the friction model applicable for our contact patches:

$$q_{eff} = \arctan\left(\frac{2.5w\sqrt{a_{mn}{}^2\cos^2 j + a_{mj}{}^2\sin^2 j}}{a_{mj}a_{mn}}\right) \tag{C.3}$$

In the cutting mode, the coefficient of friction is written:

$$m(q, f_{hk}) = \tan\left(q - \frac{1}{4}p + \frac{1}{2}\cos^{-1} f_{hk}\right) \tag{C.4}$$

In the wedge–formation mode:

$$m(q, f_{hk}) = \frac{\left(1 - 2\sin x_1 + \sqrt{1 - f_{hk}^2}\right)\sin q + f_{hk}\cos q}{\left(1 - 2\sin x_1 + \sqrt{1 - f_{hk}^2}\right)\cos q - f_{hk}\sin q} \tag{C.5}$$

In which:

$$x_1 = q - \frac{1}{4}p - \frac{1}{2}\arccos f_{hk} + \arcsin\frac{\sin q}{\sqrt{1 - f_{hk}}} \tag{C.6}$$

In the ploughing mode:

$$m(q,f_{hk}) = \frac{x_2 \sin q + \cos\left(\cos^{-1} f_{hk} - q\right)}{x_2 \cos q + \sin\left(\cos^{-1} f_{hk} - q\right)} \tag{C.7}$$

In which:

$$x_2 = 1 + \frac{1}{2}p + \cos^{-1} f_{hk} - 2q - 2\sin^{-1}\left(\frac{\sin q}{\sqrt{1 - f_{hk}}}\right) \tag{C.8}$$

Appendix D
Critical angle for lump growth

Aluminium alloys are no longer strain hardenable at extrusion temperatures, which means the difference between hardness values of the transferred lumps of aluminium and the deforming extrudate surface merely results from a die quenching effect. However, the temperature difference between the die bearing and the extrudate surface is quite small, due to: 1) in most industrial extrusion plants the dies are not artificially cooled; 2) the thickness of the "gap" between the bearing and the extrudate surface is small (of the order of bearing roughness). Therefore, the transferred aluminium and the extrudate surface are of approximately equal hardness. According to Kayaba et al. [84], this suggests that the transferred lump can only grow to a certain small critical attack angle before shearing.

A critical wedge tip angle $\theta_{w,\,cr}$ was defined above which plastic yielding of the hard asperity will take place. This critical value depends on the hardness ratio between the soft and hard surfaces r_H, and the interfacial shear factor f_{hk}. The hardness ratio r_H is:

$$r_H = \frac{H_{ext}}{H_{lump}} \tag{D.1}$$

The relations between the critical wedge tip angle $\theta_{w,\,cr}$, the hardness ratio and the interfacial shear factor can be written as:

When f_{hk} « 1

$$r_H = \begin{cases} \dfrac{2 + 2q_{w,cr} - p}{2 + q_{w,cr}} & r_H \geq \dfrac{4}{4+p} \\ \dfrac{2 - \cos q_{w,cr}}{2 + q_{w,cr}} & r_H < \dfrac{4}{4+p} \end{cases} \tag{D.2}$$

When $f_{hk} \to 1$

$$r_H = \begin{cases} \dfrac{1-\frac{3}{2}p+\cos^{-1}(r_H f_{hk})+\sqrt{1-(r_H f_{hk})^2}+2q_{w,cr}}{1-\frac{1}{2}p+\cos^{-1} f_{hk}+\sqrt{1-f_{hk}^{\ 2}}+q_{w,cr}} \\ q_{w,cr} \geq \dfrac{3}{4}p-\dfrac{1}{2}\cos^{-1}(r_H f_{hk}) \\ \dfrac{1-\sqrt{1+r_H f_{hk}}G_1-\sqrt{1-r_H f_{hk}}G_2+\sqrt{1-(r_H f_{hk})^2}}{1-\frac{1}{2}p+\cos^{-1} f_{hk}+\sqrt{1-f_{hk}^{\ 2}}+q_{w,cr}} \\ \sin^{-1} f_{hk} \leq q_{w,crt} \leq \dfrac{3}{4}p-\dfrac{1}{2}\cos^{-1}(r_H f_{hk}) \\ \dfrac{1-\sqrt{1+r_H f_{hk}}G_1-\sqrt{1-r_H f_{hk}}G_2+\sqrt{1-(r_H f_{hk})^2}}{1-\sqrt{1+f_{hk}}G_3+\sqrt{1-f_{hk}}G_4+\sqrt{1-f_{hk}^{\ 2}}} \\ \dfrac{1}{4}p-\cos^{-1}(r_H f_{hk}) \leq q_{w,cr} \leq \sin^{-1}(f_{hk}) \end{cases} \quad \text{(D.3)}$$

In which the geometrical factors $G_1 \sim G_4$ are:

$$G_1 = \cos(q_{w,cr})+\sin(q_{w,cr}); \quad G_2 = \cos(q_{w,cr})-\sin(q_{w,cr})$$
$$G_3 = \cos\left(\frac{1}{2}q_{w,cr}\right)-\sin\left(\frac{1}{2}q_{w,cr}\right); \quad G_1 = \cos\left(\frac{1}{2}q_{w,cr}\right)+\sin\left(\frac{1}{2}q_{w,cr}\right) \quad \text{(D.4)}$$

The critical attack angle for lump growth can be related to the critical wedge tip angle as:

$$q_{cr} = \frac{1}{2}p-\frac{1}{2}\sin q_{w,cr} \quad \text{(D.5)}$$

Appendix E
Material specifications for split die extrusion experiment

E.1 Extrudate material

Table E-1 Chemical composition of the extrudate material (from XRD measurement).

Element	Si	Mg	Mn	Fe	Cu	Al
% Weight	0.25	0.40	0.26	0.17	0.08	Remainder

E.2 Bearing surface treatment

All the dies were manufactured with H1.2344 tool steel. The bearing surfaces were hardened according to the following approach:

- Heated to 1030 °C in vacuum.
- Quenched to 150 °C in vacuum.
- Tempered at 620 °C in vacuum.

Hardness: 420 HV10 ($\approx$ 4110 MPa).

The chemical composition of the bearing material is listed below:

Table E-2 Chemical composition of the extrudate material (from XRD measurement).

Element	C	Cr	Mo	V	Si	Fe
% Weight	0.32	5.74	0.26	1.17	1.3	Remainder

Appendix F
Specifications of the split die

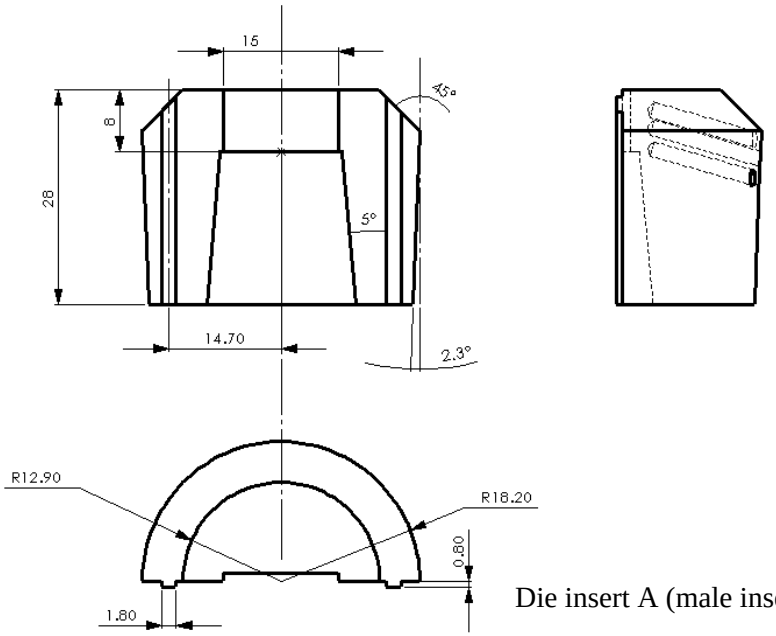

Die insert A (male insert)

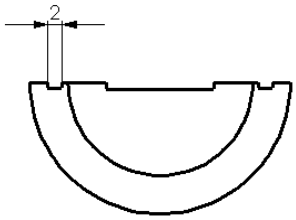

Die insert B (female insert)

Appendix G
Constitutive parameters for aluminium alloys

Sellars–Tegart's equation has been used in this study to describe the constitutive flow behaviour of aluminium alloys under elevated temperature conditions. Aluminium alloys under such conditions are thermal softened and strain rate hardened:

$$\sigma_f(T,\dot{\varepsilon}) = \sigma_m \operatorname{arcsinh}\left[\left(\frac{Z}{A_z}\right)^{\frac{1}{m}}\right]; \quad Z = \dot{\varepsilon}\exp\left(\frac{Q}{RT}\right) \tag{G.1}$$

Constants in the above expressions vary with aluminium alloys. Table G-1 shows the values for the coefficients for a range of aluminium alloys obtained from torsion test.

Table G-1 Constants in the constitutive equation for some aluminium alloys [1].

Alloy	σ_m [MPa]	m [−]	Q [J/mol]	A_z [s^{-1}]
1100	22.2	5.66	1.58e5	5.18e10
2024	62.5	4.27	1.49e5	3.25e8
3003	31.6	4.45	1.65e5	4.81e11
4047	25.0	2.65	1.29e5	7.76e8
5005	34.5	5.80	1.84e5	3.75e11
5052	62.5	5.24	1.55e5	4.24e10
6061	22.2	3.55	1.45e5	2.41e8
6082	22.2	2.98	1.53e5	2.39e8
7050	37.2	2.86	1.52e5	8.39e9
7075	70.9	5.41	1.29e5	1.03e9

Appendix H
Photographic impressions of the split die extrusion

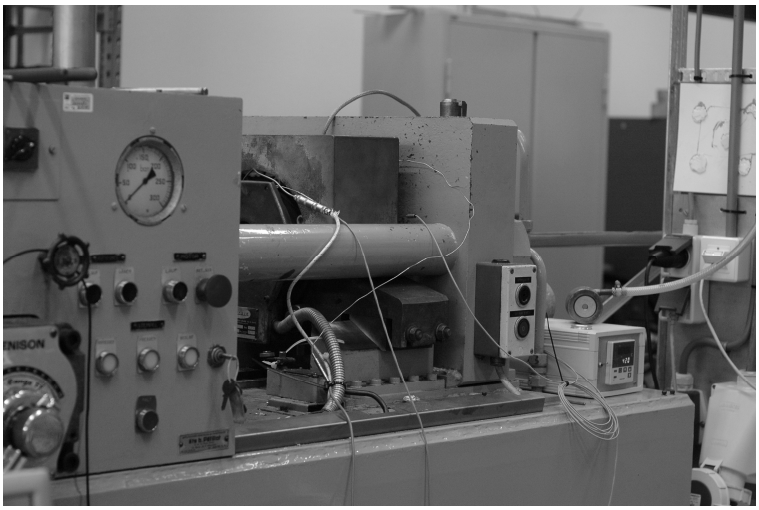

Fig H.1 The press assembly.

Fig H.2 The control unit of the extrusion press.

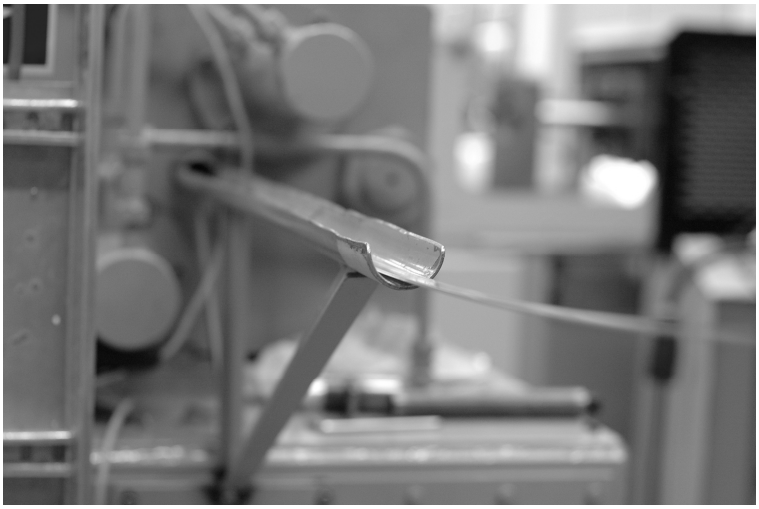

Fig H.3 The exiting profile.

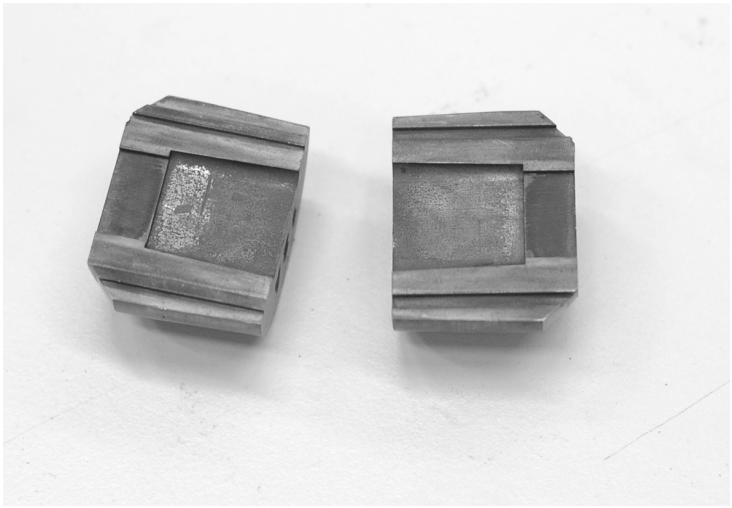

Fig H.4 Die inserts split up after extrusion.

References

[1] Sheppard, T., Extrusion of Aluminium Alloys, Kluwer Academic Publishers, the Netherlands, 1999.

[2] Peris, R.G., 2007, Effects of extrusion conditions on “die pick – up” formed during extrusion of aluminium alloy AA 6060, Master thesis, Auckland University of Technology, New Zealand.

[3] European Aluminium Association, “Aluminium and Aluminium Alloys – Extrusion”, 2000, from: http://www.azom.com/details.asp?ArticleID=1554.

[4] Parson, N.C., Hankin, J.D. and Bryant, A.J., 1984, The metallurgical background to problems occurring during the extrusion of 6xxx alloys, 3rd International aluminium extrusion technology seminar, 287 – 295.

[5] Sheppard, T. and Clode M.P., 1988, The origin of surface defects during extrusion of AA 6063 alloy, 4th International aluminium extrusion technology seminar, 329 – 341.

[6] Lassance, D., 2006, Modelling of damage mechanisms in AlMgSi alloys, PhD thesis, Universite Catholique de Louvain, Belgium.

[7] Minoda, T., Hayakawa, H., Matsuda, S. and Yoshida, H., 2000, The mechanism of pick – up formation on 6063 aluminium alloy extrusions, 7th International aluminium extrusion technology seminar, 23 – 29.

[8] Van Alsten, J. and Granick, S., 1989, Friction measured with a surface forces apparatus, Tribology Transactions 32, 246 – 250.

[9] Nayak, P.R., 1971, Random process model of rough surfaces, Journal of Lubrication Technology 93, 398 – 407.

[10] Rooij, M.B. de, 1998, Tribological aspects of unlubricated deepdrawing processes, PhD Thesis, University of Twente, The Netherlands.

[11] Greenwood, J.A., 1984, A unified theory of surface roughness, Proceedings of the Royal Society of London A 393, 133 – 157.

[12] Moalic, H., Fitzpatrick, J.A. and Torrance, A.A., 1989, A spectral approach to the analysis of rough surfaces, Journal of Tribology 111, 359 – 363.

[13] Greenwood, J.A. and Williamson, J.B.P., 1966, Contact of Nominally Flat Surfaces, Proceedings of the Royal Society of London: A 295, 300 – 319.

[14] Chang, W.R., Etsion, I. and Bogy, D.B., 1987, An elastic-plastic model for the contact of rough surfaces, Journal of Tribology 109, 257 – 263.

[15] Nayak, P.R., 1973, Random process model of rough surfaces in plastic contact, Wear 26, 305 – 333.

[16] Pullen, J. and Williamson, J.B.P., 1972, On the plastic contact of rough

surfaces, Proceedings of the Royal Society of London: A 327, 159 – 173.

[17] Zhao, T., Maietta, D.M. and Chang, L., 2000, An asperity microcontact model incorporating the transition from elastic deformation to fully plastic flow, Journal of Tribology 122, 86 – 93.

[18] Masen, M.A. and Rooij, M.B. de, 2002, Abrasive wear between rough surfaces in deep drawing, Wear 256, 639 – 646.

[19] De Pellegrin, D.V. and Stachowiak, G.W., 2004, Evaluating the role of particle distribution and shape in two-body abrasion by statistical simulation, Tribology International 37, 255 – 270.

[20] Ma, X., Rooij, M.B. de and Schipper, D. J., 2008, Modelling of contact and friction in aluminium extrusion, Tribology International 43, 1138 – 1144.

[21] Pullen, J. and Williamson, J.B.P, 1972, On the Plastic Contact of Rough Surfaces, Proceedings of Royal Society of London: A 327, 159-173.

[22] Westeneng, A., 2001, Modelling of Contact and Friction in Deep Drawing Processes, PhD thesis, University of Twente, the Netherlands.

[23] Gelinck, E.R.M., 1999, Mixed Lubrication of Line Contacts, PhD thesis, University of Twente, the Netherlands.

[24] Schipper, D.J., 1988, Transitions in the Lubrication of Concentrated Contacts, PhD thesis, University of Twente, the Netherlands.

[25] Wilson, J.E., Stott, F.H. and Wood, G.C., 1980, The development of wear – protective oxides and their influence on sliding friction, Proceedings of the royal society of London A, 369, 557 – 574.

[26] Tverlid, S., 1998, Modelling of friction in the bearing channel of dies for extrusion of aluminium sections, PhD thesis, Norwegian University of Science and Technology, Norway.

[27] Bjork, T., 2001, Tribological aspects of aluminiuim extrusion dies, PhD thesis, Karlstad University, Sweden.

[28] Moore, D.F., 1972, The Friction and Lubrication of Elastomers, Pergamon Press, London.

[29] Xie, Y. and Williams, J. A., 1996, The prediction of friction and wear when a softer surface slides against a harder rough surface, Wear 196, 21 – 34.

[30] Bowden, F. P. and Tabor, D., 1950, The Friction and Lubrication of Solids I, Clarendon Press, Oxford.

[31] Goddard, J. and Wilman, H., 1962, A theory of friction and wear during the abrasion of metals, Wear 5, 114 – 135.

[32] Lafaye, S., Gauthier, C. and Schirrer, R., 2006, Analysis of the apparent friction of polymer surfaces, Journal of Materials Science 41, 6442 – 6452.

[33] Masen, M.A., 2004, Abrasive tool wear in metal forming processes, PhD Thesis, University of Twente, the Netherlands.

[34] Bucaille, J.L., Felder, E. and Hochstetter, G., 2001, Mechanical analysis of the scratch test on elastic and perfectly plastic materials with the three – dimensional finite element modelling, Wear 249, 422 – 432.

[35] Lafaye, S., Gauthier, C. and Schirrer, R., 2006, The plough friction: analytical model with elastic recovery for a conical tip with a blunted spherical extremity, Tribology Letters 21, 95 – 99.

[36] Stachowiak, G.W. and Batchelor, A.W., 2001, Engineering Tribology, Butterworth – Heinemann, Wohurn, USA.

[37] Challen, J.M. and Oxley, P.L.B., 1979, An explanation of the different regimes of friction and wear using asperity deformation models, Wear 53, 229 – 243.

[38] Rooij, M.B. de and Schipper, D. J., 1997, Characterising microwear and material pickup in metal forming processes, Conference Proceedings of 1st International Conference on Tribology in Manufacturing Processes, Gifu, Japan, 41 – 46.

[39] Challen, J.M., McLean, L.J. and Oxley, P.L.B., 1984, Plastic deformation of a metal surface in sliding contact with a hard wedge: its relation to friction and wear, Proceedings of the Royal Society of London A 394, 161 – 181.

[40] Kato, K. and Hokkirigawa, K., 1988, An experimental and theoretical investigation of ploughing, cutting and wedge formation during abrasive wear, Tribology International 21, 51 – 57.

[41] Kuijpers, N.C.W., 2004, Kinetics of the β- AlFeSi to α- Al(FeMn)Si transformation in Al – Mg – Si alloys, PhD thesis, Delft University of Technology, the Netherlands.

[42] Couto, K.B.S., Clave, S.R., Van Geertruyden, W.H., Misiolek, W.Z. and Goncales, M., 2005, Effects of homogenisation treatment on microstructure and hot ductility of aluminium alloy 6063, Materials Science and Technology 21, 263 – 268.

[43] Zajac, S., Hutchinson, B. and Gullman, L. O., 1994, Microstructure control and extrudability of Al – Mg – Si alloys microalloyed with manganese, Materials Science and Technology 10, 323 – 333.

[44] Eivani, A.R., 2010, Modeling of microstructural evolution during homogenization and simulation of transient state recrystallization leading to peripheral coarse grain structure in extruded Al – 4.5Zn – 1Mg alloy, PhD thesis, Delft University of Technology, the Netherlands.

[45] Schikorra, M., Donati, L., Tomesani, L. and Tekkaya, A.E., 2008, Microstructure analysis of aluminium extrusion: prediction of microstructure on AA 6060 alloy, Journal of Materials Processing Technology 201, 156 – 162.

[46] Tan, C.F. and Said, M.R., 2009, Effect of hardness test on precipitation hardening aluminium alloy 6061 – T6, Chiang Mai Journal of Science 26, 276 – 286.

[47] Airod, A., Vandekinderen, H., Barros, J., Colas, R. and Houbaert, Y., 2003, Constitutive equations for the room temperature deformation of commercial purity aluminium, Journal of Materials Processing Technology 134, 398 – 404.

[48] Pachisia, S.K., Ramalingam, S.K. and Srinivasan, M.N., 1982, Flow stress of an aluminium alloy in the warm working range, Bulletin of Materials Science 4, 595 – 601.

[49] Yao, X.X., 2000, The strain – rate sensitivity of flow stress and work – hardening rate in a hot deformed Al-1.0Mg alloy, Journal of Materials Science Letters 19, 733 – 734.

[50] Sellars, C.M. and Tegart, W. J., Hot workability, Metallurgy Reviews 17, 1.

[51] Evangelista, E., Forcellese, A., Gabrielli, F. and Mengucci, P., 1991, in "Hot Deformation of Alumlnium Alloys", TMS, 121-139.

[52] Picu, R. C., Vincze, G., Ozturk, F., Gracio, J. J., Barlat, F. and Maniatty, A. M., 2005, Strain rate sensitivity of the commercial aluminum alloy AA5182-O, Materials Science and Engineering A 390, 334–343.

[53] Verlinden, B., Suhadi, A. and Delaey, L., 1993, A generalised constitutive equation for an AA 6060 alloy, Scripta Metallurgica et Materialia 28, 1441 – 1446.

[54] Lof, J., Klaseboer, G., Huetink, J. and Koenis, P.T.G., 2000, FEM simulations of aluminium extrusion using an elasto – viscoplastic material model, 7th International Extrusion Technology Seminar 2, 157 – 168.

[55] Schikorra, M., Donati, L., Tomesani, L. and Kleiner, M., 2007, The role of friction in the extrusion of AA6060 aluminum alloy, process analysis and monitoring, Journal of Materials Processing Technology 191, 288–292.

[56] Trent, E. M., 1991, Metal Cutting, Butterworths, London, UK.

[57] Parson, N., Jowett, C., Fraser, W. and Pelow, C., 1996, Surface defects on 6xxx alloy extrusions, 6th International Aluminium Extrusion Technology Seminar, Chicago, USA.

[58] Chanda, T., Zhou, J., Kowalski, L. and Duszczyk, J., 1999, 3D FEM

simulation of the thermal events during AA6061 aluminium extrusion. Scr. Mater. 41,195–202.

[59] Parvizian, F., Kayser, T., Hortig and Svendsen, B., 2009, Thermomechanical modeling and simulation of aluminium alloy behavior during extrusion and cooling, Journal of Materials Processing Technoology 209, 876 – 883.

[60] Wang, L., Cai, J., Zhou, J. and Duszczyk, J., 2009, Characteristics of the friction between aluminium and steel at elevated temperatures during Ball-on-disc Tests, Tribology Letters 36, 183 – 190.

[61] Moufki, A., Molinari, A. and Dudzinski, D., 1998, Modelling of orthogonal cutting with a temperature dependent friction law, Journal of the Mechanics and Physics of Solids 46, 2103–2138.

[62] Thedja, W.W., Muller, K.B. and Ruppin, D., 1992, Tribomechanical process on the die land area during extrusion of of AA6063 alloy, Proceedings of Extrusion Technology Seminar, Chicago, 467.

[63] Abtahi, S., 1996, Interface Mechanisms on the Bearing Surface in Extrusion, Proceedings of Extrusion Technology Seminar, Chicago, 125.

[64] Ma, X., Rooij, M.B. de and Schipper, D.J., 2009, On the formation of a sticking layer on the bearing during thin – section aluminium extrusion, Proceedings of Comsol conference, Milan.

[65] Qi, H. S. and Mills, B., 2000, Formation of a transfer layer at the tool-chip interface during machining, Wear 245, 136 – 147.

[66] Birol, Y., 2004, The effect of homogenization practice on the microstructure of AA6063 billets, Journal of Materials Processing Technology 148, 250 – 258.

[67] Greenwood, J.A., 2007, A note on Nayak's third paper, Wear 262, 225 – 227.

[68] Ma, X., Rooij, M. B. de and Schipper, D. J., 2009, A load dependent contact and friction model for fully plastic conditions, Wear 269, 790 – 796.

[69] Hu, Y.Z. and Tonder, K., 1992, Simulation of 3-D Random Rough Surface by 2-D Digital Filter and Fourier Analysis, International Journal of Machine Tools and Manufacture 32, 83-90.

[70] Bos, J., 1995, Frictional heating of tribological contacts, PhD Thesis, University of Twente, the Netherlands.

[71] Johnson, K.L., 1985, Contact Mechanics, Cambridge University Press, Cambridge.

[72] Heide, E. van der, 2002, Lubricant failure in sheet metal forming processes, PhD thesis, University of Twente, the Netherlands.

[73] Ernst, H. and Merchant, M.E., 1941, Chip formation, friction, and high

quality machined surfaces, Surface Treatment of Metals, American Society of Metals.

[74] Saoubi, R.M. and Chandrasekaran, H., 2005, Innovative Methods for the Investigation of Tool-Chip Adhesion and Layer Formation during Machining, Manufacturing Technology 54, 59 – 62.

[75] Challen, J.M. and Oxley, P.L.B., 1984, A slip line field analysis of the transition from local asperity contact to full contact in metallic sliding friction, Wear 100, 171 - 193.

[76] Adams, G.G. and Muftu, S., 2005, Improvements to a Scale-Dependent Model for Contact and Friction, Journal of Physics D: Applied Physics 38, 1402–1409.

[77] Nosonovsky, M., 2007, Modelling size, load and velocity effect on friction at micro/nanoscale, International Journal of Surface Science and Engineering 1, 22-37.

[78] Tercelj, M., Turk, R., Kugler, G., Fajfar, P. and Cvahte, P., 2006, Measured temperatures on die bearing surface in aluminium hot extrusion, Materials and Geoenvironment, 53, 163 – 173.

[79] Miroux, A., 2009, Microstructure observation of press flees, Internal report.

[80] Ma, X. and Matthews, A., Evaluation of abradable seal coating mechanical properties, Wear 267, 1501 – 1510.

[81] Matienzo, L.J. and Holub, K.J., 1983, Applications of Surface Science 15, 307-320.

[82] Chowdhury, S.K.R and Pollock, H.M., 1981, Adhesion between metal surfaces: the effect of surface roughness, Wear 66, 307 – 321.

[83] Rabinowicz, E., 1995, Friction and Wear of Materials, Wiley – Interscience, 2nd edition.

[84] Kayaba, T., Kato, K. and Hokkirigawa, K., 1983, Theoretical analysis of the plastic yielding of a hard asperity sliding on a soft flat surface, Wear 87, 151 – 161.

[85] Yovanovich, M.M., 2005, Four decades of research on thermal contact, gap and joint resistance in microelectronics, IEEE Transactions on Components and Packing Technologies 28, 182 – 206.

[86] Li, L., Zhou, J. and Duszczyk, J., 2004, Prediction of temperature evolution during the extrusion of 7075 aluminium alloy at various ram speeds by means of 3D FEM simulation, Journal of Materials Processing Technology, 145, 360.

[87] Hunt, S. and Carlsson, L.A., 1993, Debonding in overmolded integrated

circuit packages, Journal of Electronic Packaging 115, 249 – 255.

[88] Yi, S., Shen, L., Kim, J.K. and Yue, C.Y., 2000, A failure criterion for debonding between encapsulants and leadframes in plastic IC packages, Journal of Adhesion Sicence and Technology 14, 93 – 105.

[89] Szeto, W.K., Xie, M.Y., Kim, J.K., Yuen, M.M.F., Tong, P. and Yi, S., 2000, Interface failure criterion of button shear test as a means of interface adhesion measurement in plastic packages, 2000 International Symposium on Electronic Materials & Packaging, 263 – 268.

[90] Israelachvili, J.N., 1991, Intermolecular and Surface Forces, Academic Press.

[91] Ramanan, T.R., Huff, O.A. and Phillipson, W.L., 2000, Extrusion defects – helping the customer to solve them, Proceedings of 7th International Aluminium Extrusion Technology Seminar, Chicago, 61 – 72.

[92] Duplancic, I., 2000, The effect of extrusion conditions on the surface propertiesof AlMgSi (6063) hollow sections, Proceedings of 7th International Aluminium Extrusion Technology Seminar, Chicago, 261 – 271.

[93] Hamilton, G.M., 1983, Explicit equations for the stresses beneath a sliding spherical contact, Proceedings of the Institution of Mechanical Engineers 197 C, 53 – 59.